

**Surface Plasmon Fluorescence Spectroscopy and
Microscopy Studies for Biomolecular Interaction Studies**

Dissertation zur Erlangung des Grades

‘Doktor der Naturwissenschaft’

am Fachbereich
Chemie und Pharmazie der
Johannes Gutenberg-Universität Mainz

vorgelegt von

Doene Demirgoez

aus Selimpasa, Istanbul-Turkey

Mainz, July, 2005

Dekan: Univ.-Prof. Dr. Peter Langguth

1. Berichterstatter: Prof. W. Knoll

2. Berichterstatter: Prof. Dr. W. Baumann

3. Berichterstatter: Prof. H. Decker

Tag der mündlichen Prüfung: 20, Juli 2005

Die vorliegende Arbeit wurde unter Betreuung von Herrn Prof. Dr. W. Knoll im Zeitraum zwischen April 2002 bis Juli 2005 am Max-Planck-Institut für Polymerforschung, Mainz angefertigt.

Contents

1 INTRODUCTION	5
1.1 The aim of the study	7
2 THEORETICAL BACKGROUND	8
2.1 Deoxyribo Nucleic Acid (DNA)	8
2.2 Peptide Nucleic Acids (PNAs):	10
2.3 Detection of DNA Hybridization on Surfaces	11
2.4 Genetically Modified Organism (GMO):	12
2.5 Detection of GMOs in food chain and EU regulations in GMO contained food labeling	12
2.5.1 DNA Based detection Methods:	13
2.5.1.1 <i>Polymerase Chain Reaction (PCR):</i>	13
2.5.1.2 <i>Real Time PCR:</i>	15
2.5.2 Protein Based Testing Methods:	16
2.5.2.1 <i>Western Blot</i>	16
2.5.2.2 <i>ELISA (Enzyme Linked Immunosorbent Assay)</i>	16
2.5.2.3 <i>Lateral flow strip</i>	17
2.5.2.4 <i>The Nucleic acid sequence-based amplification (NASBA):</i>	17
2.6 Microarrays	18
2.6.1 Making microarrays	18
2.7 Fluorescence	22
2.7.1 The Phenomena of the Fluorescence	22
2.7.2 Fluorescence Lifetime and Quantum Yield	23
2.7.3 Fluorescence Quenching	24
2.7.4 Photobleaching	25
2.8 Langmuir Adsorption	26
2.9 Evanescent Optics	29
2.9.2 Reflection and transmission of light	30
2.9.3 Surface Plasmon	32
2.9.4 Surface Plasmon with prism coupling	34
2.9.5 Optical Thickness	35
2.10 Surface Plasmon Fluorescence Spectroscopy (SPFS)	36
2.10.1 Fluorescence at the metal/dielectric interface	38
2.11 Surface Plasmon Microscopy (SPM)-Fluorescence Microscopy (SPFM)	39
2.11.1 Image Analysis	41
3 MATERIALS AND METHODS	44
3.1 Instrumental	44
3.1.1 Experimental Surface Plasmon Microscopy (SPM) and Surface Plasmon Fluorescence Microscopy (SPFM) Set-up	47
3.2 Substrate and Metal Layer preparation	47
3.2.1 Self Asssembled Monolayers (SAM) on gold	48
3.2.2 Binding of Streptavidin and preparation of the flow cell	50
3.2.3 Immobilization of the Catcher Probe onto the Substrate Surface	54
3.2.4 Hybridization reaction and Fluorescence Measurement	55
3.2.5 Surface Regeneration	61
3.3 Surface-Plasmon –Fluorescence Microscopy – A Novel Platform for Array Technology	62
3.3.1 Microarray preparation	62

3.3.1.1 Array Fabrication	62
3.3.1.2 Array Characterization	63
3.3.2 Hybridization between PNA-probe and oligonucleotides-target	63
RESULTS	64
4 PNA-DNA Hybridization Observed in Real-Time	64
4.1 Surface Plasmon Fluorescence Field-Enhanced Spectroscopy (SPFS) studies of PNA-DNA interaction on two dimensional (planar) surfaces	64
4.1.1 SPFS	65
4.1.2 Experimental	65
4.1.2.1 Fluorescence monitoring	65
4.1.3 Materials	66
4.1.4 Single kinetic measurements	69
4.1.5 Titration experiments	77
4.1.6 Global Analysis:	86
4.2 Surface Plasmon Fluorescence Microscopy (SPFM) studies of PNA-DNA interaction on microarrays	94
4.2.1 Aim	94
4.3 Conclusions	111
5 Genetically Modified Organism (GMO) detection in food chain by means of DNA-DNA and PNA-DNA Hybridization by Surface Plasmon Fluorescence Spectorcopy (SPFM)	113
5.1 DNA-DNA Hybridization on Biotin / Streptavidin Matrix	114
5.1.1 Aim	114
5.2 PNA-DNA Hybridization on SH-Streptavidin Matrix	125
5.2.1 Aim	125
5.2.2 Materials	125
5.3 CCD Saturation Test:	131
5.4 PNA-DNA Hybridization on Biotin thiol / Streptavidin Matrix	133
5.4.1 Array A	133
5.4.2 Array B	139
5.5 Conclusions	142
LIST OF FIGURES.....	144
LIST OF TABLES.....	152
APPENDIX A.....	153
BIBLIOGRAPHY.....	154
ACKNOWLEDGEMENT	
LEBENS LAUF	

1. INTRODUCTION

Biotechnology has enabled the modification of agricultural materials in a very precise way. Crops have been modified through the insertion of new traits or the inhibition of existing gene functions, named Genetically Modified Organism (GMO), and resulted in improved tolerance of herbicide and/or increased resistance against pests, viruses and fungi [Kuiper et al, 2002].

Seven millions farmers in 18 countries grew bioengineered crops on 167.2 million acres in 2003, compared to 145 millions acres in 2002, according to ISAAA report. In 1996, which was the first year that genetically modified crops were commercially available, about 4.3 million acres were under biotechnology cultivation [Kulkarni, 2004, F.E.Ahmed, 2002].

Upon an increase of the population and lack in nutrition, some other countries like South Africa and Brazil have also joined the GMO cultivated countries.

In Europe modified foods have not gained acceptance because of consumer suspicion resulting from earlier food and environmental concerns, transparent regulatory oversight, and mistrust in government bureaucracies. All these concern factors have fuelled the debates about the environmental and public health issues of GMOs like antibiotic resistance and gastrointestinal problems, destruction of agricultural diversity, and potential gene flow to the other genes. Upon these developments, the European Union regulations mandated labelling of GMOs containing food [EC, 1998, 2000]. Beside these reasons it is also important to allow the end consumers to make an informed choice [Nature Biotech. News, 2001]. Hence, the regulations established a 1% threshold for contamination of unmodified foods with GMO ingredients in early 2000. A consequence of the declaration of a 1% threshold was the need to progress from qualitative detection of alien DNA by using screening system to more complex quantitative procedures.

Food, naturally, contains a range of different substances, such as fatty acids, polysaccharides and lipids in addition to DNA and protein. Some of these substances may negatively affect the assay techniques use to detect the GMOs. For example, the presence of some plant polysaccharides can effectively inhibit polymerase chain reaction (PCR) and in the absence of appropriate controls that result could be interpreted as false negative.

Due to many other GMO varieties which are entering to the market or are in the pipeline for approval, the necessity for a powerful detection method become a crucial point. At this moment, microarrays seems to be holding the advantage of being able to detect, identify and quantify the large numbers of GMO varieties in a sample in one single assay.

By using microarrays, thousands of hybridization reactions can be screened simultaneously by two-dimensional image analysis. However, detection systems for microarrays require a highly sensitive and effective differentiation of signals from noise. At present, the lack of sensitivity of the imaging systems brings the necessity of using additional labelling techniques. Label based detection methods typically involve the use of fluorescence, where the oligonucleotide targets are tagged with dyes that are spectrally detectable. In fluorescence detection methods, the fluorescence signals are quantified by photo multiplier tubes (PMTs) or charged-coupled devices (CCDs). By measuring the fluorescence from labelled target molecules at different position on a microarray, one can identify molecules and determine their relative abundance in a sample. The most commonly used dyes are Cy5, Cy3 and AlexaFluor. These cyanine dyes are suitable because they are sensitive, photo-stable, highly soluble in water and exhibit low non-specific binding.

Fluorescence combined optical methods have enhanced sensitivity. One of the well-established optical method for biological sensing is the surface plasmon resonance (SPR) technique. It is a surface-sensitive optical method used to characterize the layers on gold (Au) or noble metal thin films [Kno1, 1998]. These measurements utilize the optical field enhancement that occurs at a metal/dielectric interface when surface plasmons are generated. Surface plasmons are electromagnetic waves that are excited by p-polarized light and propagate parallel to the Au surface. The optical field decays exponentially from the surface of the metal and has a maximum decay length of about 200nm. Within this region, the fluorophore can be excited.

Beside GMO detection, DNA arrays hold the most promising way to transfer complex biomolecular interaction in the interest of biomedical field. At the most basic level, DNA arrays provide expression of whole genes in a cell on a single chip. Therefore they also hold promise of transforming biomedical sciences by providing new vistas of complex biological systems.

1.1 The aim of the study

Under the light of the information gained during the presented studies, two key issues are addressed and solved.

- 1) what is the best strategy to design and built an interfacial architecture of a probe oligonucleotide layer either on a two dimensional surface or on an array platform;
- 2) what is the best detection method allowing for a sensitive monitoring of the hybridisation events?

The study includes two parts:

1. Characterization of different PNAs on a 2D planar surface by means of defining affinity constants using the very well established optical method “Surface Plasmon Fluorescence Spectroscopy”(SPFS) and for the array platform by “Surface Plasmon Fluorescence Microscopy” (SPFM), determination of the sensitivity of these two techniques.
2. Detection of the existence and threshold value of alien DNA in food chain by using DNA and PNA catcher probes on the array platform in real-time by SPFM.

2. THEORETICAL BACKGROUND

2.1 Deoxyribo Nucleic Acid (DNA)

A DNA molecule in an organism contains all the genetic information necessary to ensure the normal development of that organism. Therefore, they occupy a unique position in the biochemical world.

The DNA monomers, which are referred to as nucleotides (nt), consist of three subunits: a deoxyribose sugar, a base and a phosphate group [Saenger, 1983]. Linking of the 3' and 5' OH of the sugar units via phosphodiester bonds creates a DNA strand. The resulting ends of a DNA strand are designated as 3' and 5'-terminus. The C1 atom of the ribose is attached to one of the four naturally occurring bases, the purines, adenine and guanine, or the pyrimidines, cytosine and thymine. In single-stranded (ss) DNA, the distance between two successive phosphates is about 0.7 nm. In a DNA hybridization reaction, two complementary single strands of DNA become oriented in an anti-parallel manner to form double-stranded (ds) DNA via Watson Crick base pairing like the one depicted in Fig. 1 [Watson, 1953].

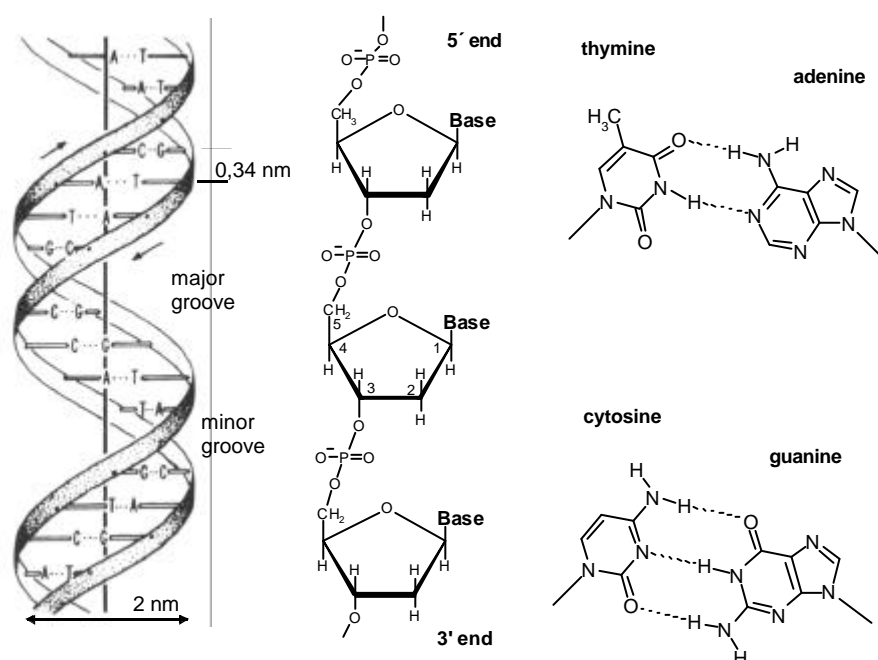


Figure 1: Schematic representation of the double helix (left) showing the minor and the major groove, a DNA single-strand illustrating the way the sugar units are linked via the H-bonding between specific Watson-Crick base pairs (right) and phosphodiester bridges (middle).

James Watson noted that hydrogen-bonded base pairs with the same overall dimension could be formed only between A and T, and also G and C (figure 1). The A-T base paired structure has two hydrogen bonds, whereas the G-C base pair has three. The hydrogen bond pairs are formed between bases of opposing strands and can only arise if the directional senses of the two interacting chains are opposite [Zubay et al, 1995]. This structural information has been also proven by Francis Crick using X-Ray diffraction pattern. The results were interpreted in terms of a helix composed of two nucleotide strands. In this structure, the planes of the base pairs are perpendicular to the helix axis and the distance between adjacent pairs along the helix axis is 3.4Å. The structure repeats itself after 10 residues or once every 34 Å along the helix axis [Zubay et al, 1995].

The stability of the DNA double helix structure depends on several factors. The negatively charged phosphor groups are all located on the outer surface where they have a minimum effect on each other. The repulsive electrostatic interactions generated by these charged groups are often partly neutralized by the interaction with cations such as Mg^{+2} [Tinland, 1997].

The process of separating the polynucleotide strands of a duplex nucleic acid structure is called denaturation. Denaturation disrupts the secondary binding forces that hold the strands together. These secondary binding forces are the hydrogen bonds in between the base pairs of opposing strands and the stacking forces between the planes of the adjacent base pairs. Individually these secondary forces are weak but when they act together, they give a high stability to the DNA duplex in an aqueous solution.

The melting temperature, T_m , of the DNA is sequence-dependent thermodynamic stability of DNA in terms of nearest-neighbor (n-n) base pair interaction and defined as the temperature at which 50% of the DNA becomes single stranded [Geoffrey, 1995]. The T_m is primarily determined by double stranded DNA (dsDNA) length, degree of GC content, the higher the mole percentage of the G-C base pairs, higher the T_m is since the G-C base pair contains three hydrogen bonds whereas the A-T base pair has only two, and degree of the complementarity between strands.

Other factors present in the aqueous solution can also affect the stability of the strand. For example, salt has a stabilizing effect on DNA strands by acting on the repulsive electrostatic interactions between negatively charged phosphate groups of the DNA. Salt ions shield the charges and therefore stabilizes the duplex structure.

2.2 Peptide Nucleic Acids (PNAs)

PNAs are nucleic acid analogs composed of neutral psuedopeptide/protein-like backbone with regular or modified nucleobases [Nielsen et al, 1991].

In recent years, PNAs have become more popular in gene-targeted drug development and molecular biology tools due to some advantages that PNA shows as compared to the other analogues. One of the reason for this is the fact that PNA oligomers are virtually resistant to degradation by nucleases, which insures the stability of the PNAs in plasma and cell extracts [Nielsen, 2002].

As shown in Fig.2 in PNA the negatively charged backbone of the DNA is completely replaced by a neutral psuedopeptide. Thus, the usual electrostatic repulsion between complementary strands is absent resulting in a more stable duplex formation with a DNA strand. PNA also hybridizes with very high affinity and specificity to the complementary DNA. The thermal stability of a duplex increases in the series DNA-DNA<PNA-DNA<PNA-PNA.

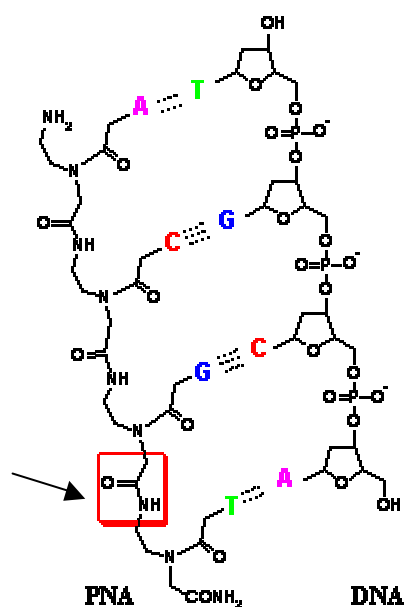


Figure 2: The structure of PNA and hybridization scheme with DNA strand.

Beside all the advantages of PNA, its solubility properties are problematic, e.g it is less soluble in water. But, as it will be described in sections 4.1 and 4.2, this solubility issue can be improved by modifying the bases. As we will be discussing later,

modifications that have been done to increase the solubility have also increased the affinity of the binding PNA to the complementary DNA strand.

2.3 Detection of DNA Hybridization on Surfaces

Biosensors are devices that combine a biological recognition element, which gives selectivity, and a transducer, which provides sensitivity and converts the recognition event into a measurable signal [Collings et al, 1997]. The biological recognition element can be for example a single-stranded or double stranded either natural or synthetic oligonucleotide [Tombelli et al, 2001].

The recognition event is a hybridization reaction between a surface immobilized probe and a target. A sequence of bases forming the oligonucleotide on the sensor is called the probe. Its complementary strand from solution is called target. The probes are generally short oligonucleotides which are immobilized on a selected surface and coupled to an optical, electrochemical, thermal or mass sensitive transducers whereas targets are freely dissolved in solution.

Optical biosensors are sensitive to changes in the optical properties in a solid/liquid interface upon any interaction between probe and target. This change might result either in a refractive index change, luminescence or fluorescence. Foremost important for any surface detection method is that only a specific adsorption process of interest is measured while any other non-specific processes do not contribute significantly to the final result. Optical biosensors offer several assets among other biosensor types: (1) generally there is no need to label the molecules being detected; (2) many important biological recognition takes place at surfaces; (3) the signal/noise ratio is better and hence the sensitivity is higher and (4) they can be used to monitor recognition processes in real time and in situ [Homolo, 2003].

The concept of detecting DNA hybridization on a surface has been widely employed using various optical surface techniques including surface plasmon spectroscopy [Kambhampati et al., 2001, Jordan et al., 1997 McDonnell, J. M. et al., 2001], waveguide spectroscopy [Plowman, 1996], fibre optics evanescent wave spectroscopy [Scheller et al., 2001] and quartz-crystal microbalance methods [Yun et al., 1998 and Qian et al., 1998].

2.4 Genetically Modified Organism (GMO):

Genetically modified organisms are defined as living organisms whose genome has been modified by the introduction of an exogenous gene, which is able to express an additional protein that confers new characteristics [Mariotti et al., 2002].

The foreign DNA is usually inserted in a gene cassette consisting of an expression promoter, a structural gene, which has an encoding region and an expression terminator.

Considering GMO plants, a new gene can confer herbicide tolerance, fertility/maturation modification or parasite, virus, fungi, drug or insect resistance. The pesticide ‘Roundup’ works by inhibiting an enzyme that is necessary for the plant to synthesis certain aromatic aminoacids that are killing the plant. The targeted enzyme is called 5-enolpyruvyl shikimate-3-phosphate synthase (EPSP). The genetic modification in Roundup Ready soybeans involves the incorporation of a bacterial version of this enzyme into soybean plant to give a soybean protection against Roundup [Minunni et al., 2001].

2.5 Detection of GMOs in food chain and EU regulations in GMO contained food labeling

There are several issues concerning health and safety since GMOs are introduced to the market. The general public concerns about the risk assessment of GMO products because many GMO products are used as foods. Environmental concerns derived from the result that GMO product effects on components of the ecosystem are not easily observable in the short-term. Those are all because of the lack of knowledge on the effects of many health-positive, intrinsic plant compounds on the following issues [Kuiper et al, 2003].

- which compounds exert beneficial affects
- mechanisms of health promoting effects and of potential toxicity
- bioavailability of compound of interest
- matrix effects of on bioavailability and metabolism
- interaction between bio-active compound
- dose-response relationship of protective and adverse effects
- losses or modifications of compounds through food processing

Due to these facts, the detection of GMOs became socially and politically important in many countries. Hence many countries have developed their own laws controlling the marketing of GMOs [Kok et al, 2002]. While, for example, labelling is not required in the US, in the EU it is mandatory. In the EU, the directive 90/220 regulates the approval and the release of the GMOs.

Raw material and processed products like foods derived from GM seeds might be held apart by testing for the presence of introduced DNA or by detecting expressed novel proteins encoded by genetic material. Both qualitative and quantitative methods which give a yes/no answer are available [Tzu-Ming Pang, 1991].

Quantitative detection methods are needed for the enforcement of the labeling threshold for GMOs in food ingredients. The labeling threshold is set to 1% in the European Union and Switzerland and must be applied to all GMOs. Until now, four different varieties of maize, insect-resistant Bt176 maize, Bt11 maize, Mon810 maize and herbicide tolerant T25 maize are approved in the EU [Broadman et al,2002].

Some analytical methods are already available for GMOs detection, based on detection of a) exogenous DNA and b) of proteins.

2.5.1 DNA Based detection Methods:

2.5.1.1 Polymerase Chain Reaction (PCR)

One method for the detection of the transgenic material in DNA is “the real time Polymerase Chain Reaction (PCR)” approach.

PCR entails the enzymatic amplification of specific DNA sequences, target strand, using two oligonucleotide primers that flank the DNA segment to be amplified and give millions of the original copy (Fig.3).

A cycle consists of each set of the three steps as described below. The extension products of one primer provide a template for the other primer in a subsequent cycle so that each successive cycle essentially doubles the amount of DNA. This results in the exponentially accumulation of the specific target fragment by approximately 2^n , where n is the number of the cycle. The specific target fragment is also referred to as the “short product” and is defined as the region between the 5`ends of the extension primers. Each primer is physically incorporated into one strand of the short product.

Other products are also synthesised during the succession of the cycles, such as “long products” of indefinite length, which are derived from the template molecules. However the amount of the long product only increases arithmetically during each cycle of the amplification process because the quantity of the original template remains constant.

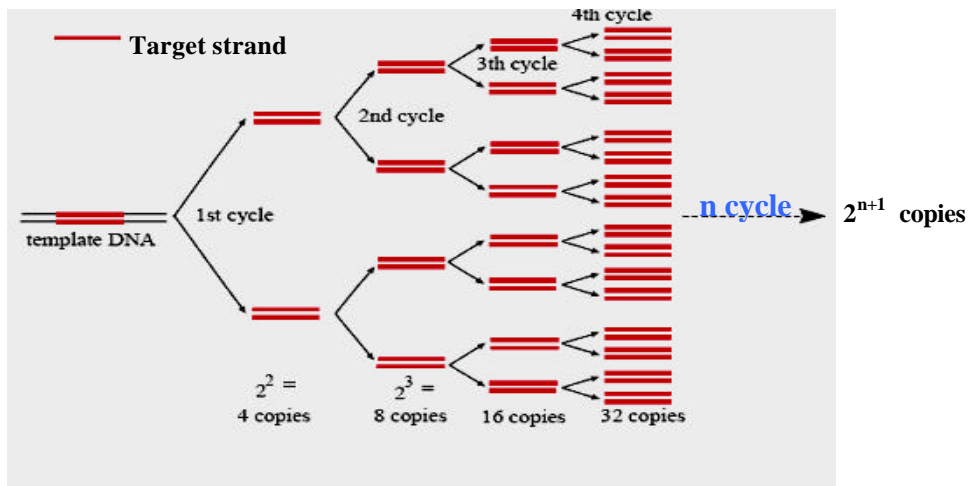


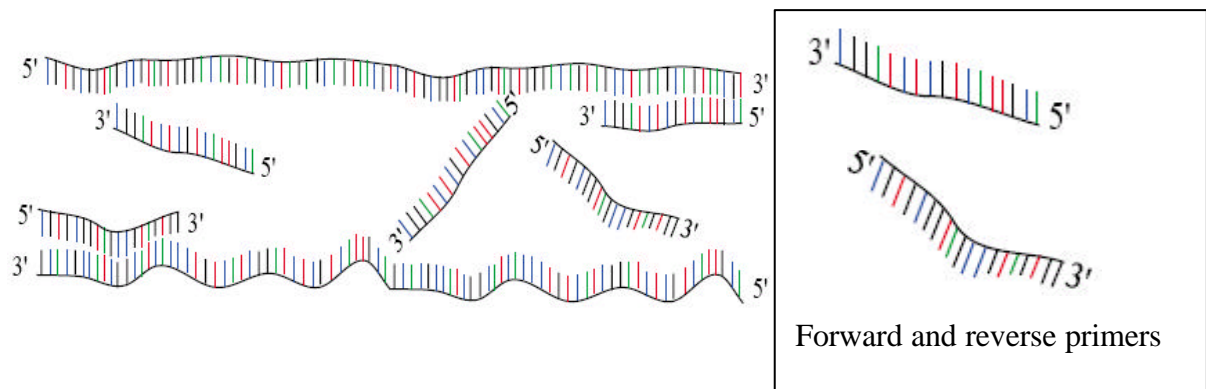
Figure 3: Target strand amplification by PCR (<http://allserv.rug.ac.be/~avierstr/pdf/PCR.pdf>)

The PCR procedure has three steps, which are usually repeated many times in a cyclic manner.

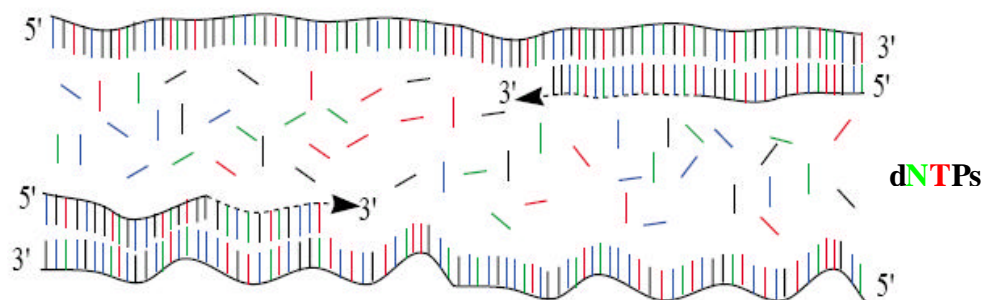
1. Denaturation Step: Denaturation of the original double-stranded DNA at high temperatures



2. Annealing Step: Annealing of the oligonucleotide primers in the DNA template at low temperature.



3. Extension Step: Extension of the primers using DNA polymerase.



2.5.1.2 Real Time PCR:

Real time PCR is the PCR method, which is able to detect sequence-specific products as they are accumulated in real time during the PCR amplification process. Real time PCR uses a fluorescently labeled oligonucleotide probe, which eliminates the post-processing step. This real time system utilizes the intercalator ethidium bromide that binds to the double stranded DNA. The amplification results thus in increased fluorescence. Once the PCR amplification begins, DNA polymerase cleaves the probe and the reporter dye is released from the probe. Each reporter dye that is released during the each cycle generates a sequence-specific fluorescent signal. As cycles go, the fluorescence increases proportionally.

This technique is capable of screening the genetic activity by using a minimal amount of sample and being specific at the same time.

2.5.2 Protein Based Testing Methods:

Immunoassay technologies with antibodies are a good way for quantitative and qualitative detection of many types of proteins in complex matrices when the target analyte is known. Both a monoclonal antibody, which is highly specific, and a polyclonal one, which is often more sensitive, can be used depending on the particular application, time and cost. The detection limit of a protein immunoassay can predict the presence of modified proteins in the range of 1% GMOs. Immunoassays with antibodies attached to a solid support have been used in two formats:

1. a competitive assay in which the detector and analyte compete to bind with capture antibodies.
2. two sided (double antibody sandwich) assay in which the analyte is a sandwich in between the capture antibody and the detector antibody [Cochet et al., 1998].

2.5.2.1 Western Blot

The Western blot is an highly sensitive, particularly useful method for soluble proteins. It provides qualitative results for determining whether the sample contains a target protein in the amount that exceeds the threshold limit or not. The samples that will be assayed, are solubilized with detergents or reducing agents and separated by Sodium Dodecyl Sulfate-polyacrylamide gel electrophoresis. Those components are then transferred to a solid support such a nitrocellulose membrane and binding immunoglobulin sites on the membrane are blocked by dried nonfat milk. Western Blot analysis can only detect one protein in the mixture of any number of others. However sensitivity of this method is highly dependent on the selected antibody's specificity to the corresponding protein.

2.5.2.2 ELISA (Enzyme Linked Immunosorbent Assay)

ELISA is a good testing method to estimate the amount of the target material in ng/ml to pg/ml concentrations in solution. Based on the principle of antibody-antigen interaction, it combines the specificity of antibodies with the sensitivity of the enzyme assay systems.

Beside being used in clinical testing, it has also started to find a place in GMO detection in recent years. Some companies like GeneScan and AgroGene use an ELISA based method to quantify alien DNA in products.

In an ELISA test for genetically modified agricultural products, the biologically engineered gene is isolated and antibodies are raised against specific surface structures of this protein. If the protein is available in the sample, it is bound to the walls of the test holder and react with tagged antibodies resulting in a change of colors which can be detected by a fluorescence scanner.

2.5.2.3 Lateral flow strip

Lateral flow tests, or immunochromatographic strip tests (ICS) are performed with a visually detectable solid support (strip), to which basically any ligand can bind. According to the type of the ligand molecule, e.g. dyed microspheres, qualitative determination or semi quantitative detection might be performed.

Commercial test kits for Roundup Ready soybean genes are available from many companies such as Strategic Diagnostic Inc., Naogen Corp., Enviroogix Inc. etc. (www.usda.gov). However, according to a reviewed article in *The International Journal of Food Science and Technology*, the ICS tests gave false negative results more than 30% of the time for samples containing 0.5% and 1% GMO soybeans.

There are a number of technologies currently available that can be used to overcome the disadvantages of those methods. For example, Surface Plasmon Microscopy (SPM) and Spectroscopy (SPS), Surface Plasmon Fluorescence Microscopy (SPFM), and Spectroscopy are currently available methods to observe biomolecular interaction either in an array or on a surface in real time.

2.5.2.4 The Nucleic acid sequence-based amplification (NASBA):

The Nucleic acid sequence-based amplification (NASBA) technique amplifies an RNA target molecule. One of the primers contains a T7 promoter, which allows for the production of a RNA molecule after cDNA synthesis. There are some methods to detect the antisense RNA molecules, among which FRET and molecular beacon methods are the most suitable ones. A disadvantage of this type of technique is that the test is based on the detection of RNA. It has the tendency to degrade easily and

therefore it's only detectable in intact cell systems, which are also hard to work with. Because of the varying expression level, the quantification of the GMO content with this method is not straightforward.

2.6 Microarrays

Microarrays are comprised of large sets of nucleic acid probe sequences which are immobilized in defined, addressable locations on the surface of a substrate. Microarrays are capable of acquiring huge amounts of genetic information from biological samples through single hybridization procedure.

In the late 1960s, Pardue and Gall [Pardue et al., 1969] and Jones and Robertson [Jones et al., 1970] discovered a way of locating the position of specific sequences in the nucleus or in chromosomes. They used hybridization reactions on a cell fixed to a microscope slide. This method allowed DNA to take a part in duplex formation with the probe that is being used to fix DNA spotted slides in one microarray method.

In the mid 1970s, recombinant DNA methods have been developed and the front of discovering new genes had been opened [Grundstein and Hogness, 1975].

One attractive method for monitoring biomolecular interactions is high throughput analysis and in this context, the microarray technique takes the most favourable place. Microarrays have been used in genomic work, gene expression, protein screening and the recently growing area of genetically modified organism (GMO) detection using extremely limited amounts of biological samples.

Modern drug discovery efforts require the screening of millions of compounds in a high throughput format before novel therapeutic moieties can be identified. The same is true for all kinds of assays, which are performed in several hundreds of thousands in certain disease categories.

2.6.1 Making microarrays

Printing is an easy and cheap way to produce a microarray among other surface patterning techniques e.g, microcontact printing.

Printing of an array can be categorized according to following aspects: choice of (1) the spotting system, (2) the surface chemistry for probe attachment, and (3) the spotting solution.

(1) Spotting System

The choice of the spotting system is important for controlling the drop volume, spot size and the homogeneity. A spotting device can either release the drops (ink-jet spotter) or leave them as a result of a contact between pin and the surface (pin-tool spotter)

The ink-jet nanoplotter is a non-contact spotting equipment which allows for the user to control the volume of the spotting reagent. The droplet volume is controlled by a piezo pump (See Figure 4). The spot diameter is usually between 100-200 μm .

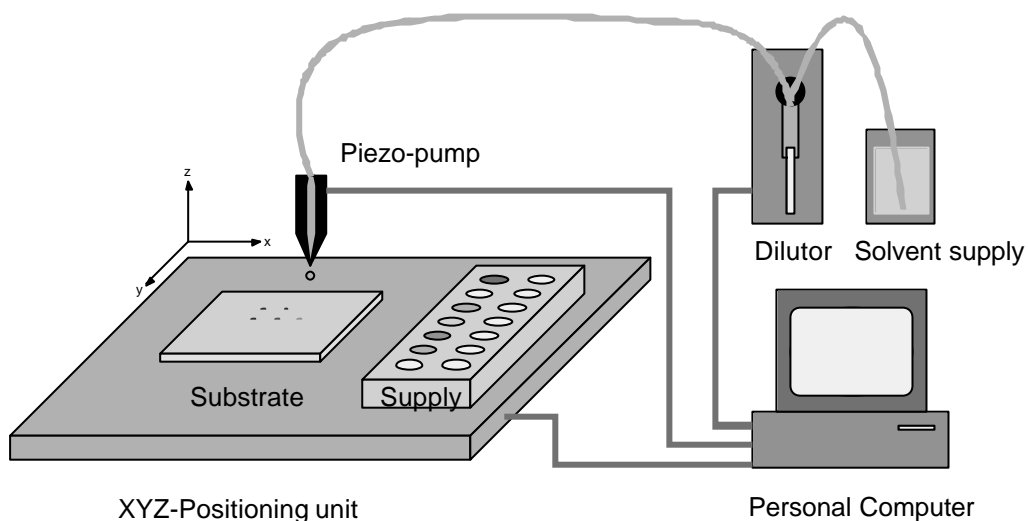


Figure 4: Ink-jet spotter

The pin-tool nanoplotter is a contact mode spotter (fig.5a). Silicon tips or commercial steel pins require the application of force on the pin in order to press the print tip surface against the substrate to print satisfactorily as schematically shown in Fig.5b.

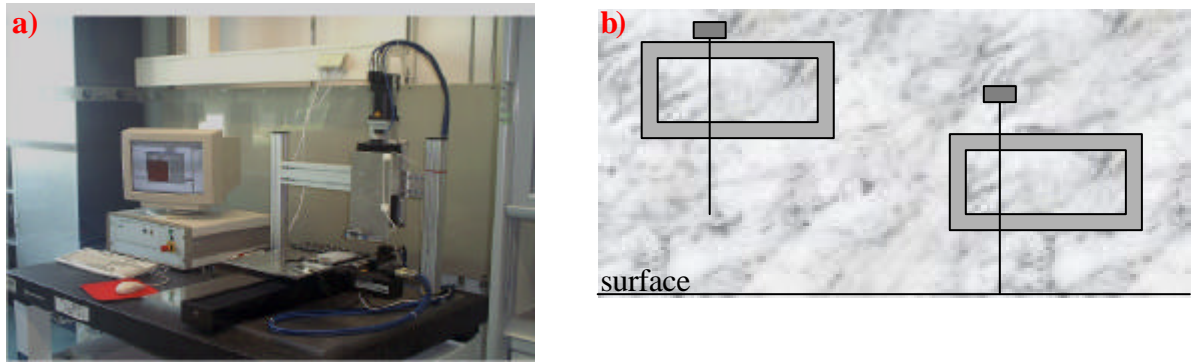


Figure 5: a) Pin Tool spotter and b) Tip position from surface

The spot diameter can be controlled by changing the pin type. There are usually 2 different kinds of pins: Solid pins and split pins as shown in Fig.6

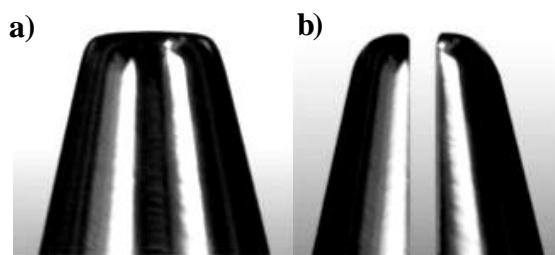


Figure 6: a) Solid pin, b) Split pin (www.pointech.com)

Beside steel pins, silicon tips are also common to use. They are manufactured from extremely flat, highly polished single-crystal silicon wafers by a series of lithographic operations and therefore each tip is a single crystal silicon tip except for their thin SiO₂ coating. This coating layer plays an important role in liquid handling, wettability, cleaning and chemical resistivity.

Silicon tips have certain advantages with respect to steel tips. First, the volume uptake in silicon pins is less than that of steel ones. (25-250nl per dip vs. app. 1-2 μ L). Another important point is that the cost of a silicon tip is around 25% of the steel pins ones. The hardness of the tip is higher in the silicon tip. That gives deterioration resistance to the tip.

(2) Surface chemistry for probe attachment

Surface chemistry is the most critical issue for the stability of the array. No matter what printing system is being used , the surface chemistry defines the specificity of

the array. Some of the commercial array chemistry sometimes requires 5' amino linked primers in the polymerase chain reaction (PCR) amplification in order to generate the probe, but generally poly-L-lysine or silane coated slides are used. More recently, superior glass of uniform thickness, monolayer branched polymer slides have become popular.

A Biotin/streptavidin matrix is another widely used surface architecture for oligonucleotide attachment to the surface. As it will be mentioned later again, this approach has been used in our studies.

(3) Spotting Solution

In some cases, the probe suspending solution is being used in order to alter the nature of the spot. Traditional arraying methods involve the spotting of oligonucleotides in salt-buffer solution, but the use of surfactants contributes to a more even deposition of the material on the glass substrate [B. Jordan, 2001]. The selection of the spotting solution is often determined by the chemistry that is used to attached DNA elements to the substrate. As can be seen in Fig.7, the spots using spotting solution are better defined in shape.

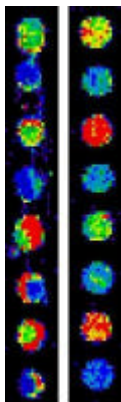


Figure 7: Effect of spotting solution on spot quality, right image is without spotting solution and the left one is with spotting solution (www.telechem.com)

2.7 Fluorescence

During the past years, the use of fluorescence techniques in biological sciences has increased dramatically, especially for the observation of cell growth, clinical chemistry and genetic analysis [Mary-Ann Mycek, 2003]. Because of that growing interest, the instrumental part has been developed even though the basic fluorescence principle is used. In this chapter, these basic principles of the fluorescence phenomena will be described.

2.7.1 The Phenomena of the Fluorescence

The emission of light from a system is always a response to a process that brings energy to the system. This response varies from biological response (bioluminescence) to radioactive interaction. Luminescence is the emission of light from any substance and involves any electronically excited states and can be divided into two categories: Fluorescence and phosphorescence, depending on the nature of the excited state.

Fluorescence is a phenomenon that describes emission of photons from molecules that undergo a transition from an electronically excited state to the ground state [Lakowicz J.R, 1983]. The processes that occur between the adsorption and emission of light are illustrated by a Jablonski diagram [Mary-Ann Mycek, 2003].

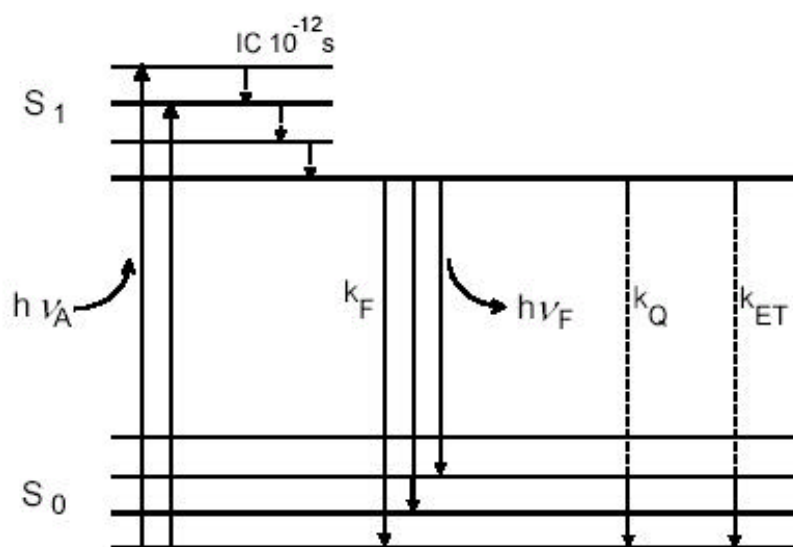


Figure 8: Jablonski energy level diagram

The scheme in Fig.8 shows different electronic states, the electronic ground state designated as singlet (S_0) and the first excited singlet state, S_1 . In each of these electronic states, the molecule can exist in a number of vibrational levels, which are populated according to the Boltzmann distribution law. The molecule exists in the lowest vibrational state of the electronic ground state prior to photon absorption. In the Jablonski diagram, the vertical lines indicate the nature of light absorption. After absorption of the light, transitions occur within 10^{-15} s. A fluorophore is usually excited to higher vibrational level of S_1 or S_2 (not shown here). The absorption spectrum therefore reveals information about the electronically excited states of the molecule. With a few exceptions, molecules in condensed phases rapidly relax to the lowest vibrational level S_1 . This process is called “internal conversion” and generally occurs on a time scale of 10^{-12} s. Since the fluorescence lifetime is typically near 10^{-8} s, this process is generally completed prior to emissions. Hence the fluorescence emission generally results from thermally equilibrated excited state, which is the lowest-energy vibrational state of S_1 . From there, the molecule can decay to different vibrational levels of the state S_0 by emitting light. This leads to fine structure of the emission spectrum by which information can be gained about the electronic ground state S_0 .

If a comparison is made between emission and absorption spectra, one can observe that the energy of the emission is typically less than that of the absorption. Hence, fluorescence occurs at lower energies or, in other words, at longer wavelengths. This phenomena was first observed by Sir G.G. Stokes, it has been called “Stokes’ shift”. This shift can be explained by considering the energy lost between two process due to the rapid internal conversion in the excited states (S_1 and S_2) and the subsequent decay of the fluorophore to higher vibrational levels of S_0 . This shift is fundamental to the sensitivity of fluorescence techniques since it allows the emitted photons to be isolated from excitation photons detected against a low background.

2.7.2 Fluorescence Lifetime and Quantum Yield

The fluorescence lifetime and quantum yield are the two most important parameters in a fluorescence process. The quantum yield is the number of emitted photons relative to the number of absorbed photons. The higher the quantum yield is,

approaching the unity, the brighter the fluorescence will be. The life time is also important since it determines the available time for a fluorophore to diffuse or interact with its surroundings and give information about it, as shown in the emission spectrum. These two parameter are best illustrated in a Jablonski Diagram.

In Fig.8, the relaxation process does not illustrate in detail all the relaxation leading to the relaxed S1 state. Instead, it outlines the processes returning the molecule to the ground state and emphasizes the two terms of importance which are the emissive rate of the fluorophore (Γ , which equals to $h\nu_F$) and its rate of nonradiative decay (k_{nr}) to S_0 . The process is governed by these two terms both deplete and excited state. Therefore, the fraction of the fluorophores which decay through emission, this is essentially the quantum yield, is given by the following equation.

$$Q = G / (G + k_{nr}) \quad (eqn.1)$$

If $k_{nr} \ll \Gamma$, the radiationless decay is much smaller than the radiative decay, i.e., the quantum yield can be close to unity. However, we know from Stokes' losses that the energy yield of fluorescence is always less than unity.

The lifetime of the excited state, on the other hand, is defined by the average time the molecule spends in the excited state prior to returning to the ground state. Generally fluorescence lifetimes are in the range of 10ns and this can be illustrated with the formula;

$$t = 1 / (G + k_{nr}) \quad (eqn.2)$$

The quantum yield and fluorescence life time can be both influenced by all factors that influence the rate constants k_{nr} and Γ . Because of a very fast rate of internal conversion or very slow rate of emission, a molecule might not be fluorescent.

2.7.3 Fluorescence Quenching

The intensity of the fluorescence can be decreased by many processes. This decrease is known as quenching [Macdonald, R. I.1990, Roberts, K. E et al., 2003].

Quenching can be caused by mechanisms such as the physical interaction with other molecules in solution while the fluorophore is in the excited state. In that case the mechanism is called “collisional quenching” and the molecule “quencher”. In this case, the fluorophore returns to the ground state during the diffusive encounter with the quencher. The molecules are not chemically altered during the process. The decrease in the fluorescence intensity due to collisional quenching is well described by the Stern-Volmer equation:

$$F / F_0 = 1 + K[Q] = 1 + k_q \tau_0 [Q] \quad (\text{eqn.3})$$

The term K in this equation is the Stern-Volmer quenching constant, k_q is the bimolecular quenching constant, τ_0 is the unquenched lifetime, and $[Q]$ is the quencher concentration. A wide variety of molecules, for example, oxygen, halogens, amines and electron-deficient molecules like acrylamide can act as collisional quenchers.

Beside collisional quenching, there are other ways to cause fluorescence quenching. One of them is that fluorescent molecule can form a non-fluorescent complex with the quencher. This process refers to a static quenching since it occurs in the ground state and does not rely on molecular collisions or diffusion. Quenching can also occur by other trivial mechanisms such as attenuation of incident light by the fluorophore or other absorbing species.

2.7.4 Photobleaching

A typical fluorophore can undergo a finite number of excitation-relaxation cycles prior to photochemical destruction. This process is often referred to as photobleaching. For a photostable fluorophore, e.g. tetramethylrhodamin, photobleaching occurs after about 10^5 cycles. In contrast, some molecules, like fluorescein, photobleach very easily. Generally speaking, the photobleaching involves the generation of reactive oxygen molecules, thus it is sometimes useful to introduce antioxidants or to use anoxic conditions. On the other hand, the rate of the photobleaching is often proportional to the intensity of illumination. Therefore, a simple practical way to overcome this is to reduce the time or the intensity of the excitation radiation.

2.8 Langmuir Adsorption

The Langmuir isotherm was developed by Irving Langmuir in 1916. This model describes the dependence of the surface coverage of an adsorbed gas on the pressure of the gas above the surface at a fixed temperature. There are many other types of isotherm that differ in the assumption made in deriving the expression for the surface coverage. [Ulman, 1991].

The recent development of evanescent wave biosensors offers an access to the kinetics of a biomolecule in the solution reversibly interacting with another biomolecule, which is immobilized on the solid surface. The conventional treatment starts with a simple 1:1 interaction model [Schuckannu, P., 1997] equivalent to the Langmuir adsorption isotherm [Atkins, 1998] based on the assumptions listed below:

- a limited number of binding sites is available
- all binding sites can be occupied by binding molecules until the complete surface is saturated and all sites are blocked
- all binding sites are equivalent and already occupied sites do not influence the binding reaction in adjacent sites
- the surface is homogeneously covered by a monolayer

The process of the binding to the surface can be described by the rate constant, k_{on} and the one that describes the desorption from the surface is k_{off} as shown in Fig.9.

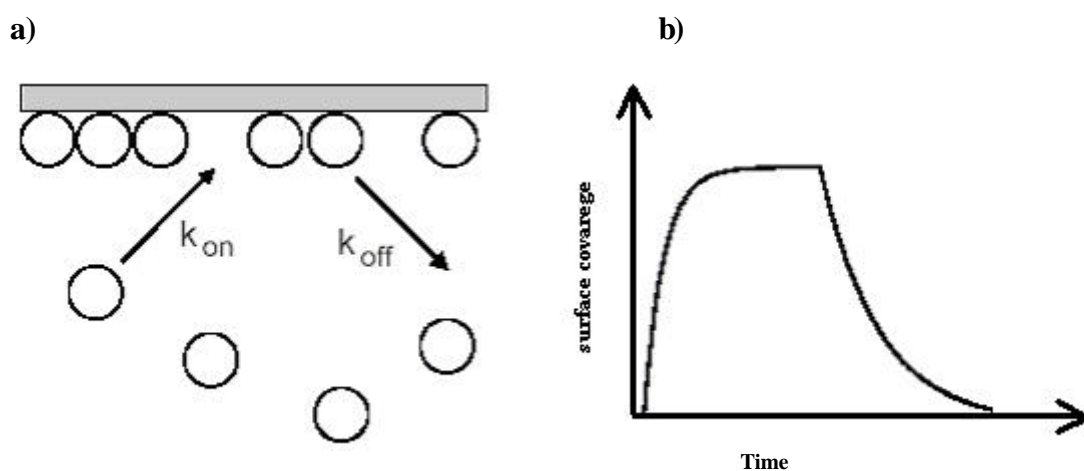


Figure 9: Schematic description of Langmuir adsorption. As it can be seen from the graph, the surface coverage is dependent on adsorption and desorption rate constants, k_{on} and k_{off} respectively.

The adsorption mechanism can be described as an equilibrium between surface bound molecules and molecules which are free in solution. The process of association involves the binding of the analyte from solution onto the interface while the dissociation process entails the detachment of bound analyte that then diffuse back into solution. The resulting time dependent surface coverage, Θ , can be described by the following expression;

$$\frac{\partial\Theta}{\partial t} = k_{on}C(1 - \Theta) - k_{off}\Theta \quad \text{Eqn. 4}$$

in which c_0 is the analyte concentration. One can see that the higher the analyte concentration is, the faster the surface binding reaction is. On the other hand, the desorption process has no relation with the analyte concentration and only depends on the dissociation rate constant, k_{off} , and the surface coverage. If we combine eqn.4 with the initial equilibrium conditions, i.e., surface coverage, $\Theta=0$ at $t=0$, we can derive the following eqn.

$$\Theta(t) = \frac{c_0 k_{on}}{c_0 k_{on} + k_{off}} (1 - \exp(-(c_0 k_{on} + k_{off})t)) \quad \text{Eqn.5}$$

The typical solution of this equation is given in fig.9-b, where the adsorption process leads to the equilibration of the system at a certain surface coverage, which is dependent on both rate constants. In the case of a real experiment the desorption process can be followed separately by exchanging the analyte solution against pure buffer, since the concentration c_0 equals to zero and the first expression in eqn.5 becomes negligible. The rate constant k_{off} can thus be derived by the consideration of desorption alone with the simulation of experimental data following eqn 6.

$$\Theta(t) = \Theta_0 \exp(-k_{off}t) \quad \text{Eqn.6}$$

where Θ_0 is the initial surface coverage at the beginning of the desorption process. For simplicity, it's assumed that any re-binding of already rinsed off analyte is negligible.

In order to complete the experimental justification of the Langmuir isotherm, a titration process can be performed. The titration process is the stepwise saturation of

the surface with a known concentration of the analyte and allowing adsorption to reach equilibrium. A new analyte solution with higher concentration is then injected and allowed to equilibrate. This process is repeated until no more surface binding is observed for the next analyte solution of higher concentration. Such titration procedure allows each subsequent step to begin with a value of Θ_0 higher than zero. Solving eqn.6 with this initial conditions ($\Theta_0 = \Theta$ at $t=0$ because of the higher surface coverage already in place when adsorption is allowed to occur) leads to a solution of the form;

$$\Theta(t) = \frac{c_0 k_{on}}{c_0 k_{on} + k_{off}} \left(\Theta_0 - \frac{c_0 k_{on}}{c_0 k_{on} + k_{off}} \right) \exp(-(c_0 k_{on} + k_{off})t) \quad \text{Eqn.7}$$

The simplest relation of surface coverage to equilibrium constant K of the surface reaction can be derived from eqn .4

$$\Theta = \frac{c_0 K}{1 + c_0 K} \quad \text{Eqn.8}$$

This might be the most significant equation in the Langmuir model since it allows direct calculation of the general equilibrium constant K from two simple experimental parameter like analyte concentration and surface coverage. For the fluorescence experiment, the surface coverage Θ is determined by scaling the detected signal intensity against the theoretical maximum intensity obtained at total surface saturation.

In reality, some limitations of the model have to be taken into account. The surface coverage is mass transport limited if the analyte concentration is too low, analyte molecules are too small or the lateral deposition density is too low. This case is usually seen in titration measurements where the surface is started to be “decorated” with the target molecule from very low concentration. In the fluorescence measurement, the exchange rate between bound species and free species can bring upon large influence in the measured signal due to detrimental effects of the photo-bleaching and the possibility of recombination with the washed away molecule is also not avoidable.

2.9 Evanescent Optics

Because of the fast progress in sensor technology, the need of high sensitivity and specificity has become a crucial issue. One way to fulfill that requirement is the combination of sensors based upon Surface Plasmon Resonance Spectroscopy (SPR) [Knoll, 1997]. These sensors are generally able to detect changes in refractive index down to $\Delta n/n = 10^{-5}$ with a time resolution in the order of seconds [Jung et al, 1998]. SPR methods are surface sensitive techniques that employ the enhancement of the optical fields that occur at metal like Au, Ag, Al, Cu etc. surfaces if surface plasmon polaritons (SPPs) are created at the metal/dielectric interface.

2.9.1 Evanescent Light

The simplest case of the existence of an evanescent wave is the total internal reflection of a plane electromagnetic wave at the base of a glass prism, with an index of refraction n_1 , in contact with an optically less dense medium like air, n_2 ($n_1 > n_2$), shown in Fig.10 [Knoll, 1991].

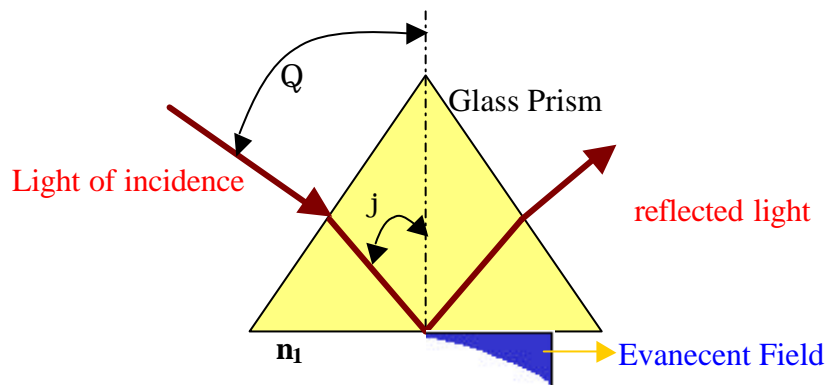


Figure 10: The basic configuration for evanescent optics

The relation between the reflected light intensity and angle of incidence, Θ , is governed by Snell's Law (eqn 9).

$$n_1 \cdot \sin \theta_1 = n_2 \cdot \sin \theta_1' \quad \text{Eqn.9}$$

Upon the increase of the incidence angle θ_1 in Fig.11, one finds that transmission angle θ_2 is increased until the maximum value of $\theta_2 = 90^\circ$ is reached. Since $\sin 90^\circ = 1$, the Snell eqn. turns to eqn9 and then θ_1 is called Critical Angle θ_c which is given by:

$$\sin \theta_c = n_2/n_1 \quad \text{Eqn. 10}$$

At the same time, the intensity of reflected light increases to its maximum, while the intensity of transmitted light is reduced until it vanishes at 90° . This particular angle of incidence is referred to as the critical angle. Upon further increase of θ_1 , the reflection coefficient remains 1, indicating total internal reflection (TIR). The TIR regime is characterized by the existence of a plane wave travelling along the interface. This wave exhibits an electrical field component that decays exponentially in z-direction. The penetration depth, d , of the evanescent field is in the range of the wavelength λ that is used.

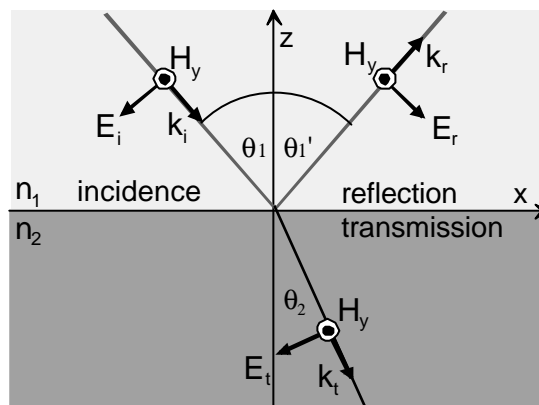


Figure 11: Schematic representation of reflected and transmitted P-polarized light at the interface between two optically different media

2.9.2 Reflection and transmission of light

Imagine a system like the one in fig.11, an interface in the xy-plane between two media with optical properties described by their refractive indices n_1 and n_2 . Coming from medium 1, monochromatic polarized light passes through the medium. Depending on the angle of incidence θ_1 and the optical constants of the materials, a certain part of the light will be reflected and transmitted into the adjacent optical medium with the sum of the energies of these two light waves being equal to that of the original wave.

Since propagating light consists of a transverse electric and magnetic field, the magnetic, $H_{x,y,z}$, and electric field components, $E_{x,y,z}$, can have different orientations parallel or perpendicular to the surface. Two modes of polarization can be distinguished for a wave propagating in the xy -plane:

Transversal magnetic polarization (TM or p-polarized light) with

$$H_x = H_z = E_y = 0$$

and the non-vanishing components E_x , E_z and H_y . The electric field has a component E_z that oscillates in a plane perpendicular to the xy -plane.

Transversal electric polarization (TE or s-polarized light) with

$$E_x = E_z = H_y = 0$$

and the non-vanishing components E_y , H_x , H_z . Here, the electric field only has a field component that oscillates in parallel to the xy -plane.

Below the critical angle for total internal reflection, the reflection differs slightly for s- and p-polarized light. In the following considerations, we will focus on the TM mode since only this mode is able to induce a surface charge density along the z direction, which is the pre-requisite for SP excitation. According to the reflection law, the angle of incidence θ_1 equals the angle upon which reflection occurs at θ'_1 . The transmitted ray is diffracted towards the surface normal according to Snell's law (Eqn.9) with $n_1 > n_2$. Monitoring the reflection R as a function of the angle of incidence yields the reflection spectrum (with $R=I_r/I_0$, where I_r is the intensity of the reflected and I_0 the intensity of the excitation light, respectively). It should be noted that the intensity always corresponds to the square of the electric field, $|E|^2$. The spectrum can be theoretically predicted using a transfer matrix algorithm [Raether, 1988].

The electric field distribution in the immediate vicinity of the interface indicates that, when TIR occurs above the critical angle, Θ_c , the light intensity does not fall sharply to zero in air, in other words, the light intensity does not vanish completely. Instead, a harmonic wave with an exponentially decaying amplitude perpendicular to

the interface is found to be traveling parallel to the surface. Such type of wave is known as an evanescent wave [Deri F. et al, 1985] and its depth of penetration with respect to the interface l is defined by the equation below.

$$l = \frac{\lambda}{2\pi\sqrt{(n_1 \cdot \sin \Theta)^2 - 1}} \quad \text{Eqn.11}$$

2.9.3 Surface Plasmon

Plasmon Surface Polaritons (PSPs) are surface electromagnetic modes that travel along a metal-dielectric interface as bound non-radiative waves, their field amplitudes decaying exponentially perpendicular to the interface [Rather,1988]. They are created by coupling energy from photons into oscillation modes of density at the metal/dielectric interface (Fig.13-a) and formed from light waves. Its electric field vectors or wave vectors are oriented parallel to the plane of incidence. PSPs also have propagation vectors or wavevectors, k_{sp} , that lie in the plane of metal surface.

The dispersion relation (i.e. the energy-momentum relation) for SPs at a metal (ϵ_m)/ dielectric (ϵ_d) interface is given by:

$$k_{sp} = k'_x + ik''_x = \frac{\omega}{c} \sqrt{\frac{\epsilon_d \epsilon_m}{\epsilon_d + \epsilon_m}} \quad \text{Eqn.12}$$

where ω is the frequency of light, c is the speed of light, k_{sp} is the wavevector of the photon and ϵ_m and ϵ_d are the dielectric constant of the metal and dielectric which is often air or water.

Since ϵ_m is complex, the wave vector k_x has to be complex, too, where k''_x represents the damping part of the SP. Consequently, SPs exhibit a finite propagation length L , given by $L_x = 1/k''_x$. The propagation length limits the lateral resolution of SP-based microscopical methods. In a typical experiment at a gold/dielectric interfaces and an excitation wavelength of 630 nm, the lateral resolution will be about 5 μm .

Excitation of the surface plasmon is possible either by electrons or by photons. The previously discussed dispersion relation (eqn.12) has shown that the resonant

excitation cannot be realized by using free photons. The dispersion of free photons is described by the light line:

$$\omega = c_d \cdot k_{ph} \quad \text{with } c_d = \frac{c}{\sqrt{\epsilon_d}} \quad \text{Eqn.13}$$

Relevant for the excitation of SPs is only the projection of the wave vector \mathbf{k} in x -direction. For the simple reflection of a photon with the energy $\hbar\omega_L$ (fig.13-a) the magnitude of the x -component, $k_{ph,x} = k_{ph} \sin \theta$, can be varied by changing the angle of incidence, θ . $k_{ph,x}$ vanishes for perpendicular incidence of light, while it is maximized for large angles of incidence.

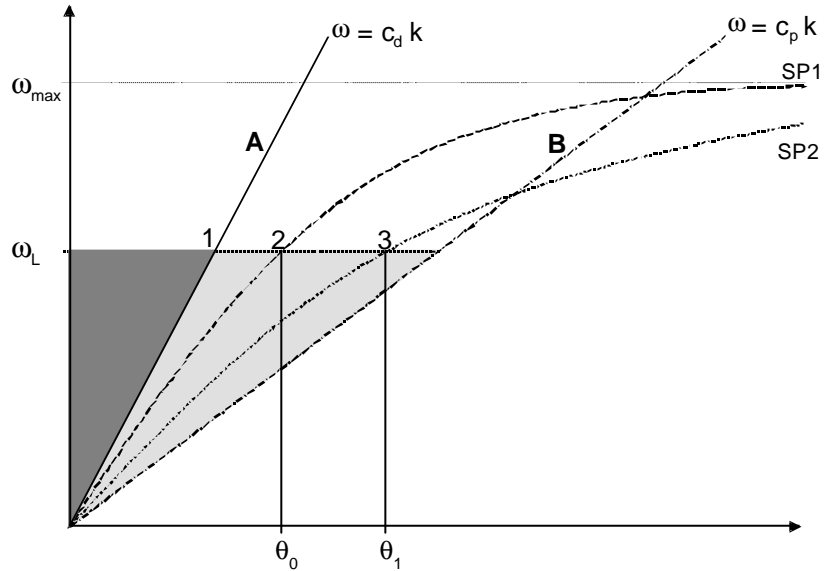


Figure 12: Dispersion relation for A) free photons in a dielectric, B) free photons propagating in a coupling prism, SP1) surface plasmons at a metal/dielectric interface and SP2) surface plasmons after adsorption of an additional dielectric layer [Liebermann, 1999].

A graphical representation of the dispersion of free photons and SP modes is given in Fig.12. The dispersion of photons in the bulk is given as a straight line (A). The SP dispersion curve (SP1) approaches a maximum angular frequency that is attributed to the plasma frequency of the employed metal. Increasing the angle θ from 0° to the grazing angle, tunes the curve from point 0 to point 1 (dark gray area). Because of the asymptotically approach of surface plasmon dispersion curve, SP1, to the line A at very low energies, the momentum matching conditions for resonant surface plasmon excitation cannot be met which means that coupling of the modes is not possible by

changing the angle of incidence alone. Therefore, a way must be found to increase the momentum of light.

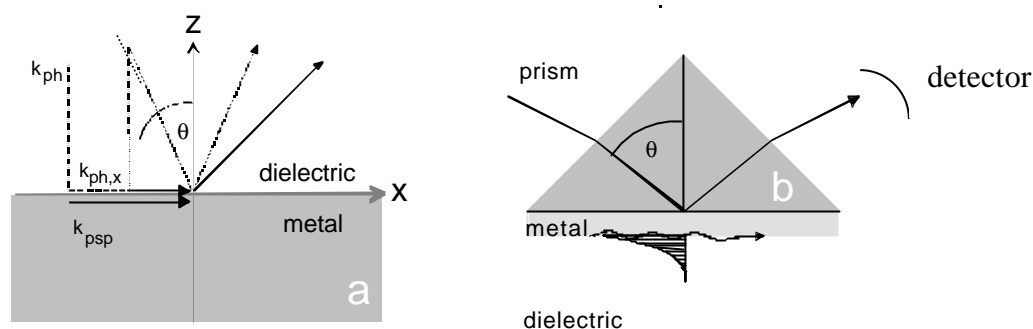


Figure 13: a) Reflection geometry for photons with a momentum k_{ph} at a metal/dielectric interface. The angle of incidence θ determines the absolute value of the momentum in z-direction, $k_{ph,x}$, that is relevant for surface plasmon excitation. b) Kretschmann configuration for momentum matching via prism coupling.

2.9.4 Surface Plasmon with prism coupling

A common way to increase the momentum of light is a method based on prism coupling. Using this method, the photons are not coupled directly to the metal/dielectric interface but via the evanescent tail of light upon total internal reflection at the base of a high refractive index prism ($\epsilon_p > \epsilon_d$) [Otto, A.Z., 1968,]. Line B in Fig.12 describes the increased momentum of photons travelling through a high index prism. By choosing the appropriate angle of incidence (point 2), resonant coupling between the evanescent photons (B) and the surface plasmons (SP1) can be achieved. After adsorption of a dielectric film (SP2) the resonance occurs at an angle corresponding to point 3. The illustration of a prism coupling experimental set-up known as the Kretschmann configuration is shown in Figure 13-b.

The geometry experimentally used in the present work, is the Kretschmann configuration [Kretschmann E, 1968]. As depicted in Fig.13-b, a high index prism is coated with a thin gold layer (~55 nm) adjacent to a lower index dielectric. We have to note that the excitation of the PSPs requires efficient coupling between the metal and the prism. Monochromatic p-polarized laser light is reflected at the base of the prism under an angle of incidence larger than the critical angle. The evanescent field resulting from total internal reflection overlaps with the surface plasmon mode and resonance is achieved by tuning the angle of incidence. If one monitors the intensity

of the reflected light while sweeping through a range of angles, plasmon resonance shows up as a sharp dip in the reflectivity spectrum at the resonance angle, as seen in fig.14.

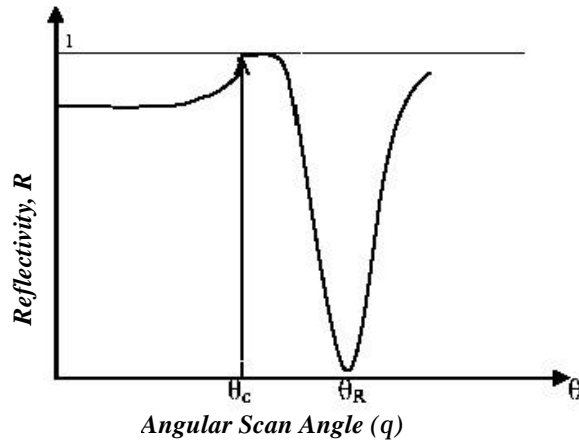


Figure 14: As it was described in the text above, resonant coupling is observed as a very pronounced drop in angular scan of the reflected light intensity at θ_R . θ_c is the critical angle for Total Internal Reflection (TIR).

It is also important to note that the finite thickness of the metal layer does affect the dispersion behavior of the surface plasmon modes. In addition to the intrinsic dissipation of energy in the metal itself, the coupling of some of the light through the thin metal/prism interface creates another channel of radiative loss for surface plasmon which will be discussed in more detailed in section 2.10.1.

2.9.5 Optical Thickness

As illustrated in Fig.12, the dispersion relation of SPs changes when a thin layer of metal is deposited onto prism, effectively shifting the momentum-matching process (from curve SP1 to SP2) and thus the incident angle at which surface plasmon resonance occurs. Further deposition of metal layers or dielectric layer with different dielectric constants will continue to shift the resonance angle (i.e. Fig.15). This is largely due to increase of the overall refractive index detected by the evanescent plasmon field. Consequently, the dispersion relation is shifted towards larger wave vectors, $k_{p2} = k_{p1} + \Delta k$. In this expression k_{p2} and k_{p1} are wave vectors of the system before and after the adsorption, and that Δk is largely influenced by the refractive index and the thickness of the layer absorbed. Such sensitivity to optical thickness is

one of the most fundamental and significant features of surface plasmon resonance spectroscopy.

2.10 Surface Plasmon Fluorescence Spectroscopy (SPFS)

The SPR method offers a label-free, non-invasive and real time detection of various biomolecular events. Most of the times, biomolecules binding events like biotin-streptavidin, result in appreciable shift in the plasmon resonance angle and also during the fixed angle kinetic studies as it can be seen in figure 15.

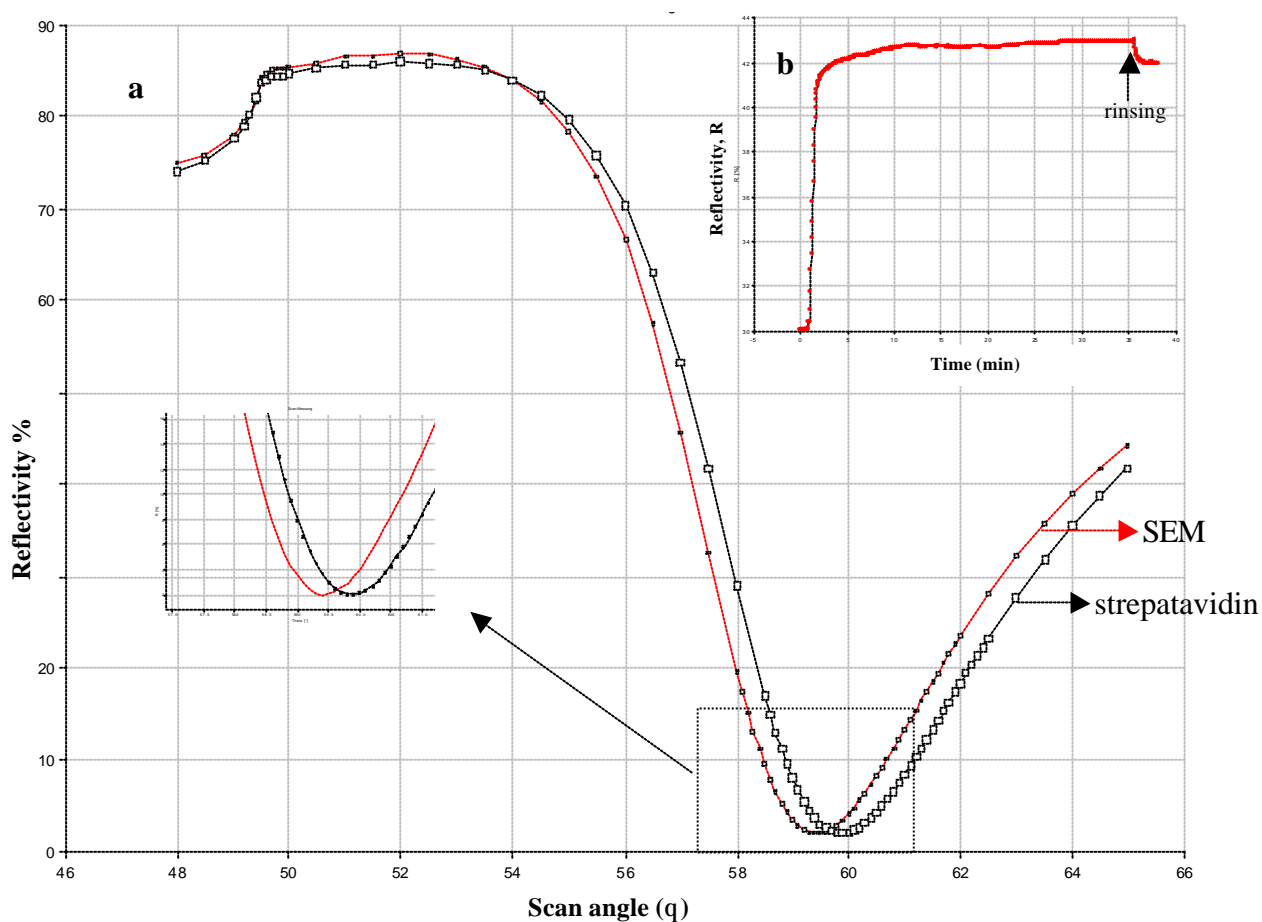


Figure 15: a) Scan curves of Biotin-Streptavidin binding onto biotinylated/OH-terminated thiol modified Au surface. The resonance angle shift is around 0.5 degree since streptavidin is a big bulk molecule that has molecular weight around 60K. b) kinetic curve of streptavidin binding onto same surface. The binding was observed at fixed resonance angle by following the reflective index change in time.

Problems, however, arise if low molecular weight molecules, like short chain DNA molecule or pharmaceutical drugs are involved in binding or if the packing density of the film is very small. For such cases, the resonance angle shifts are very small and SPR is no longer sensitive enough to monitor these binding events or interactions accurately. Under such circumstances, there is a need to incorporate certain signal amplification schemes that can be used in combination with SPR to monitor all these interfacial interactions. Fluorescence tagging of molecules can lead to amplification in the detected signal and thus offers an interesting way of monitoring these low resonance shift events [Knoll, 1985].

The surface plasmon evanescent field can be used to excite the fluorescent dye molecules. But only those chromophores lying within the vicinity of the interface are excited. The emitted fluorescence is strongly dependent on the intensity of the optical evanescent field at a given wavelength and also the probability of the radiative decay of the chromophore from its excited state to the ground state. The optical excitation of the fluorophores follows the evanescent field and since the evanescent field is maximum near the resonance angle, a characteristic increase in the fluorescence signal is observed.

Although the fluorescence coupling with normal SPR results in an enhanced sensitivity, the detected signal is a strong function of the plasmon electromagnetic field. Any external stimuli, which causes a change in the plasmon field will be directly affecting the fluorescence excitation. This effect can be seen if the refractive index of the dielectric medium in contact with the metal changes under the influence of temperature, pressure and the structure of the solvent and the plasmon electromagnetic field is also altered. If the plasmon field changes, the fluorescence excitation level also changes and leads to different fluorescent emission. Thus, if the experimental set-up is designed, those special cases should be taken into account.

Another important point is that the SPFS technique requires the labeling of the biomolecules. That means, every time one labels a biomolecule there is a high probability of secondary effects introduced by the labeling of the biomolecule.

In spite of the limitations that have been mentioned above, the SPFS technique offers a way to observe various biomolecular interactions which can not be monitored by using normal SPR. Since this detection technique is highly sensitive, it is possible to carry out the experiment with a smaller amount of the material. That will help to reduce the cost in the case of expensive materials. As it will be described in the

following sections, the fluorescence microscope, multi-spot detection of various interactions can be also monitored simultaneously leading to high throughput analysis.

2.10.1 Fluorescence at the metal/dielectric interface

The fluorescence emission from the chromophores is strongly dependent upon the distance from the metal surface. Fig.16 illustrates the distance dependence of the chromophore to the metal surface [Barnes, W. L., 1998 Knobloch, H et al., 1993]: The ones that are close to the metal surface are quenched and most of the excited state energy is dissipated as heat. For the chromophores lying at intermediate distances from the metal surface, some of their energies can be used in back couple to a surface plasmon mode. And as a last case, at sufficient separation distances (>20 nm), free emission of the dyes dominates. However, the fluorescence yield cannot be directly obtained unless two effects are considered. Firstly, the fluorescence emission oscillates as the distance increases, since the metal reflects the fluorescence field and introduces light interference. Secondly, the excitation source, i.e., the evanescent field weakens as the distance increases..

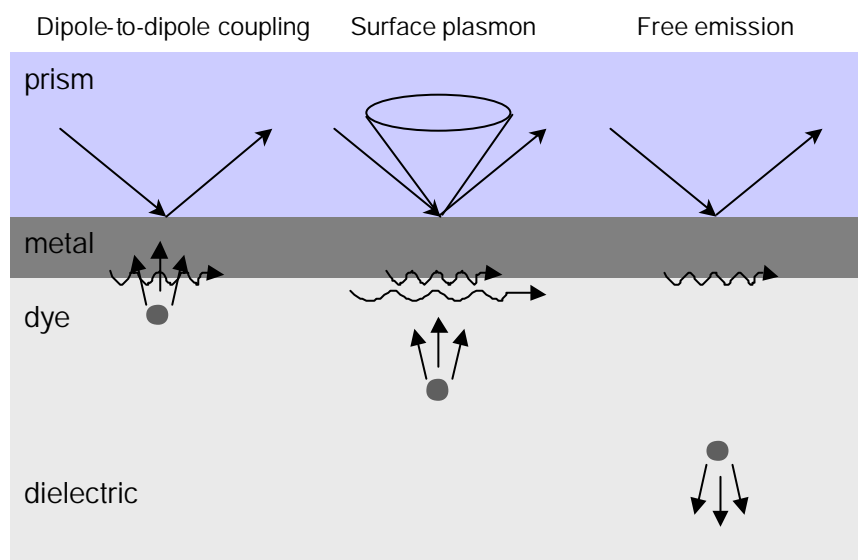


Figure 16: Schematic drawing of a fluorophore positioned close to a metal/dielectric interface. Different fluorescence decay channels take place at different fluorophore/metal separation distances

This distance dependence of fluorescence emission is described by the Förster equation;

$$\frac{I_d}{I_\infty} = \left[1 + \left(\frac{d_0}{d} \right)^4 \right]^{-1} \quad \text{eqn.14}$$

where I_∞ denotes the fluorescence intensity at infinite separation distance in the absence of a metal surface, I_d is the observed fluorescence intensity at a distance d from the surface, d_0 is the so called Förster radius that corresponds to the distance at which the fluorescence is decreased to the 50 % level. This radius ranges typically between 5 and 10 nm. Since the quenching effects can influence the quantitative description of various interactions, it is really important to carefully design the supramolecular architecture. This is the case in our working system, Streptavidin-biotin system, where the thickness of the architecture is around 7-8nm, which is in the quenching regime of the metal substrate.

In order to calculate a theoretical quenching profile for the present SPFS system, one has to consider the probability for fluorescence emission in a) all directions b) towards the photodiode on the backside of the prism and c) towards the gold surface, where coupling of the fluorescence light to surface plasmons is possible.

2.11 Surface Plasmon Microscopy (SPM)-Fluorescence Microscopy (SPFM)

SPM and SPFM are imaging detection methods based on evanescent field optics that allow for observation of oligonucleotide hybridization in real time. These methods offer both label and label-free detection modes, and as a result are useful when dealing with delicate molecules where a label might significantly alter the properties of any biomolecular interaction [Kambhampati D., 2004].

Surface plasmon microscopy, or SPM, has also been developed for spatially-resolved DNA sensing, which can directly meet the needs in reading DNA or biomolecule microarrays. This imaging technique is especially useful for the imaging of low-contrast samples. SPM allows for the imaging of such systems without any addition of fluorescent dyes, which is generally used to enhance discrimination (SPFM) [Rothenhäusler et al., 1988].

The same theoretical principles of SPR are also valid for the microscopy. That means any PSP spectrometer can be easily converted to a microscope by simply

adding a lens to the detection side and monitoring the obtained image on a screen or with the help of CCD camera as shown in Fig.17.

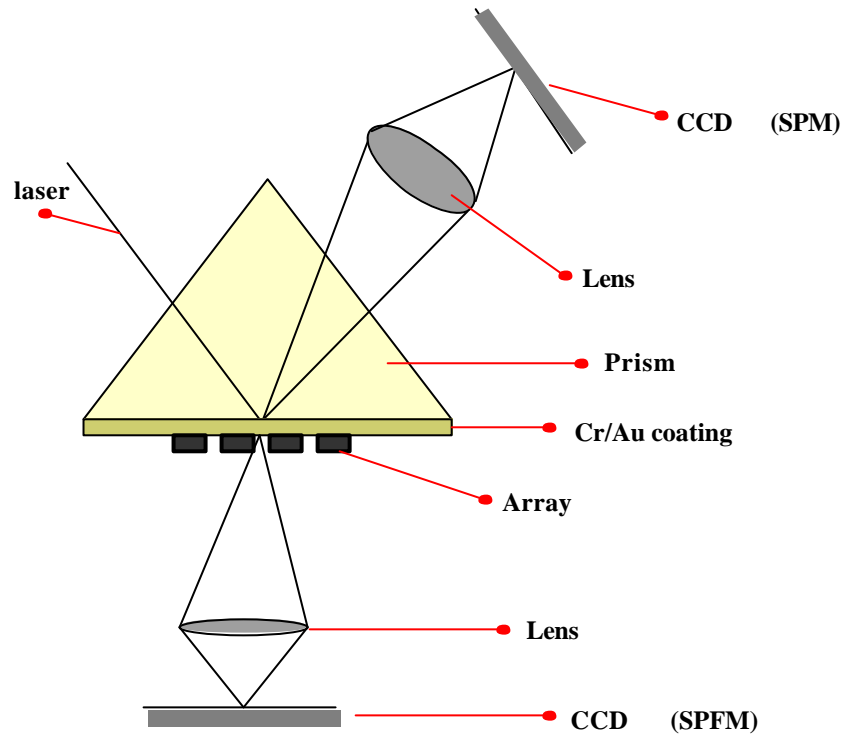


Figure 17: Schematic representation of SPM & SPFM set-up (from Rothenhäusler et al., 488, 1988, Nature).

The sensitivity issue is important in microscopy as is the lateral resolution. The lateral resolution in SPM is in the $1\mu\text{m}$ range. Even though we have to deal with resonance contrast in SPM, this technique gives higher sensitivity than the other microscopy techniques resolving 10nm thickness; since the detection scheme contains plane-wave optical components, SPM is limited by diffraction. As it was explained in previous sections, PSPs are propagating modes [Rather, 1988] which are strongly damped in their propagation direction due to intrinsic dissipation and radiative damping. A quantitative measure of how far a PSP mode travels is the propagation length L_x is directly related to the imaginary part of the complex PSP wavevector, k_{ix} , by $L_x=(2k_{ix})^{-1}$. If radiative damping can be neglected, L_x which is defined by the complex dielectric function of the metal. Hence, L_x is the wavelength-dependent higher spatial resolution in SPM, which is achieved with only lossy PSP modes.

In the case of SPFM, the resulting fluorescence emission is detected by a highly sensitive CCD camera in the microscopic mode [Zizlsperger et al 1998, Liebermann et al,2003] which can be used then to observe the oligonucleotide hybridization process.

In both SPM and SPFM measurements, the light is expanded with a 3D spatial filter as seen in Fig.18. The images are then collected from the side of the prism in SPM case and from the backside through a interference filter for SFPM.

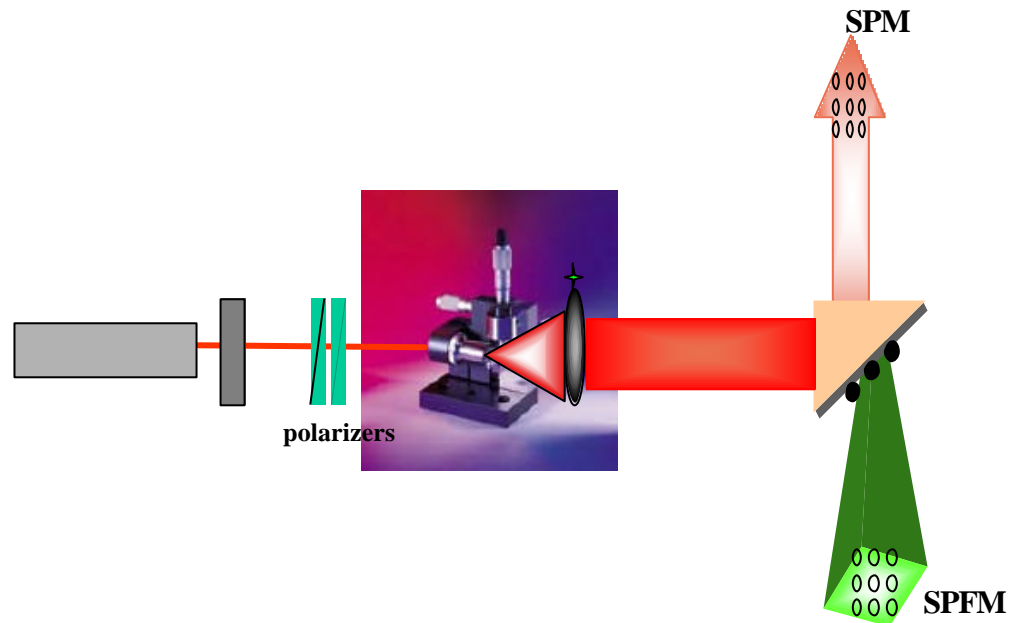


Figure 18: Schematic representation of SPM and SPFM techniques with a 3D spatial filter configuration

2.11.1 Image Analysis

The most important property of a camera for fluorescence microscopy is the sensitivity. The sensitivity of the camera is defined by the parameters such as quantum efficiency, dark current, read noise and the total noise. Even though the parameters are individually affecting the sensitivity, they are dependent on the cooling capability of the camera since the dark current value is strongly temperature dependent.

To measure the sensitivity of the camera, we need to calculate the total noise.

$$\text{Total Noise} = \sqrt{\text{read noise}^2 + \text{dark noise}^2} \quad \text{Eqn.15}$$

$$\text{Dark Noise} = \sqrt{(\text{dark current}) \times (\text{integration time})} \quad \text{Eqn.16}$$

Dark current is the charge that is thermally generated or in other word, it is the charge accumulated within a pixel, in the absence of light. Dark current describes the rate of generation of thermal electrons in a given CCD camera. High-performance CCD camera systems reduce the dark noise by cooling the CCD with either thermoelectric coolers (TECs), liquid nitrogen (LN₂) or cryogenics camera refrigeration during camera operation. For example dark current of a CooledSNAP CCD camera is 5 e⁻/p/s at normal operating temperature while that value is 0.05 e⁻/p/s at -30 °C. If these values are inserted in the equation to calculate the total noise for normal operating temperature system, the value of the dark noise is increased and then the total noise and as a result sensitivity decreases. For long exposure times, cooling becomes very important. Especially for the observation of the kinetic binding of DNA chains, a long term observation is needed to get reproducible association and dissociation data.

Quantum efficiency is the measure of the effectiveness by which an imager produces electronic charge from incident photons. Especially this is an important property to perform low-light-level imaging. A good cooled CCD has a quantum efficiency around 40-45%. Beside that, *the pixel size* defines the resolution. Resolution of a CCD is a measure of how fine a detail can be detected in terms of pixel.

When an image is quantified, the gray value is the main output to measure. *Average Gray* value is the average of the pixel grayscale values contained in the object.

Average Gray Value

$$\frac{\sum \text{Gray Value}}{\text{Number of Pixels}} \quad \text{Eqn.17}$$

Total Gray Value is the sum of the grayscale values for all pixels contained in the object. Also referred to as Integrated Gray Value.

$$\text{Total gray value} = \sum \text{Gray Values} \quad \text{Eqn.18}$$

Another function for the image analysis is the intensity profile of the image. Intensity Profile is a function in the image analysis program MetaMorph® which creates an image that represents a source image's intensity levels as heights in a "3-D" topographic display.

There are some other functions that are described below which have been used in the SPFM studies and are important in the image analysis. Those are;

- Subtracting background: subtracts the background intensity level from captured image.
- Measure Regions: measures and displays various intensity statistics of selected regions in a stack or a live video image in gray value.
- Integrated Intensity: the sum of all intensity values for all pixels in the region.
- Line scans: measure of the intensity level for the selected region. For the quantification of the array image, the line scan has an important role

3. MATERIALS AND METHODS

3.1 Instrumental

The experimental set up that has been used for the experiments is the Kretschmann-Raether configuration. The set up has been built during the first year of the work and modified for the microscopic purposes by replacing the detection elements with CCDs.

The schematic representation of the set-up is given in Fig.1 and pictures of the actual apparatus are given in fig.2. A Helium-Neon (HeNe) laser beam (Uniphase, 5mW, $\lambda= 632.8$ nm) passes through a chopper (frequency = 1331 MHz), which is connected to a lock-in amplifier (EG&G). Then the beam passes through 2 polarizers (Glan-Thompson), that can be used to tune intensity and polarization direction of the beam. Between sample holder and polarizers, a programmable shutter can be added to minimize the photo-bleaching in the spectroscopy mode. It allows the laser light to pass through during the open time and after data points are recorded during the time that given by a script, it is constantly blocked again.

Next, the beam is reflected off the base of the coupling prism (Schott, LASFN9, $n=1.85$) and is focused by a lens ($f = 50$ mm, Owis) onto a collection lens and a photo-diode detector, connected to the lock-in amplifier. The prism/sample and the photo-detector are mounted on two co-axial goniometers, respectively, enabling an independent tuning of the respective angular positions.

Surface plasmon microscopy (SPM) can be realized for monitoring laterally structured surfaces or for parallel read-out of arrayed samples. Two modifications of the set-up are necessary: a beam expander is assembled by an $10\times$ objective lens, a 25, 15 or $10\mu\text{m}$ pinhole and a collimating lens resulting in a clean, parallel and expanded beam for illuminating a larger surface area. The other modification replaces the photo-diode detector by a monochromatic CCD camera (Hamamatsu, C5405-01) equipped with an imaging lens (EHD, Zoom70 or Rodenstock $f=50$ mm). The CCD camera is connected to a frame-grabber card for image transmission and recording.

The fluorescence detection unit is mounted towards the base of the prism, rotating together with the prism (sample) at θ , while the photo-diode detecting the reflected light rotates at 2θ . The fluorescence emission from the sample surface is collected by

a lens ($f = 50$ mm, Owis) and passes through an interference filter ($\lambda = 670$ nm, $\Delta\lambda = 10$ nm, LOT, 80% transmittance) into a photomultiplier tube (PMT, Hamamatsu), which is connected to a photon-counter unit (Agilent) via a home-built electronic interface. Note that the interference filter is specifically designed for commercially available fluorophores such as Cy5 (Cyanine 5, from Amersham Pharmacia Inc.). Custom programs are used for data acquisition and for controlling the system electronics.

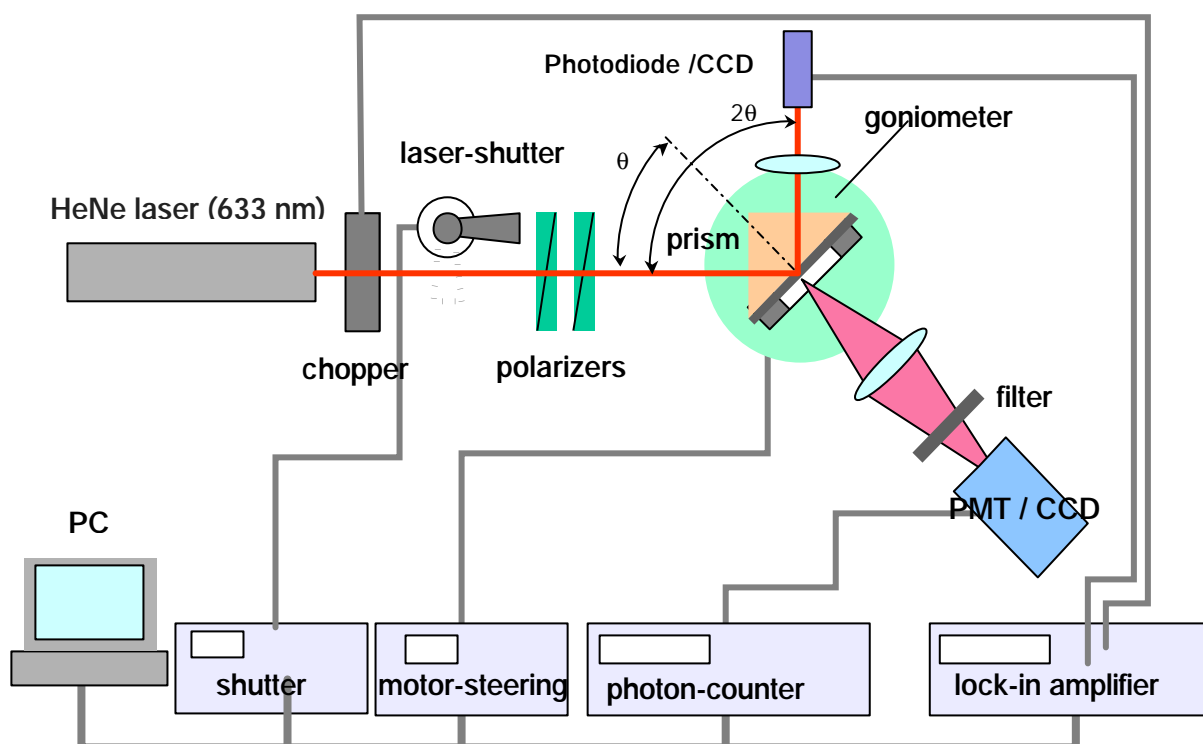


Figure 1: Schematic sketch of a surface plasmon spectrometer (SPR) set-up including various extensions. The whole set-up including the motors of the goniometer is remote controlled by a personal computer using the software WASPLAS.

Surface plasmon fluorescence microscopy (SPFM) is also feasible with this set-up by adding a cooled CCD camera (Roper scientific) with an imaging lens (Rodenstock $f = 50$ mm). However, for these two elements, the controlling and the data acquisition programmes are provided by the vendors. Therefore, these signals are only manually synchronized with the SPR reflectivity signal.

Two measurement modes, i.e. angular scanning mode (reflectivity/fluorescence/image as a function of angular position) and time-resolved kinetic mode

(reflectivity/fluorescence/image as a function of time) are both applicable for SPR (M) and SPFS (M) measurements.

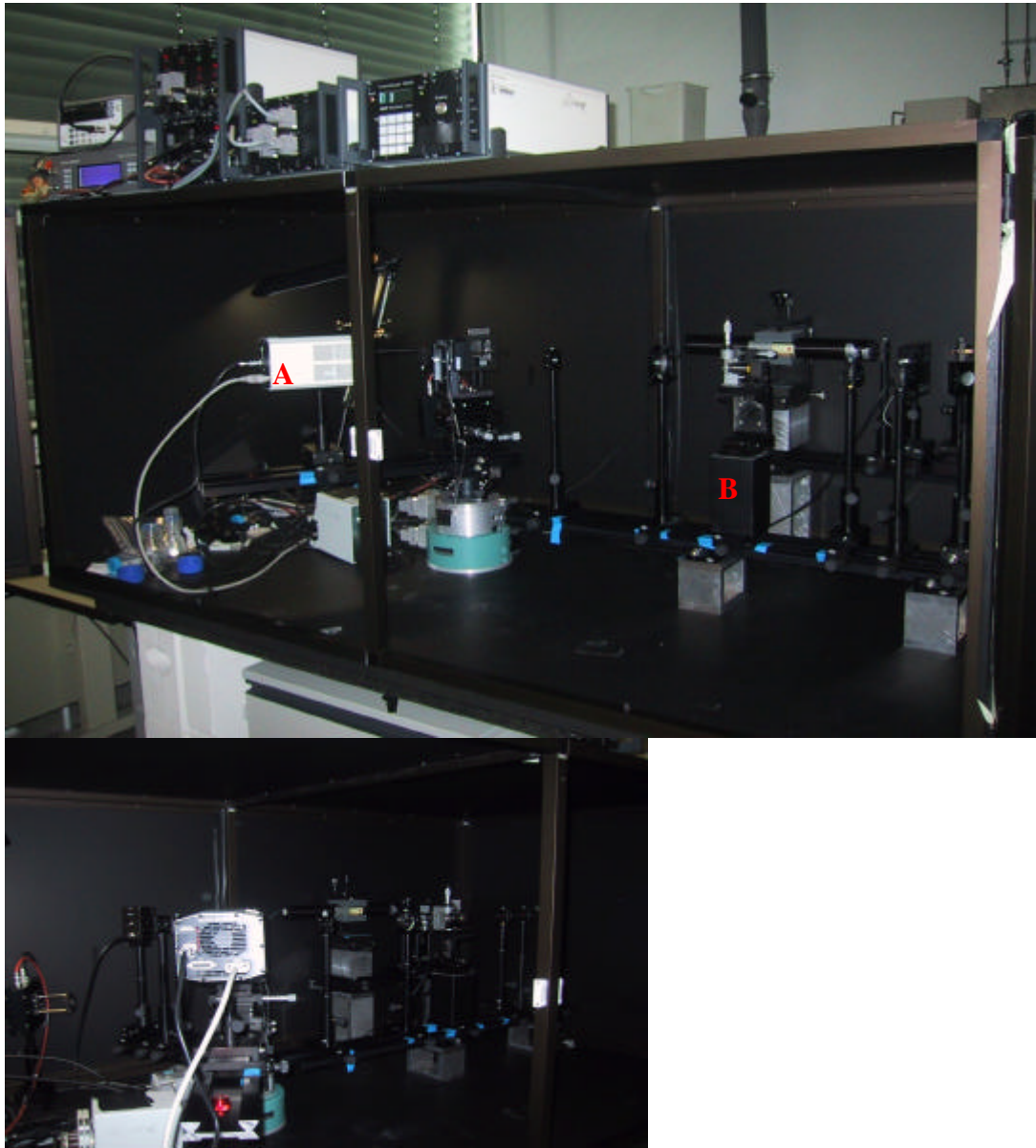


Figure 2: Actual picture of the SPR set-up with different modifications: A) CCD Camera, B) 3D beam expander

3.1.1 Experimental Surface Plasmon Microscopy (SPM) and Surface Plasmon Fluorescence Microscopy (SPFM) Set-up

Surface Plasmon Microscopy and Surface Plasmon Fluorescence Microscopy are currently available methods for monitoring real-time biomolecular interactions on metal-coated substrates. These techniques are based on a CCD modified version of the Surface Plasmons Fluorescence spectroscopy method.

As in the SPR, the sample is being illuminated with a TM polarised light in order to excite the surface plasmon at the interface between the metal and the dielectric medium. Instead of focusing the laser beam onto the sample, the diameter of the laser beam is expanded to about 1cm by using a spatial filter in order to illuminate the whole area as shown in Fig.3.

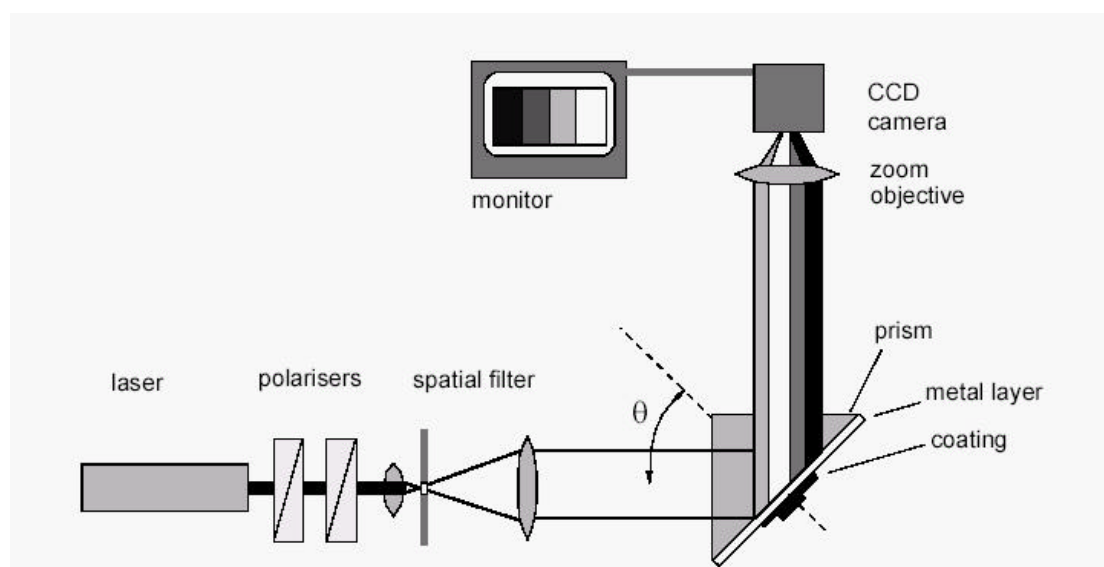


Figure 3: Experimental set-up of SPM (taken from the dissertation of Thomas Neumann)

3.2 Substrate and Metal Layer preparation

Commercially purchased high refractive index ($n=1.84489$ at 632.8nm , Melles Griot) glass slides, LaSFN9, have been used for the optical experiments. For each experiment, $1/3$ of one piece has been used after cutting the slide in 3 pieces, each 2.5×2.5 mm. The slides are cleaned in ultrasonic cycles during 15 min. each first, in 2% Helmanex® detergent (Helma, Germany) then in MiliQ and finally in ethanol.

Before the slides are loaded into a thermal evaporation machine (Edwards, FL400 with $\sim 2 \times 10^{-6}$ mbar UHV), they are dried under a stream of nitrogen and then placed directly into the evaporation apparatus.

For standard SPR measurements, 53.5nm gold (99.99%, Balzers, Germany) was deposited onto LaSFN₉ glass substrates but since the experiments were carried out by using a flow cell under saline buffer condition, additional ~ 1.5 nm chromium layer was evaporated first in order to increase the adhesion of the gold on the glass substrate.

3.2.1 Self Assembled Monolayers (SAM) on gold

Self-assembled monolayers are known as molecular assemblies that are formed spontaneously by immersion of a substrate into a solution of an active surfactant in an organic solvent [Ulman, 1991]. From the thermodynamic point of view, several processes are known to promote the self assembly process on the surface: for example one driving force could be physisorption. This process is not accompanied by a chemical reaction but relies, e.g., on electrostatic interactions between adsorbed molecules. A typical example is the alternating adsorption of polyelectrolyte layers of opposite charge. SAMs are often further stabilized by interactions between neighboring molecules in the film. Van der Waals interactions could be another example of physisorption. Another driving force is chemisorption, which is based on the high chemical affinity between the head group of the surfactant and the surface. These interactions are strongly attractive and lead to the formation of a thermodynamically favored covalent bond. As a result, molecules try to occupy every available binding site on the surface as shown in Fig4-c.

During the present work, a binary mixture of alkene-thiols, except in studies in chp.4.3.2, was routinely used to functionalize a gold surface. One of the molecules is terminated with a biotin group for the subsequent streptavidin binding to the surface architecture, while the other one which has a shorter chain length and is terminated with a hydroxyl group that acts as a spacer to dilute the biotinylated species in control of surface density. The chemical structures are shown in fig.4-a and b. The ratio of spacer thiol to biotinylated thiol has been set at 9:1 in order to create optimized space for the binding sites [Knoll, 2000]. The SAM was prepared ex-situ by immersion of a

gold slide in a 0.1 mM solution of thiols in EtOH overnight. After rinsing with EtOH, the slide was dried in a nitrogen stream and mounted into the flow cell.

The typical picture for the chemisorption of thiols on gold is that the thiol loses its hydrogen atom and becomes a thiolate covalently bound to the gold surface.

Two models for the reaction mechanism which only differ in the oxidant involved in the reaction, which is either protons or oxygen are suggested in the literature [Ulman, 1991]

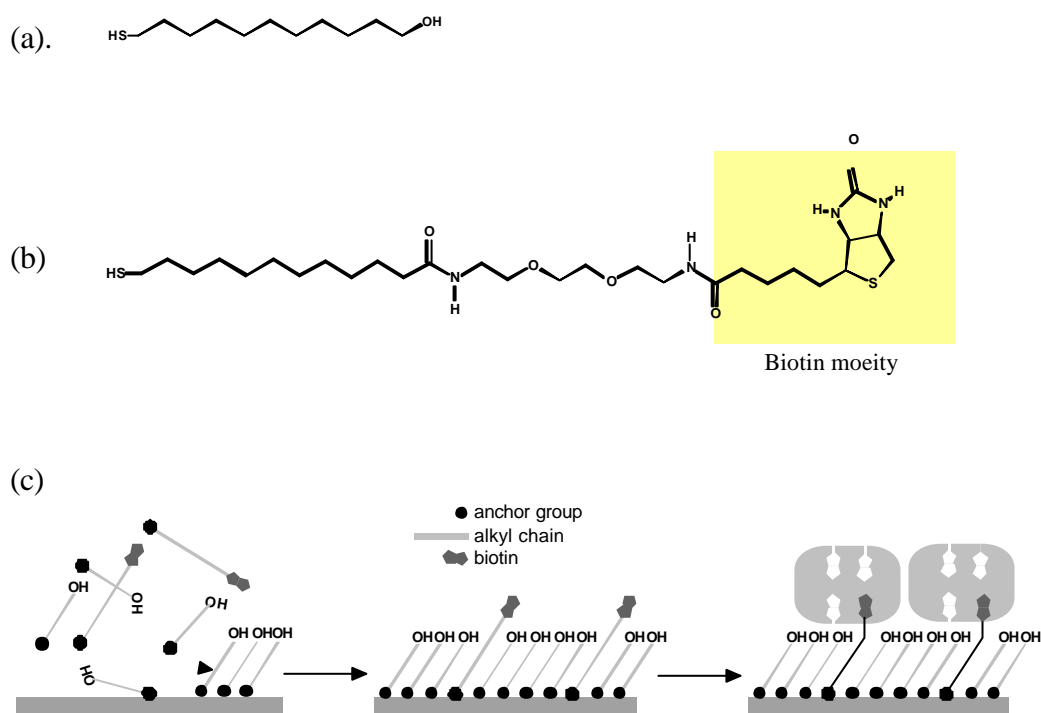
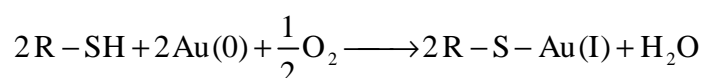
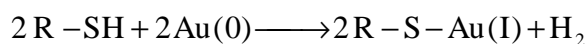


Figure 4: Chemical structure of **a)** 1-mercapto-undecanol and **b)** 11-mercapto-(8-biotinamido-4, 7, dioxaoctyl)-undecanoylamide, **(c)** Schematic of the self-assembly process. The anchor group, in this case S-H, has a strong chemical affinity to the gold surface. A covalent Au-S-bond is spontaneously formed by the mere exposure of the thiol solution to the gold surface. In the course of the reaction, all available binding sites on the gold surface are occupied by thiol molecules. The alkyl-chains adopt a parallel orientation with a uniform tilt angle of 30° relative to the surface normal. Such a highly ordered surface architecture meets perfectly the steric requirements for streptavidin binding (right cartoon).

Fig.5 shows schematically the formation of a mixed thiol SAM and its subsequent coverage with streptavidin molecules. The binding properties of a biotinylated SAM can be largely improved by spacer thiols of appropriate length and by a considerable dilution of the biotin binding sites. This is attributed to steric requirements of the binding reaction during which the biotin has to reach the binding pocket, which is relatively deep inside the protein. The OH-terminated thiol has two functions: first, it acts as lateral spacer optimizing biotin binding and second, it creates a chemical environment being resistant to unspecific adsorption of many biomolecules.

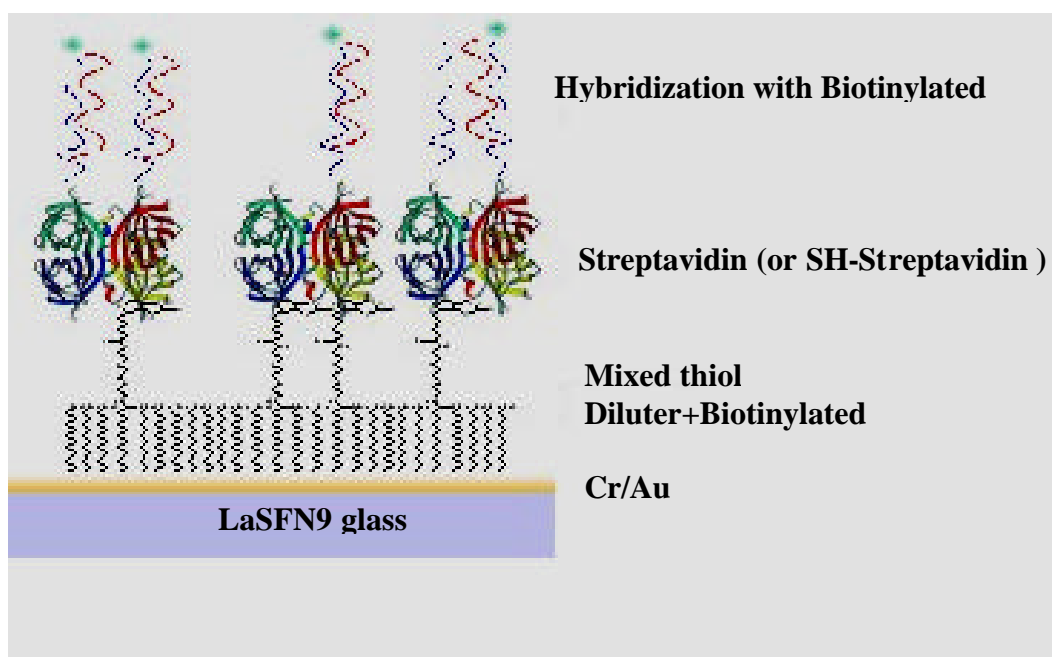


Figure 5: Schematic representation of a mixed monolayer of biotin- and EG (spacer)- thiol (with a molar ratio of 1:9 in the preparation solution) covered with streptavidin, probe and target.

3.2.2 Binding of Streptavidin and preparation of the flow cell

For the immobilization of oligonucleotide probes onto the surface, a very well defined binding matrix of streptavidin was used. Here, the strong binding between the streptavidin and biotin was utilized.

Streptavidin is a tetrameric protein (molecular weight 4×15 kDa), which was isolated from the actinobacterium *Streptomyces avidinii* (Fig.6). Each subunit is able to bind a molecule of biotin with an extraordinary high binding affinity and an exceptionally slow dissociation rate in solution ($K_d=10^{-15} \text{ M}^{-1}$) [Chilkoti, 1995, Weber, 1989].

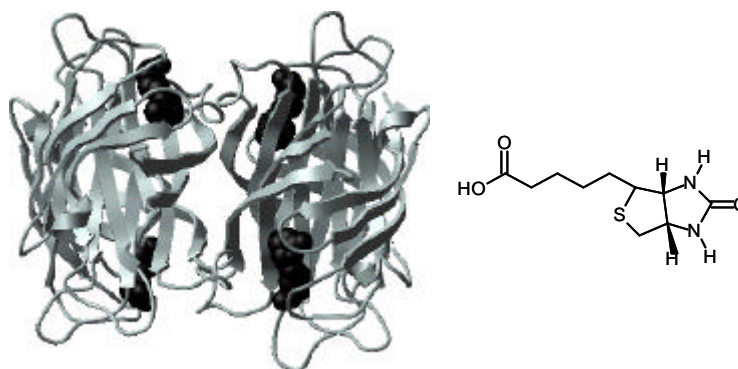


Figure 6: Molecular structure of a single streptavidin tetramer. Four biotin molecules (chemical structure on the right side) are depicted using a ball and stick model.

In the present work, a streptavidin layer that was anchored to the gold surface via biotin-modified thiols (SAM process), was used to couple biotin-modified oligonucleotides to the sensor surface. The deposition of streptavidin on the surface can be monitored by the SPR signal as a function of time, as seen in Fig.7. Circulation of the streptavidin solution proceeds until saturation is reached and no further increase in the real-time SPR signal is detected. After saturation is reached (typically after max. 45 minutes of flow circulation), the flow cell is rinsed with pure buffer for the displacement of remaining streptavidin solution.

As it has been explained in the theory section, the streptavidin binding causes an angular shift in the resonance curves and it can be also monitored as an increase in time of the reflectivity at a fixed angle at 30% reflectivity , as shown in the inset of Fig.7.

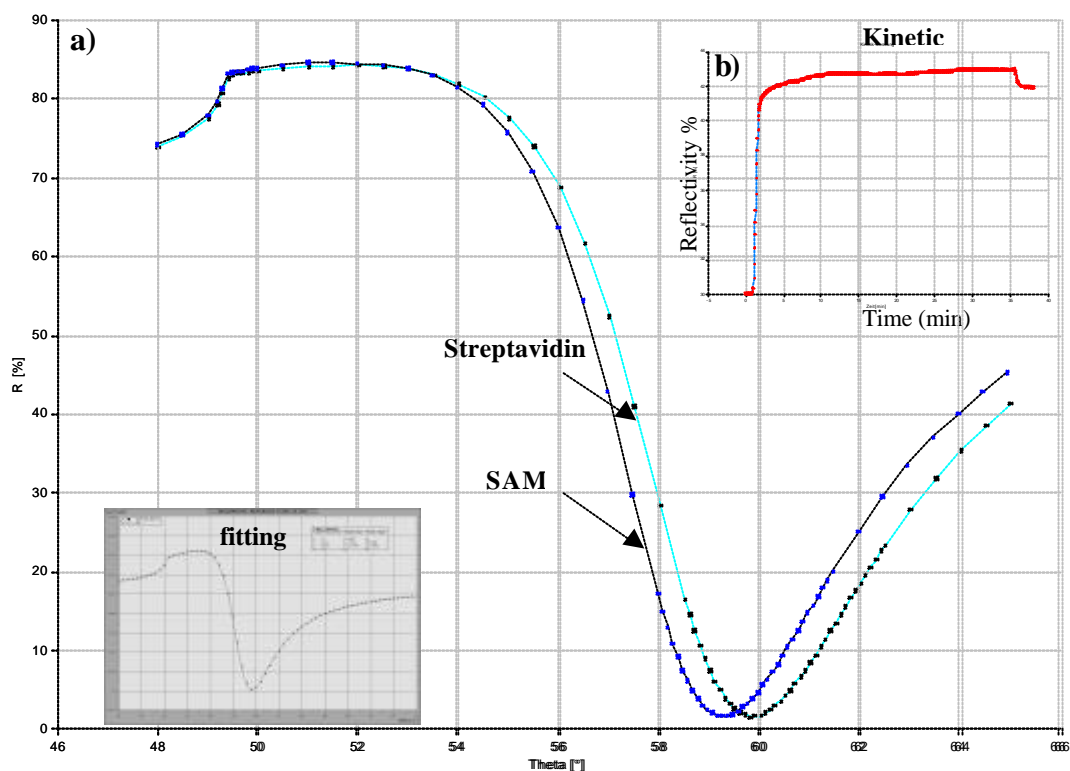


Figure 7: SPR detection of streptavidin binding. a) resonance angle shift after binding and b) kinetic observation of binding reaction in time

Providing a method for irreversible coupling, combined with its outstanding resistance against chemicals and temperature fluctuations, streptavidin immobilization became a widely spread method in bioanalytical applications such as the construction of biosensors and DNA microarrays [Wilchek, 1988]. The dimension of a single tetrameric streptavidin molecule was determined by X-ray crystallography to be $5.6 \text{ nm} \times 4.2 \text{ nm} \times 4.2 \text{ nm}$ (Fig.6) [Weber, 1989]. The thickness of the thiol-supported streptavidin layer measured by SPR is in good agreement with the height of a single streptavidin molecule. Within the scope of this work, the usefulness of the streptavidin monolayer as laterally diluted, highly reproducible platform for oligonucleotide immobilization will be demonstrated. The lateral dilution of the biotin binding sites guarantees a low coverage with oligonucleotides. This reduces fluorescence quenching between neighboring DNA chains and steric hindrance during DNA hybridization and replication reactions.

A home-made flow cell was used for the experiments. This flow cell is one of the first generation flow cells that has been used in the group. In following studies, a metal version of the flow cell has been developed but it hasn't been used in any of the

studies in this thesis due to the corrosive effect of NaOH used for regeneration purposes.

Side and top views of the flow cell are shown in Fig.8. The cell is constructed from a quartz plate (Herasil, Schott) with an inlet and an outlet (diameter=1 mm) at the indicated positions. The circular inner part of the cell has a radius of 3 mm and a height of 2 mm confining the volume to ~60 μl . In order to be able to image the whole array, the same design of the flow cell with a larger diameter (~2.5mm) was used. The flow cell is sandwiched between a quartz plate (Herasil, Schott) and a glass wafer which is evaporation-coated with a thin gold film as described above. The gold covered surface points towards the cell. The contact areas between these components are sealed by Viton O-rings. A high refractive index prism (LaSFN9; $n=1.845$) is mounted on top of the glass wafer. In order to improve the coupling between the incident light and the SP modes, the glass wafer and prism are connected via a thin film of refractive index-matching oil ($n=1.7$). The use of matching oil with a refractive index lower than that of the prism is justified by the high vapour pressure of oils exhibiting higher refractive indices. A metal sample holder keeps the sample in place on the goniometer during the measurement. All measurements were performed employing a constant flow rate of 2.5 ml/ min unless otherwise specified.

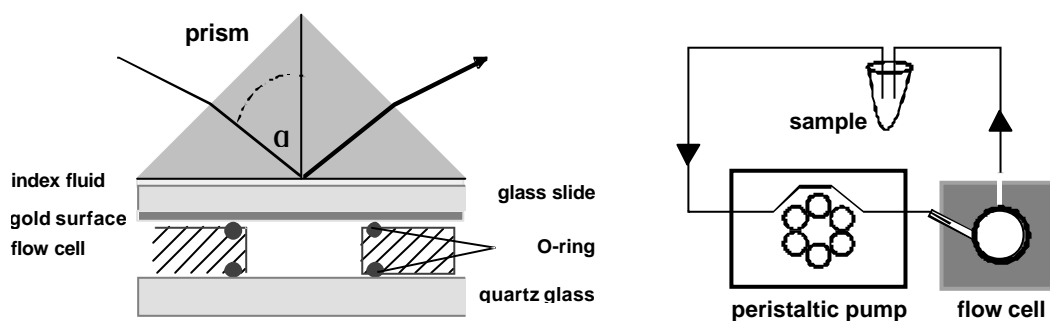


Figure 8: Construction of the measurement chamber (left) and top view of the flow cell including a schematic of the circulation loop (right).

The flow cell is connected to a peristaltic pump (NovoChem) and the sample reservoir using Tygon® tubes with an inner diameter of 0.76 mm. Thus a closed circulation loop is formed which is disconnected during the injection phase. The total volume of the loop for a 1mm diameter flow cell is around 300-400 μl , while the larger one is around 700-800 μL . Therefore injection volumes between 1-1.5 ml for

high concentrations and 5 ml for low ones have been used to ensure a constant value of the desired analyte working concentration.

Experimental buffer solutions were changed depending on the probe-target pair. In the case of PNA –DNA hybridization, 10mM phosphate buffer which have 100mM high salt concentration and 0.1mM EDTA @ pH 7.1-7.2 was used. For DNA-DNA hybridization, 10mM phosphate buffer, 2.7 mM KCl, 150 mM NaCl, pH 7.4 was used. It's imperative that any stagnant air bubbles forming on the edge and even sometimes in the flow cell are removed by lowering the vapor pressure inside the flow cell, during which the bubbles will expand, followed by sudden equilibration to the atmospheric pressure, at which the expanded bubbles will collapse or be ejected from the flow cell edges by the sudden pressure increase. Furthermore, this process can be performed during the course of an experiment without inducing any changes in surface properties or signal intensity.

3.2.3 Immobilization of the Catcher Probe onto the Substrate Surface

Biotin-coupled catcher probes, either PNA or DNA, are dissolved in an appropriate solvent which was mainly MiliQ water for PNAs and buffer for DNAs.

The DNAs are dissolved in PBS buffer (phosphate buffer saline, Sigma, 157mM NaCl) and diluted to a concentration of 1 μ M before being introduced into the flow cell. The deposition of the catcher probes can be monitored in real-time by following the increase in the SPR signal as in the case of streptavidin. However, the angular shift in resonance angle cannot be observed as clearly as in the streptavidin case as shown in Fig.9, since the catcher probes are not as big as the streptavidin molecule. This is one of the reasons that labeling is needed to be introduced to the SPR technique. The deposition of catcher probes is similar to that of streptavidin binding, and deposition can be stopped when saturation is reached, as indicated by the leveling off of the SPR response.

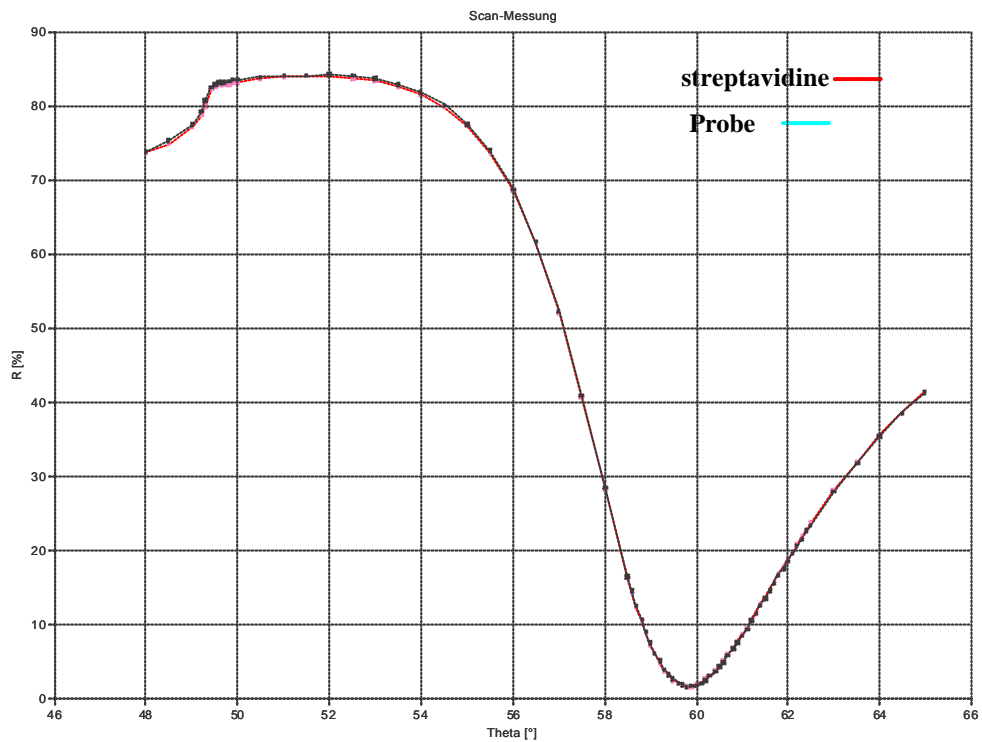


Figure 9: Angular Scan measurement after probe immobilization

3.2.4 Hybridization reaction and Fluorescence Measurement

Before target injection, an angular scan measurement with photon counter is carried out to record the background fluorescence. A typical scan measurement is shown in the Fig.10 below.

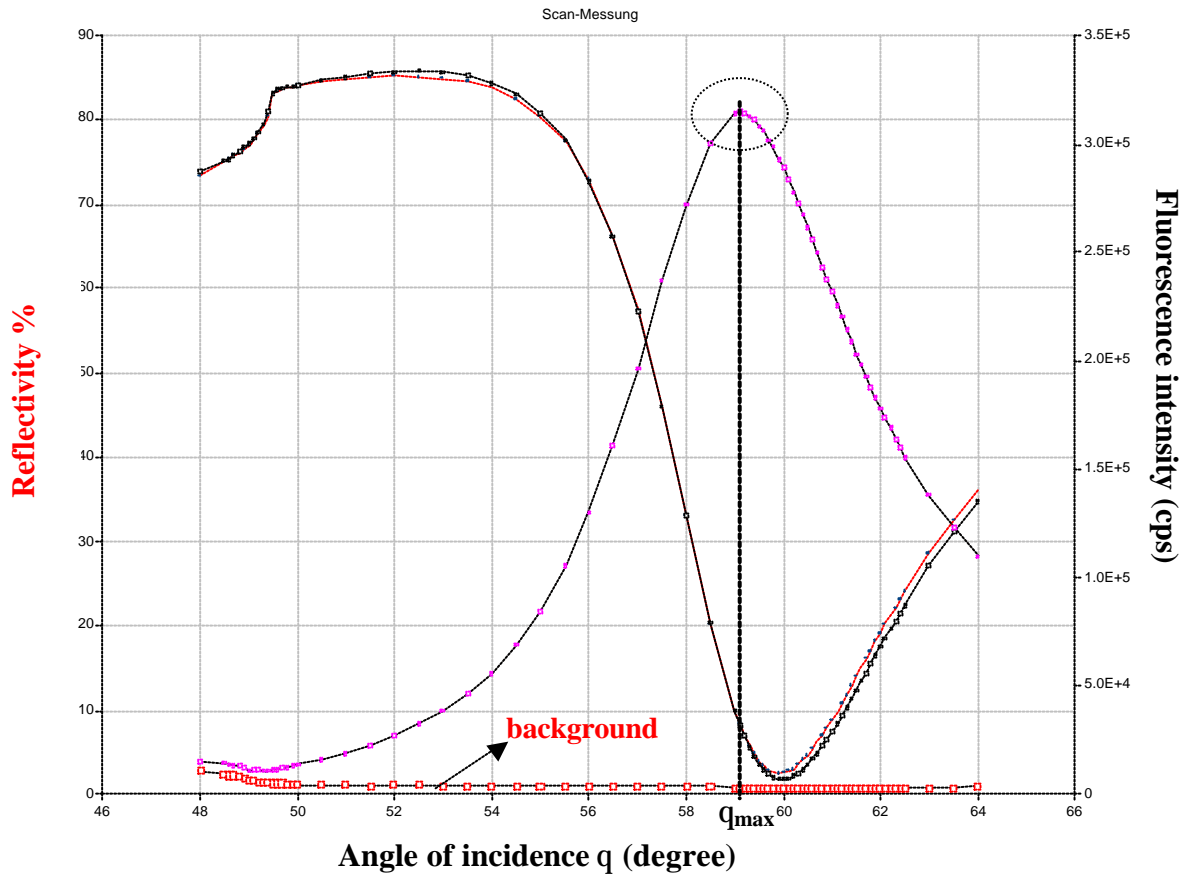


Figure 10: A typical SPR scan curve with the fluorescence (SPFS)

The fluorescence process was measured by increasing the angle of incidence $\theta_{\text{incidence}}$ from 48 to 65° stepwise with $\Delta\theta_{\text{incidence}} = 0.1-0.5^\circ$. The angle of incidence corresponding to the maximum fluorescence excitation (at θ_{max}) can be easily determined after the scan measurement and will be used as the fixed angle for kinetic measurement for fluorescence. The experiments start by rinsing with buffer and then recording a scan curve, which serves as the baseline of the experiment. In the single kinetic experiment generally a 2ml volume of 100nM Cy5 dye labeled 11mer DNA target solution was used. The first 500 μ l of the target solution was introduced into the liquid handling system to replace the buffer solution from the flow cell and the remaining 1.5ml were allowed to circulate within a closed loop during the experiment. The measurement proceeds with a constant collection of the fluorescence intensity data points with the help of a script, through which the shutter controller's parameters could be defined by the user. Usually the shutter was kept 3sec open in every data point recorded in 5 min, to avoid bleaching of the chromophores.

The rise of the fluorescence intensity slows down as the surface coverage increases and eventually levels off as the surface becomes saturated. After the fluorescence intensity is stabilized, the rinsing with the buffer solution takes place. At the beginning the loop is usually kept open to displace all the excess target from the flow cell.

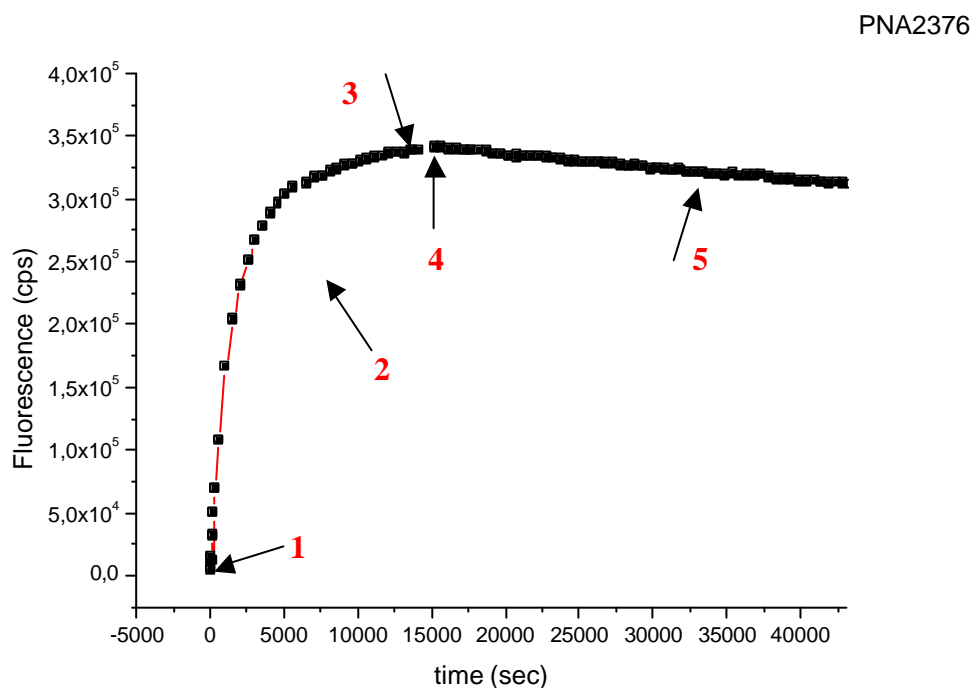


Figure 11: Single kinetic measurement with fluorescence. 1) Injection of target solution; 2) hybridization, association phase; 3) saturation of fluorescence signal; 4) start of rinsing; 5) disassociation phase with continued rinsing

The experimental data, an example is shown in Fig.11, is then simulated according to the Langmuir model and numerical values for k_{on} for the association constant (for the hybridization phase) and k_{off} for the dissociation process (from rinsing) are obtained after fitting. Thus, the binding affinity constant, K_a , which is k_{on}/k_{off} can be obtained.

Beside the PCR products, all targets that have been used in the experiments were commercially available from MWG GmbH, Germany. DNA sequences were designed in a way that natural, anti-parallel head to tail, (3' to 5') orientation relative to the surface immobilized probe could be achieved upon hybridization. All targets had a Cy5 label (Fig.12) on their 5' tail, while the probes had a biotin on the 5' end.

Depending on the purpose of the experiment, the target was designed to have either full complementary base sequence to the probe (MM0, MisMatch0), a single base-pair mismatched duplex (MM1) or a double base-pair mismatch duplex (MM2)

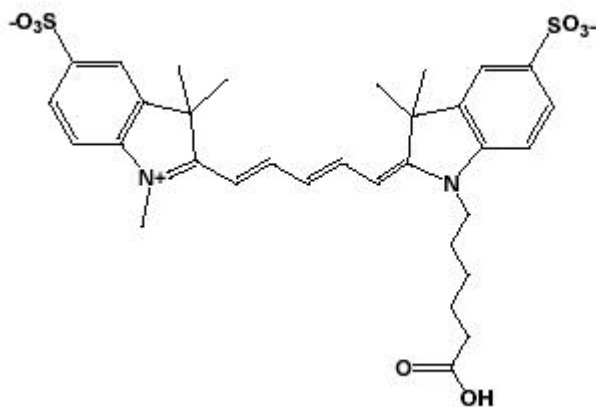


Figure 12: Chemical structure of Cy5 chromophore, which has its maximum absorbance at $\lambda=649\text{nm}$ and emission at $\lambda=670\text{nm}$.

Due to the fact that all fluorescence measurements require highly sensitive signal collection, some experimental considerations have to be kept in mind during the experiment. Since a very small amount of stray light affects the fluorescence background, the experimental set up is built in a black-box and the corners were sealed with a black tape. Another consideration is the loss of the fluorescence signal via quenching and bleaching. Self-bleaching occurs if the overall density of the chromophores is too high. That process results in either re-absorbance or dissipation of the fluorescence emission by neighbouring chromophores. This can be avoided either by keeping the target concentration low or by reducing the density of binding sites to ensure the separation between targets in solution and surface bound chromophores. Photo-bleaching occurs when fluorescence emission is diminished due to prolonged exposure to high energy excitations when the chromophore is chemically or physically degraded. Photo-bleaching is a big problem especially in the fluorescence microscopy experiments since the acquisition time is at least 20-25 sec., depending on the sensitivity of the CCD. Therefore either in the spectroscopy or in the microscopy experiment, the laser light is blocked with the help of a shutter. Since the titration experiments are longer than single kinetic experiments, the shutter control becomes more crucial. That is why the closing time between two data points in that

kind of experiments is longer than that in a single kinetic experiment. Such strong caution is needed not only because of the longer duration of the experiment, but also in order to avoid self-bleaching of the chromophores due to the increase of the surface-bound chromophore concentration in time.

A titration experiment is another method based on the Langmuir isotherm and used for defining the binding properties of the oligonucleotides. In this case, the surface is being “decorated” by the target molecule starting from lower concentrations. The surface probe architecture is allowed to be saturated by stepwise increase of the target concentration according to the Langmuir isotherm. This condition has been obtained by injection of the target solution with a specific concentration and by allowing uninterrupted hybridization until the fluorescence signal reaches saturation. After saturation, the target solution is replaced by the washing buffer and an angular fluorescence scan is recorded. After the motor position is again tuned to the 30% reflectivity angle, the second higher concentration is injected and the steps described above repeated. This procedure is repeated until the fluorescence response no longer shows a significant increase with increasing target concentration. The range of the concentrations to be performed highly depends on the specific binding affinity between surface the probe and the target. A titration experiment takes quite a long time. Especially the first concentrations take a long time since the target binding process at extreme low concentration is limited by mass transportation. The possibility of material loss due to unspecific adsorption anywhere in the flow cell during the circulation needs to be taken account at those extreme low concentrations, e.g., pM as it is seen in Fig.13-a.

After the experimental data set is obtained, the fluorescence saturation values are plotted against corresponding target concentration and the resulting plot is fitted to a Langmuir isotherm (fig.13-b) in order to obtain the dissociation constant, K_d , which is the reciprocal of the overall affinity constant K_a .

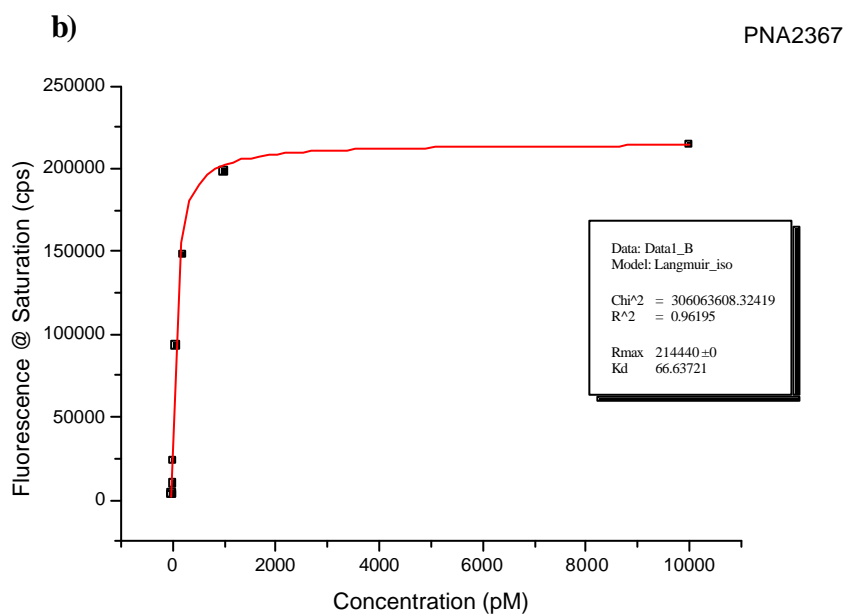
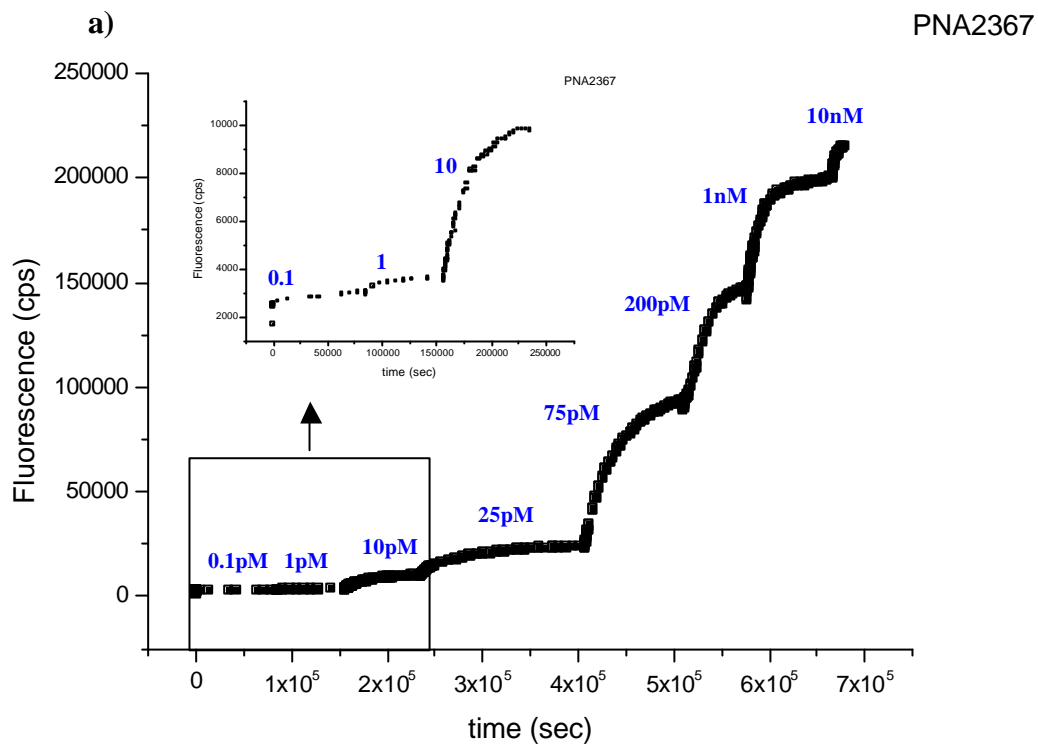


Figure 13: a) A typical titration experiment with a concentration range from pM to nM and b) obtaining the binding constant from Langmuir Isotherm fitting.

3.2.5 Surface Regeneration

The surface can be regenerated after hybridization by using 10mM NaOH. The solution is passed through the flow cell by using pulse flow for a few minutes in order not to rip off the probe from the surface. Then the surface is washed with a fresh buffer for half an hour with an open loop. Using this procedure, the same probe surface can be used several times. The regeneration process can be monitored by following the fluorescence signal drop after the NaOH treatment as seen in Fig.14. The background fluorescence level can never be achieved as low as it was before any regeneration. However, there are always some fluorescence targets left on the surface even though their level is quite small.

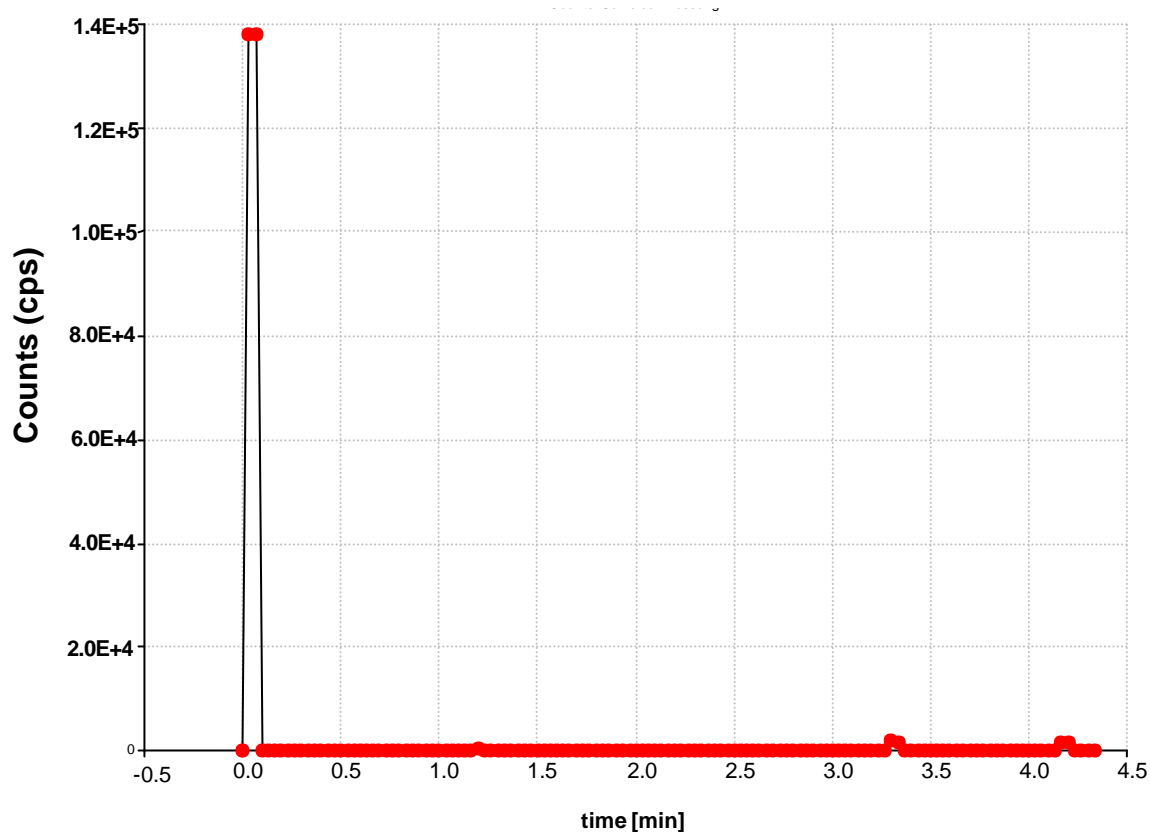


Figure 14: Monitoring of the fluorescence vs. time during the regeneration process with 10mM NaOH.

3.3 Surface-Plasmon Fluorescence Microscopy – A Novel Platform for Array Technology

3.3.1 Microarray preparation

Sample preparation steps involved basic glass slide cleaning, gold/chromium evaporation, thiol/biothiol surface functionilization and then streptavidin and biotinylated probe immobilization except for the SH-Streptavidin matrix. In later case, instead of the thiol/biothiol step, thiolated streptavidin (SH-terminated Streptavidin, Boehringer, Ingelheim, Germany) was used directly to the Au surface. The number of the steps can be reduced using this approach but the fluorescent labeled target would be brought closer to the metal surface and that will cause enhanced quenching by the metal.

3.3.1.1 Array Fabrication

Cr/Au coated LaSFN9 glass slides were immersed into a OH-thiol/biotin-thiol solution overnight, then washed with EtOH and incubated with 1 μ M Streptavidin for more than an hour. Excess of streptavidin was washed away by MilliQ water and then the samples were used immediately for spotting. A 1 μ M probe concentration has been used for all arrays.

In the case of SH-Streptavidin, the freshly evaporated slide was incubated directly in a 1 μ M SH-Streptavidin solution. It should be noted that, unless it's not mentioned, all the samples that were used in the experiments were prepared using the thiol mixture/streptavidin/probe layer sequence.

The arrays have been prepared by using either an ink-jet piezo nanoplotter (cf. Fig.4 in section 2.6.1), or a Pin-tool spotter (cf. Fig.5 in section 2.6.1) at room temperature and 70% relative humidity conditions.

All arrays have been prepared by using PNA probes of different lengths and mismatch carrying sequences in respect to the same target (MM0, MM1, MM2) given in Table1 in section 4.3.

3.3.1.2 Array Characterization

SPM images were taken in air in order to determine the resonance angle from the image contrast. In solution, however, the array usually was not detectable without hybridization with the dye-labeled target due to low contrast.

3.3.2 Hybridization between PNA-probe and oligonucleotides-target

The sensor surface was functionalized by probe-PNAs of known sequences and was exposed to an aqueous solution of the target-DNAs modified with Cy5 chromophore. A target can bind with a specific region to the probe sequence. The length of the sequence will influence the specificity and sensitivity of the binding. The rate constants and the affinity constants of the hybridization were measured for different lengths of the sequence for both, MM0 and MM1 target-DNA, respectively hybridizing to the probe-PNA strand in 10mM PB (10mM phosphate, 0.1 mM EDTA, and 0.005 % Tween 20) buffer solution at room temperature.

The fluorescence increase was measured as a function of time after the target molecules were injected until equilibrium was reached. After hybridization, a rinsing process was performed by changing the fresh buffer solution continuously. Each association and dissociation kinetics of hybridization was monitored by SPFM.

RESULTS

4. PNA-DNA Hybridization Observed in Real-Time

4.1 Surface Plasmon Field-Enhanced Fluorescence Spectroscopy (SPFS) studies of PNA-DNA interaction on two-dimensional (planar) surfaces

In this chapter, we describe the PNA-DNA interaction quantified by the SPFS technique. Different methods have been applied to describe the kinetic behaviour of the duplex formation. Affinity constants of the each PNA were obtained from single kinetic, titration and global analysis measurements and compared with their melting temperature values determined in bulk solutions.

4.1.1 SPFS

Surface plasmon field-enhanced fluorescence spectroscopy (SPFS) uses the enhanced electromagnetic field of a surface plasmon mode to excite surface confined fluorophores. In our case, the evanescent field of a surface plasmon at the gold/water interface is enhanced by a factor of 16 compared to incident field at the respective resonance angle. It decays exponentially into the dielectric medium with a penetration length of approximately 150 nm. Molecules in this evanescent layer alter the optical properties of the interface and can be sensed by monitoring the changes in SPR resonance minimum position. In the case of a molecule, carrying a fluorophore, fluorescence emission will be excited by the plasmon field.

SPFS gives access to local refractive index change and the fluorophore concentration simultaneously, it is thus a combinative technique, which gives more precise information than the label-free technique SPR alone.

However, one has to take into account some limitations. In the SPFS measurement, the fluorescence yield of a fluorophores near a metal exhibits highly pronounced distance-dependent behaviour, as it was mentioned before in the theory section [Barnes, 1998]. If we look at the Fig.1, for separation distances, 20-30 nm, the fluorescence of the fluorophore might be quenched or can be back-coupled as red-shifted re-radiation. For the distances smaller than 20nm, the chromophore gives its energy back to the metal layer as heat.

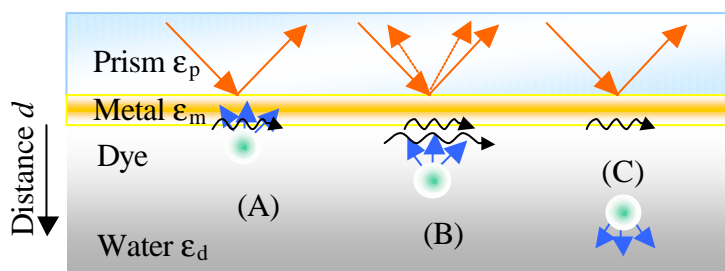


Figure 1: Decay channels for fluorescence emitted near a metallic surface A) non-radiative energy transfer, B) coupling of irradiated fluorescence light to SP modes, C) free emission of fluorescence.

Hence the effective fluorescence emission will be reduced. On the other hand, if the distance between the metal layer and the fluorophore is increased further, the fluorescence yield becomes weaker due to the fading evanescent field. This distance dependent phenomena, however, might help to understand the conformation of the surface bound molecules.

4.1.2 Experimental

4.1.2.1 Fluorescence monitoring

All the hybridization reactions were performed using Cy5 labeled targets which were diluted by working buffer.

The fluorescence light emitted from dye-labeled probes was either monitored in the scan or in the kinetic mode as described for the SPR spectra, with a PMT on the backside of the flow cell switched on. If the use of fluorescent probes was limited to surface reactions that were attributed to very low mass changes, the resonance angle for SP excitation remained unchanged. As depicted in the SPFS scan spectrum before, the fluorescence increased from the background value to a value determined by the dye concentration. Thus, if the resonance curve of the SPs does not shift, a linear relation between dye concentration and fluorescence intensity exists. The quantification of the fluorescence signal in the kinetic mode is more complicated in cases for which the resonance angle changes simultaneously with the surface concentration of dye. Then, the intensity of the evanescent field of the SP changes for a fixed angle of incidence and hence, the intensity of the excitation field. In this case,

deviations from the linear relation between concentration and fluorescence intensity are expected. For the reactions presented in this thesis, those deviations play a minor role since the observed mass changes were small.

The flow rate for the measurements was 2.5ml/min beside the experiments where flow rate affect was investigated. In those experiments, the flow rate was 3.6ml/min.

4.1.3 Materials

In the following experiments, we used materials in Table 1 obtained from the group of Prof. Peter E. Nielsen (Inst. for Medicine and Biochemistry Copenhagen). They aimed at modifying the backbone of PNA in order to increase the stability of PNA-DNA duplex and improve the cell uptake of those PNAs. In this context, they modified nucleobases containing aromatic moieties as a mean of increasing the stacking energy [Nielsen, 1991]. They measured the melting temperature of each PNA in solution and concluded that the stability of the hybridized complex increased.

The following modifications have been made:

The “D” modification indicates a 2,6-diaminopurine given in the structural formula in Fig.2.

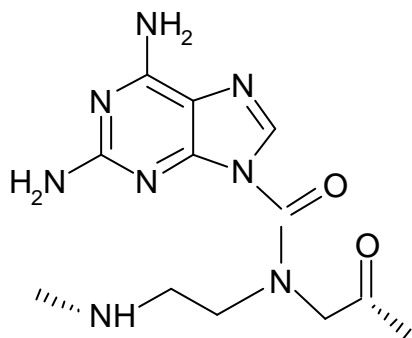


Figure 2: Structural formula of 2,6-diaminopurine represented as “D” ($C_{11}H_{14}N_8O_2$).

Another modification that has been synthesized was on the natural Thymine base. It refers to 7-chloro-1,8-naphthyridine-2(1H)-one, b1T modification (Fig.3-A) which has been designed so as to mimic the function of thymine in duplex and triplex recognition systems by specific interaction with adenine [Nielsen, 1991]. The natural A-

T base pair hybridization is shown in Fig.3-B. in both case, A-T and modified T-A (Fig.4-A) have a specific recognition to adenine (Fig3-C).

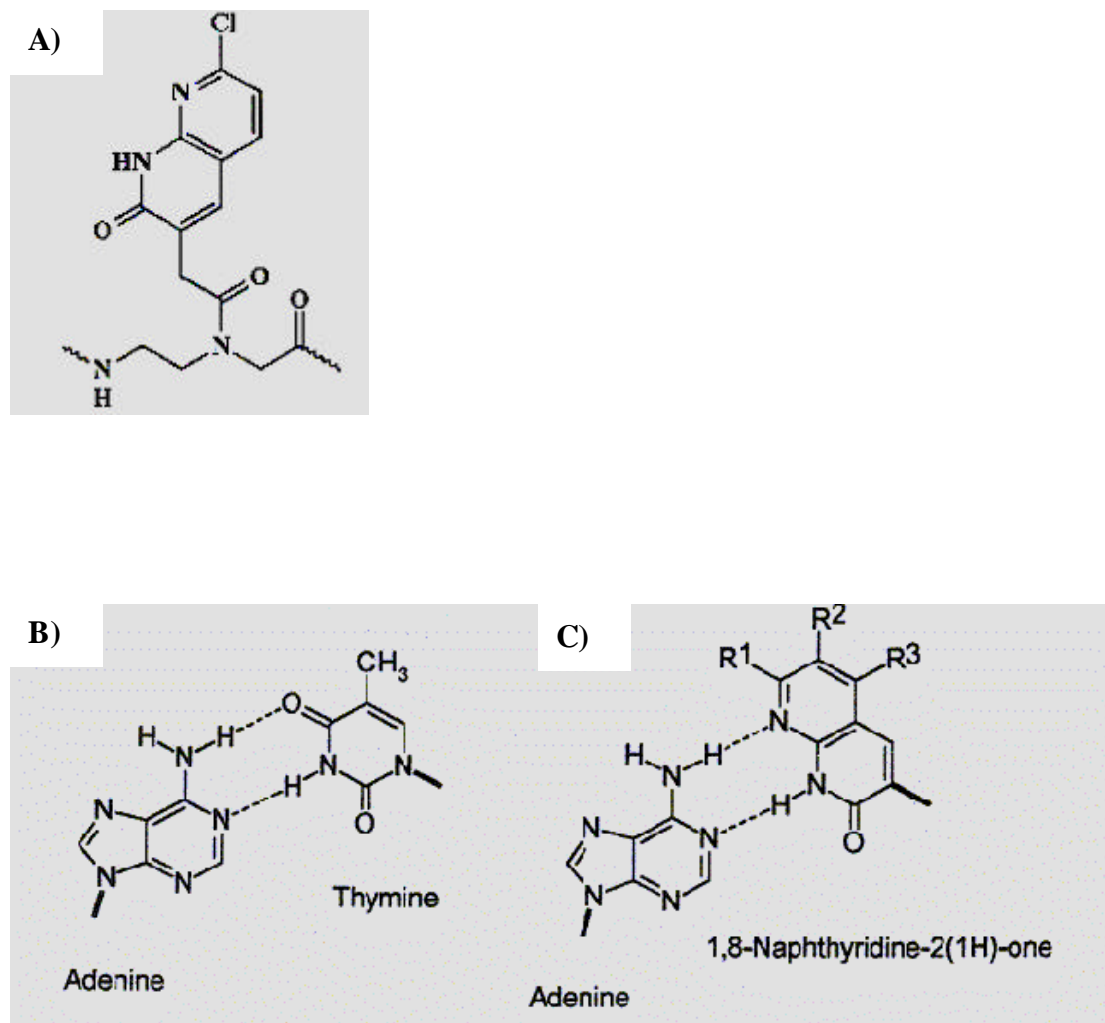


Figure 3: A) Mimic of the neutral thymine nucleobase, 7-chloro-1,8-naphthyridine-2(1H)-one; The Watson-Crick base pair interaction B) between natural Adenine-Thymine, C) Adenine-Modified Thymine bases

Table 1: PNAs that were obtained from the Copenhagen group and the targets, which were commercially supplied from MWG, Germany.

Strands	Sequence	T_m (°C) ^a	DT_m (°C) ^b	DT_m/mod (°C) ^b
PNA2361	5'-Biotin-(eg1) ₂ -AGA GTC AGC TT-Lys-NH ₂	67.1	–	–
PNA 2364	5'-Biotin-(eg1) ₂ - D GA GTC AGC TT-Lys-NH ₂	68.3	1.2	1.2
PNA 2367	5'-Biotin-(eg1) ₂ - DGD GTC AGC TT-Lys-NH ₂	73.4	6.3	3.2
PNA 2370	5'-Biotin-(eg1) ₂ - DGD GTC DGC TT-Lys-NH ₂	77.1	10.0	3.3
PNA 2373	5'-Biotin-(eg1) ₂ -AGA G(b1T)C AGC TT-Lys-NH ₂	69.2	2.1	2.1
PNA 2376	5'-Biotin-(eg1) ₂ -AGA G(b1T)C AGC (b1T)T-Lys-NH ₂	70.2	3.1	1.1
PNA 2379	5'-Biotin-(eg1) ₂ -AGA G(b1T)C AGC (b1T)(b1T)-Lys-NH ₂	71.2	4.1	1.4
Target	Cy5-AAG CTG ACT CT-3'			
SL15mer unspecific target	Cy5- CTAGTTCAGCAGCGA -3'			

a. Duplex concentration is 5.0 μM in strands.

b. The '+' sign indicates an increase in the value with respect to the unmodified duplex.

eg1: Ethylene Glycol spacer

One of the parameters that indicates the stability of the PNA-DNA duplex is the melting temperature (T_m) of the PNAs. As it was found by Prof. Peter E. Nielsen's group [Nielsen et al., 2002] that the modification has shown an increase of the melting temperatures corresponding to an increased of stability compared to the unmodified PNA2361. The melting temperature and the temperature increase per modification are in between 1.2 to 10 and 1.1 to 3.3 °C respectively.

Another parameter to describe the stability is the affinity constant (K_a). In the following experiments K_a has been obtained using 3 independent measurements; single kinetic measurement, titration measurement and global analysis measurements. All experiments were performed in 10mM phosphate buffer containing 100mM NaCl

at pH 7.1-7.2. Single kinetic measurements were performed using 100nM target unless otherwise mentioned.

The target used for the measurements has a Cy5 dye label, which is a negatively charged molecule. On the other hand, Lysine which was inserted into the backbone in order to increase the solubility of the PNA [Nielsen et al., 1991], is positively charged. Therefore, first the effect of unspecific interaction between Lysine and the Cy5 dye was investigated. A non-complementary 15mer target was injected and the fluorescence signal monitored as it is shown in Fig.4. The intensity increases, however, upon rinsing, the fluorescence dropped back to the background level. That indicates that there is almost no unspecific binding.

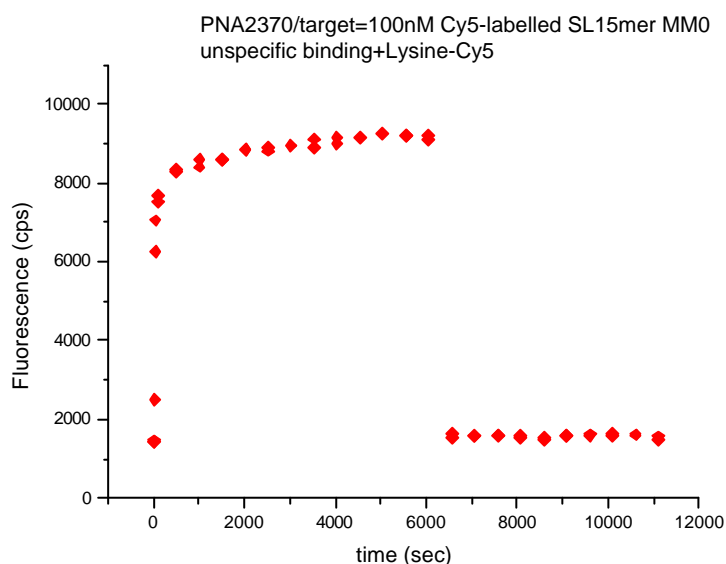


Figure 4: Unspecific binding measurement between Lysine and dye.

4.1.4 Single kinetic measurements

Single kinetic measurements analyze the association and dissociation phases of PNA-DNA hybridization. The association phase involves the hybridization process with the target. After saturation is reached, rinsing is started. Thus the dissociation phase is triggered.

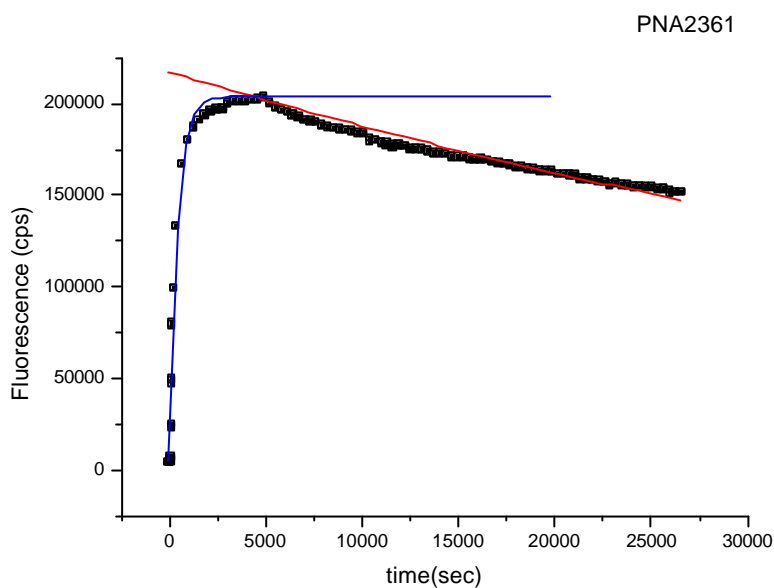


Figure 5: Single kinetic measurement of PNA2361 with 100nM target concentration in 10 mM PB.

Figure 5 shows the hybridization measurement of the surface immobilized PNA probe 2361 with a fully complementary (MM0) Cy5-labeled DNA target. We should mention here that PNA2361 does not contain any modification on its backbone. Thus, all results could be compared with values of the unmodified PNA. The fluorescence vs. time plots can be analyzed fitting the association and dissociation phases by the Langmuir model. In Fig.6, the blue and red lines represent the fitting curves.

Other kinetic curves are shown in Fig.6, B, C and Fig.7 A,B for PNA2364 and PNA 2367 respectively. In Fig.6-A and Fig.7-A, the kinetic measurements were done using 100nM target after regenerating the surface two times. Since the target concentration is relatively high, a fast association is observed. But if we zoom in to the association part of the measurement in Fig6-aa the hybridization could be well resolved with an increase of the fluorescence signal with time. The Langmuir fitting of the single kinetic measurements are shown in Fig.6-B and Fig.7-B. The blue line in the figure indicates the fitting of the association, the red line for the dissociation part. Another measurement which is shown in Fig.6-C represents the measurement which was done in order to investigate the affect of flow rate on the binding reaction. In this measurement, the target concentration was reduced to 10nM in order to slow down the association phase hence get a better fitting.

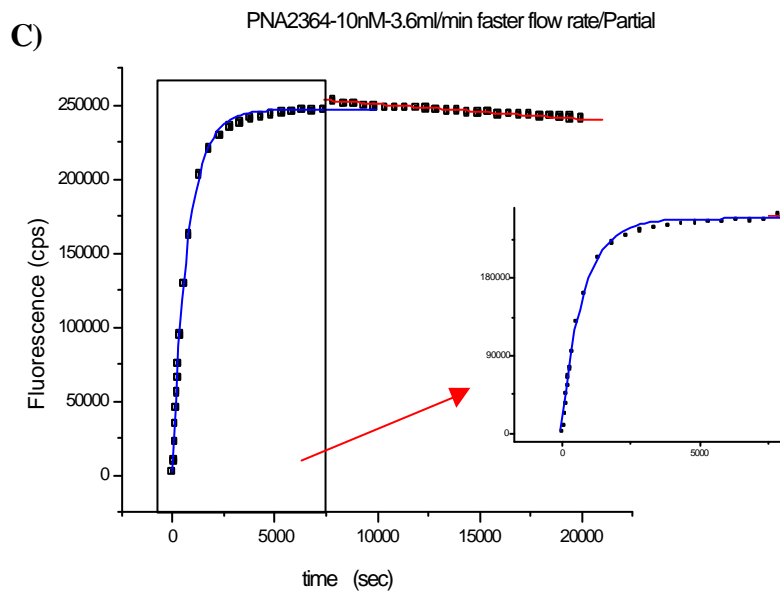
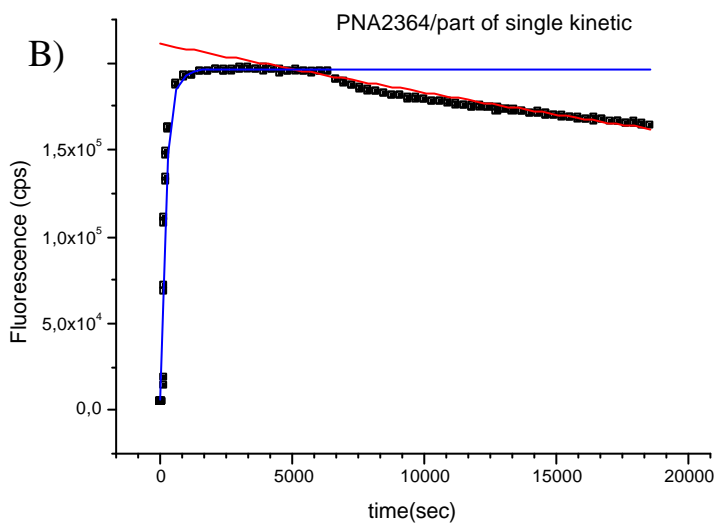
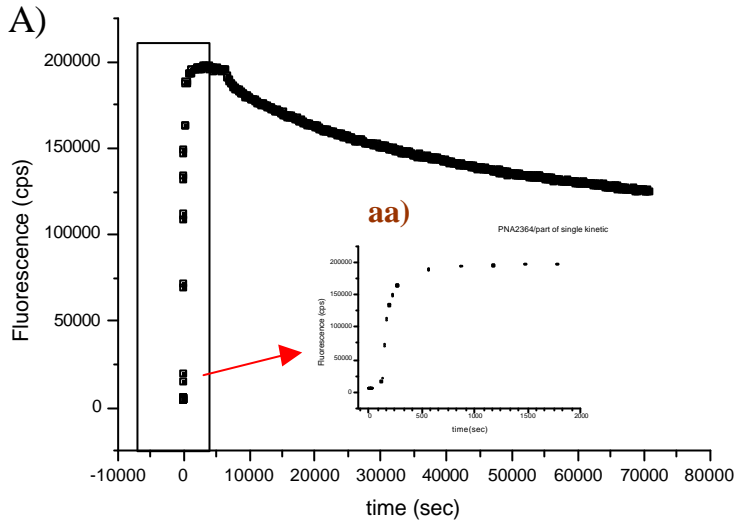


Figure 6: A) Single kinetic measurement of PNA2364 and B) its Langmuir fit with the flow rate 2.5ml/min. C) same kinetic measurement with a faster flow rate, 3.6ml/min and using 10nM target concentration and zoomed-in plot of association (small graph)

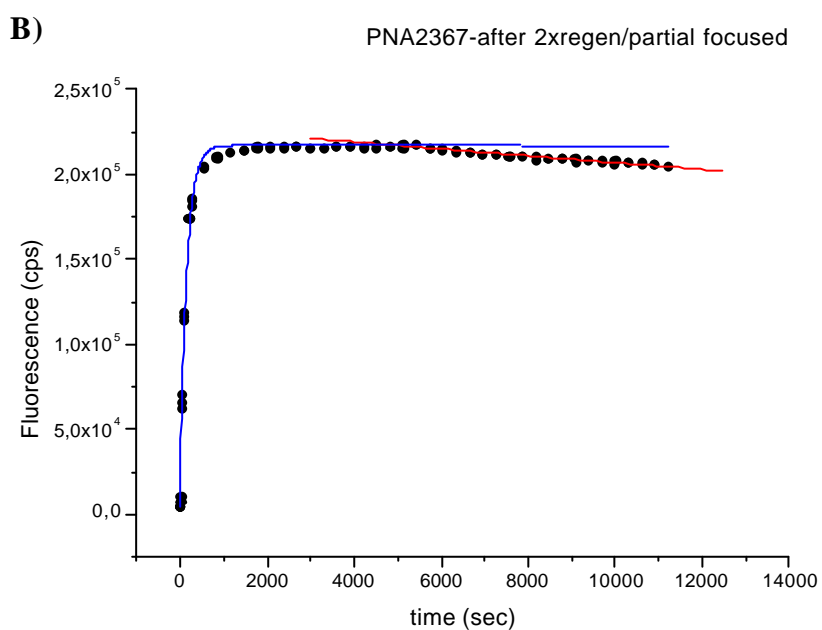
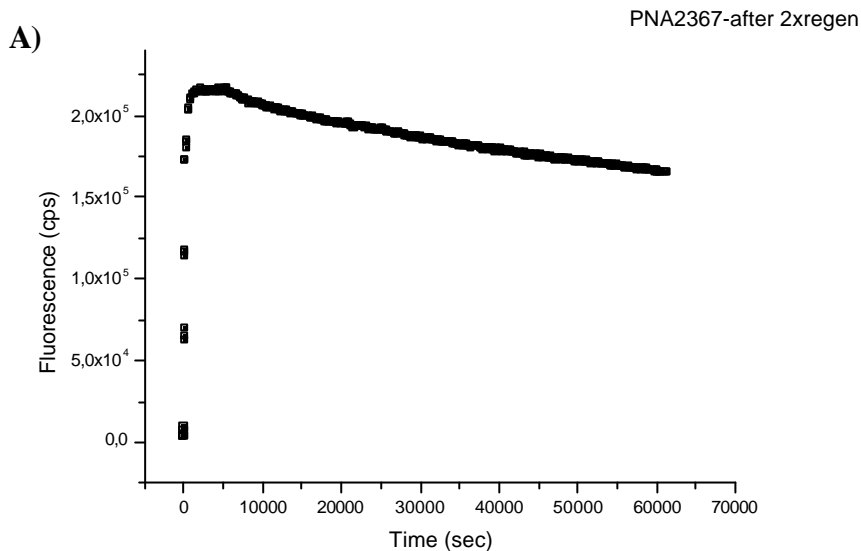


Figure 7: A) Single kinetic measurement of PNA2367 after twice regeneration of the surface and B) Langmuir fitting of kinetic curve.

In the case of PNA2370 (Fig 8-A), besides a standard experiment that was carried out for all other PNAs, a single MisMatch (MM1) target was also used in order to observe the affinity difference between the fully complementary MM0 situation and a single MM cases (Fig 8-B).

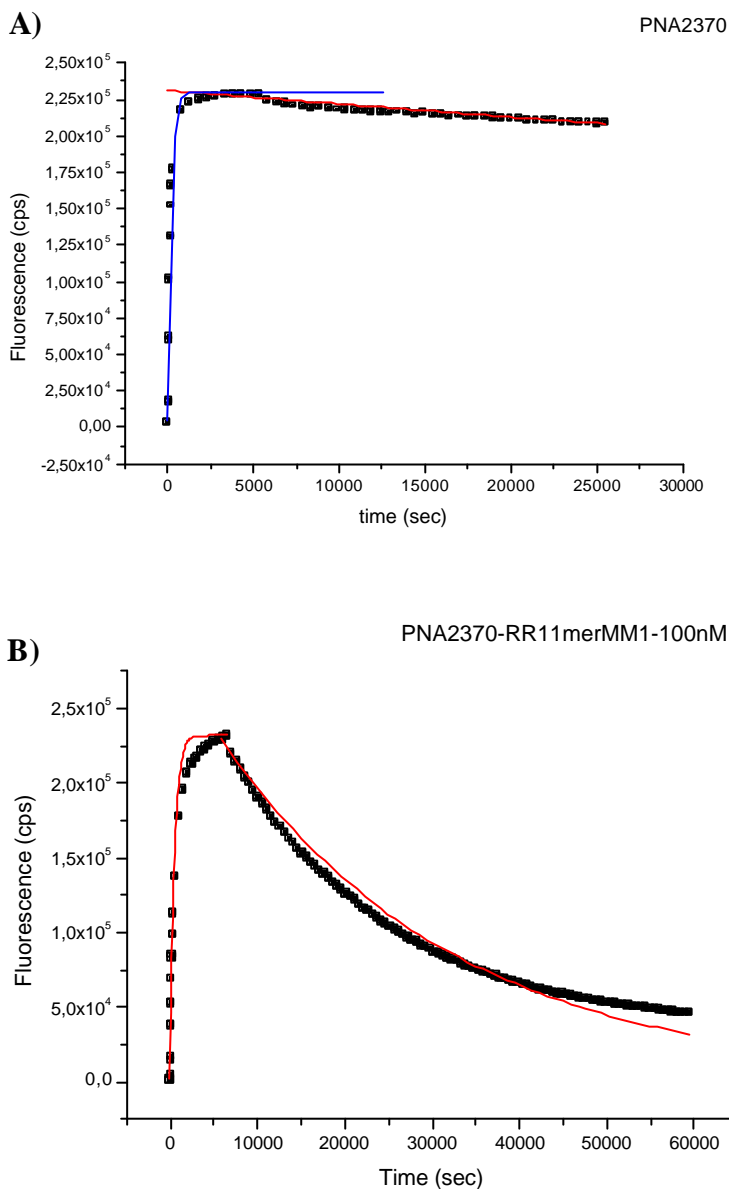


Figure 8: A) Single kinetic measurement of PNA2370 and B) MM1 case with 100nM target

Comparing the MM0 and MM1 hybridization kinetics, one can see that the difference is most pronounced in the rinsing phase even though the association phase looks similar. In the MM1 case, for which the duplex is not as stable as in MM0 case, the target is rinsed out much faster. One should also admit that the fitting in Fig.8B is not in as good as in the MM0 cases but the single mismatch difference could be seen very clearly.

In order to observe ionic strength effects, single kinetic experiments for PNA2370 were also performed in PBS(137mM NaCl, 10mM Phosphate) buffer using a 500pM concentration. As it can be seen from Fig.9, the kinetic has been slowed down due to the very low target concentration and it took almost 10hrs to reach the saturation.

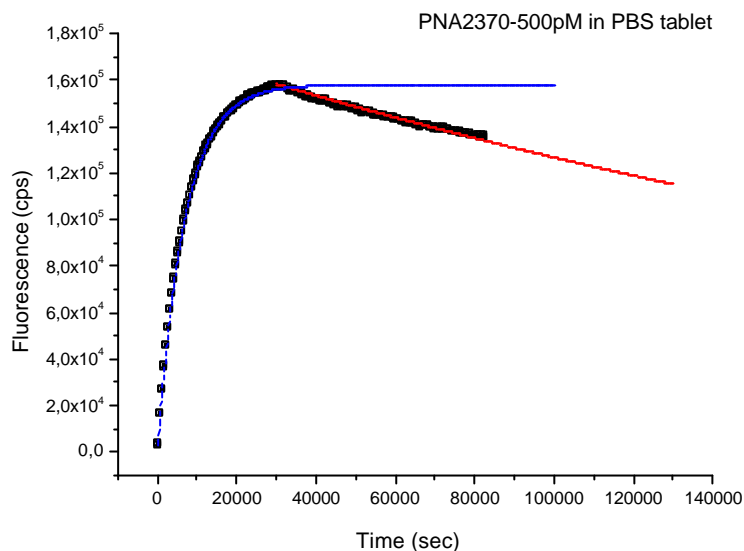


Figure 9: Single kinetic measurement of PNA2370 with 500pM target concentration in PBS

In Fig.10, the single kinetic measurements of PNA2376 and PNA2379 are shown. As it can be seen from the plots that the fitting of the association part is not in good agreement with the measurement data. The saturation fluorescence level, according to the fitting, is reached in shorter time than actual experimental time. In our studies we follow the assumption that oligonucleotide hybridisation does follow the Langmuir model. In this case the description is no longer accurate. The binding phenomenon is more complicated than in the single exponential case.

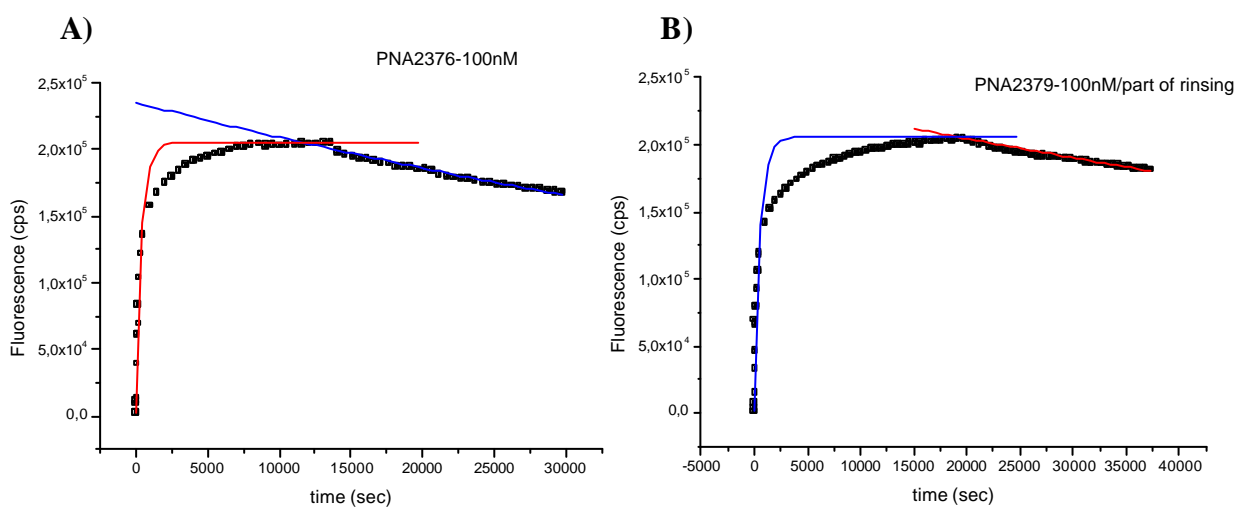


Figure 10: Single kinetic measurement of A) PNA2376 and B) PNA2379 with 100nM target

If we look into the kinetic curves more carefully, one can observe a common deviation from the fitting curves of the dissociation phase in all the kinetic measurements for longer rinsing times. That might originate from insufficient rinsing of the cell, leaving a substantial volume of complement solution in “dead corners” of our cell. This then leads to gradual recovery of complement concentration in the cell and hence to an appreciable degree of re-adsorption to the probe sites at the interface as we can see the example in Fig.6.

The kinetic constants that were obtained from Langmuir fittings are summarized in the Table 2 below.

Table2: Kinetic constants of the PNAs with 100nM Target concentration in PB buffer that was obtained after Langmuir fitting,

PNA name	k_{on} ($M^{-1}s^{-1}$)	k_{off} (s^{-1})	K_a (M^{-1})	K_d (M)
2361	2.3×10^4	2×10^{-5}	1.2×10^9	8.3×10^{-10}
2364	4.4×10^4	1×10^{-5}	4.4×10^9	2.3×10^{-10}
10nM target & flow rate 3.6ml/min	1.2×10^5	4×10^{-6}	3×10^{10}	3.3×10^{-11}
2367	6.2×10^4	9.8×10^{-6}	6.3×10^9	1.6×10^{-10}
2370	4.7×10^4	4.2×10^{-6}	1.1×10^{10}	9×10^{-11}
in PBS with 500pM target con.	2.8×10^5	3.2×10^{-6}	8.7×10^{10}	1.1×10^{-11}
MM1 target	1.9×10^4	4×10^{-5}	4.8×10^8	2.1×10^{-9}
2373	5×10^4	1×10^{-5}	5×10^9	2×10^{-10}
2376	2.4×10^4	1×10^{-5}	2.4×10^9	4.1×10^{-10}
2379	1.8×10^4	5.8×10^{-6}	3.1×10^9	3.2×10^{-10}
flow rate 3.6ml/min	2.7×10^4	7.6×10^{-6}	3.6×10^9	2.8×10^{-10}

The overall affinity constant of the surface binding is denoted by K_a , which is the association constant, k_{on} , divided by dissociation constant, k_{off} . The value K_d , which is reciprocal of K_a , is correlated to the target concentration at which half of the surface binding sites will be occupied.

If the numerical values of K_a , given in the Table2, is plotted against the ΔT_m values (Fig.11), one can see that the change in the K_a values follows the trend of the ΔT_m plot. Only two PNAs, 2376 and 2379 should have shown higher K_a values compared to that of PNA2370. But general speaking, the increase in affinity constant follows almost the same trend as ΔT_m shows. Again if we look at the kinetic measurements of PNA2376 and PNA2379 (Fig.10-A and B), one can see a substantial deviation between the experimental data and the Langmuir fit, which is obvious, different from the other PNAs' fitting of the association phase. Hence that would effect the numerical value of K_a . Beside that the main reason could be the deviation from Langmuir model. In Langmuir model, we follow the assumption that the molecule does not interact with the neighboring one. But as that can be also seen from the association phase of the single kinetic measurement, the binding phenomenon is more complex.

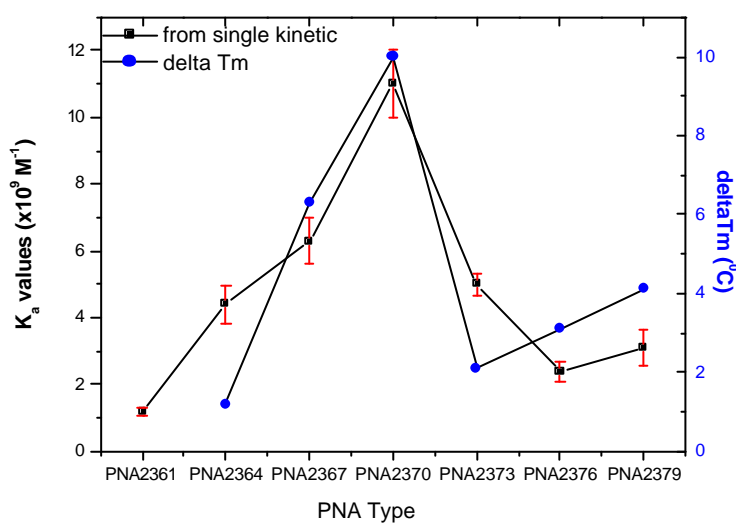


Figure 11: Plot of K_a from single kinetic measurement and ΔT_m for PNA type.

A couple of measurements were done in order to probe the effect of the flow rate on the hybridisation process. Two different PNAs, PNA2364 and PNA2379, were measured at two different flow rates, i.e., at 2.5ml/min and at 3.5ml/min. In both cases, the increase of the flow rate caused an increase in the affinity constant. However, the effect of flow rate is more pronounced for PNA2364 than for PNA2379. What is totally unclear at this moment is the binding that the single kinetic

experiments with two different concentrations in the PNA 2364 result in a changed K_a value in clear disagreement with the Langmuir picture. Some discrepancies in the fitting of the association phase due to faster binding and not enough data points collected (in order to avoid photobleaching) might also contribute to that result.

In the case of PNA2370, another measurement related to mismatch discrimination was performed. As it can be seen from the K_a values, the difference between the affinities of MM0 and MM1 is about 2 order of magnitude. The difference comes from both, the association and the dissociation constants: in the case of MM1, the target hybridisation with the probe is slower and the target dissociates faster upon rinsing. That clearly indicates that mismatch discrimination by using PNA can be a promising way for future applications.

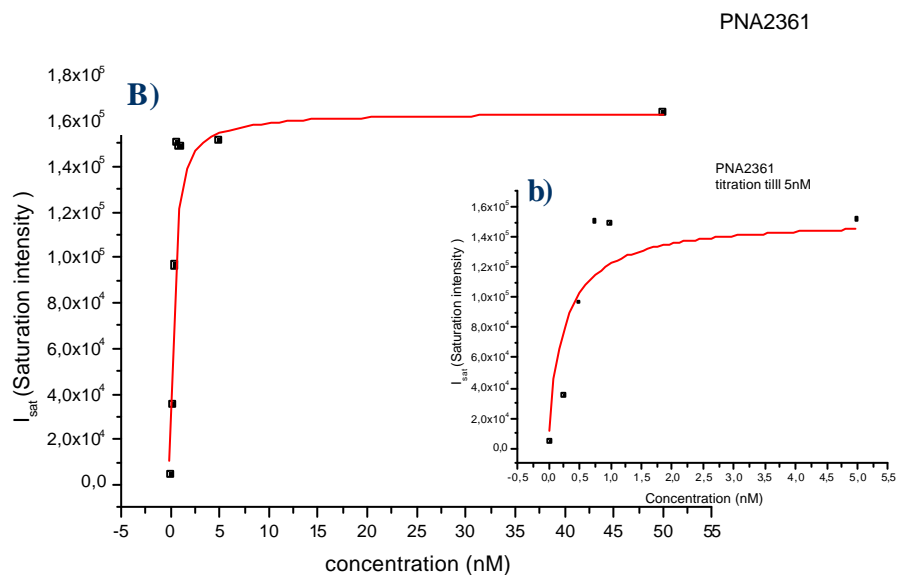
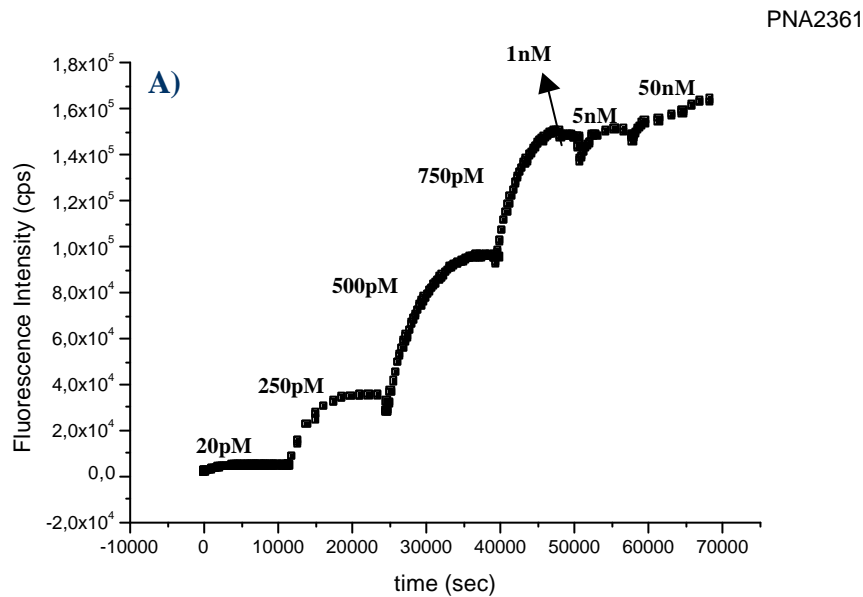
4.1.5 Titration experiments

Titration experiments were performed to further elucidate the hybridization behavior of the PNA probes. By this approach, we aimed to establish a better correlation of the values shown in Table 2. Titration experiments are also technically significant because they offer a way to obtain K_a directly by quantifying the correlation between the bulk target concentration and the surface coverage. In a titration experiment, the concentrations are chosen according to the K_d value of the probe, obtained from single kinetic experiments. The starting concentration has to be much lower than the K_d value with the final concentration being substantially higher in order to fully saturate the probe surface. After reaching saturation, an angular scan is performed to correlate the surface coverage with the obtained fluorescence intensity. The maximum fluorescence values from the angular scan curve for each concentration are plotted against the concentration.

Fig.12-A, shows a titration experiment for PNA2361 along with the resulting plots illustrating the conventional (Fig12-B) and the linearized (Fig12-C) relationship between target concentration and corresponding saturation intensity. The range of the target concentration that has been chosen for the titration experiment was defined according to the K_d values obtained from the single kinetic measurements of each PNA. As it was described before, the K_d value gives the target concentration at which 50% surface coverage is achieved. Since the K_d values of the PNAs are in the 10^{-10} range, starting target concentration in the pM range were chosen.

The graph in Fig.12-B was derived from the saturation values of each concentration. Each time the angular scan was completed, the goniometer was tuned back to the angle of the 30% reflectivity value and another higher concentration was injected.

The Fig.12-B and 12-C show the Langmuir isotherm and the linearized Langmuir isotherm up to target concentration of 5nM value in order to allow for a precise the fitting.



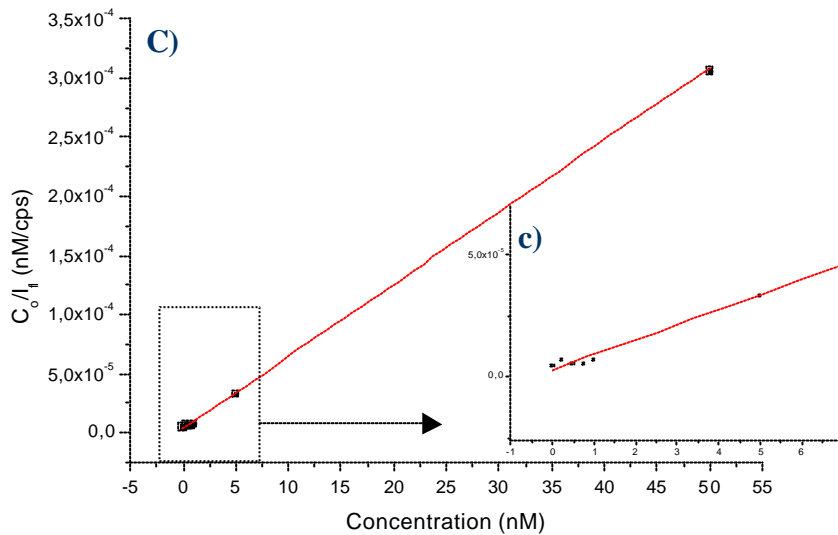


Figure 12: Titration curve of PNA2361 A) MM0 titration experiment B) conventional representation and C) linearized isotherm plots relating target concentrations with respective saturation intensity and b) and c) focused plots of B) and C) respectively.

As it can be seen from Fig12, a satisfying level of agreement is found between the experimental data points and the fitting curve in the conventional plot 12-B. However, discrepancies in the fitting can be seen more clearly if the curve is linearized.

The Langmuir isotherm can be also obtained from fluorescence scans taken after each target concentration had reached saturation in the same titration measurement. Since the fluorescence angular scan is following the surface coverage, the same Langmuir picture can be seen.

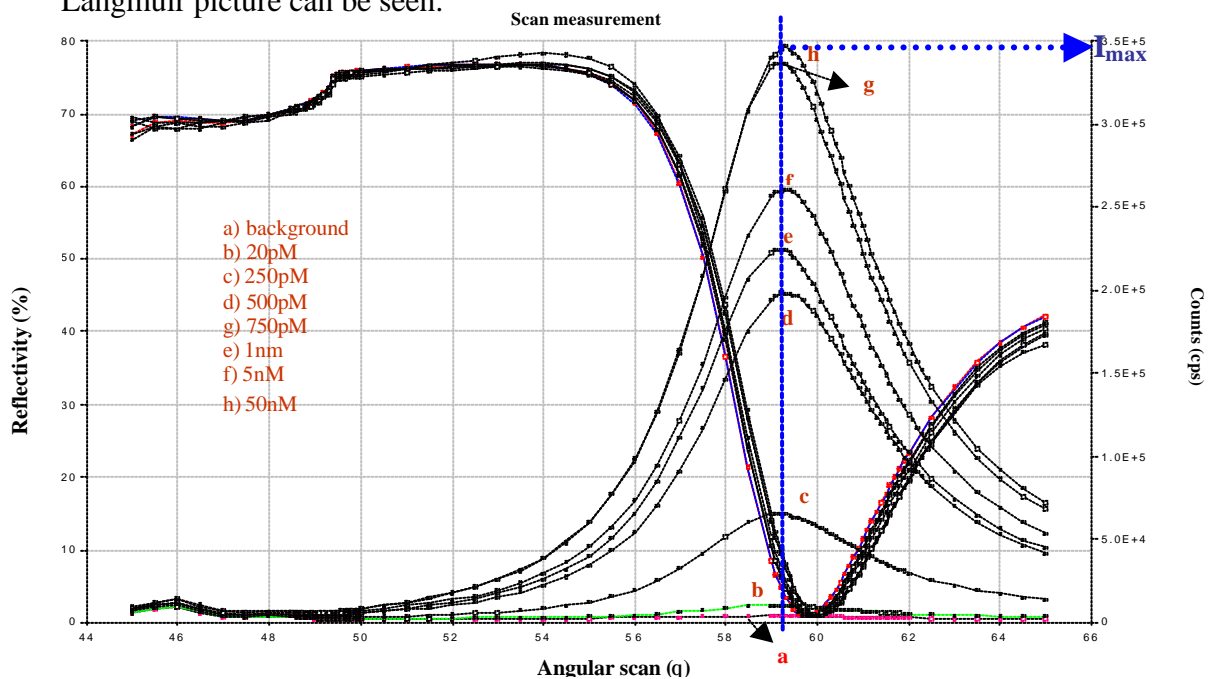


Figure 13: Angular scan with fluorescence after saturation of each target concentration in the titration measurement.

The typical angular scan measuring the reflected light, as well as, monitoring the fluorescence intensity is given in Fig.13. If the maximum fluorescence intensity in the scan curves for each concentration is plotted against the respective concentration, the same Langmuir behaviour is observed as can be seen in figure 14-A and in the linerized plot in Fig.14-B.

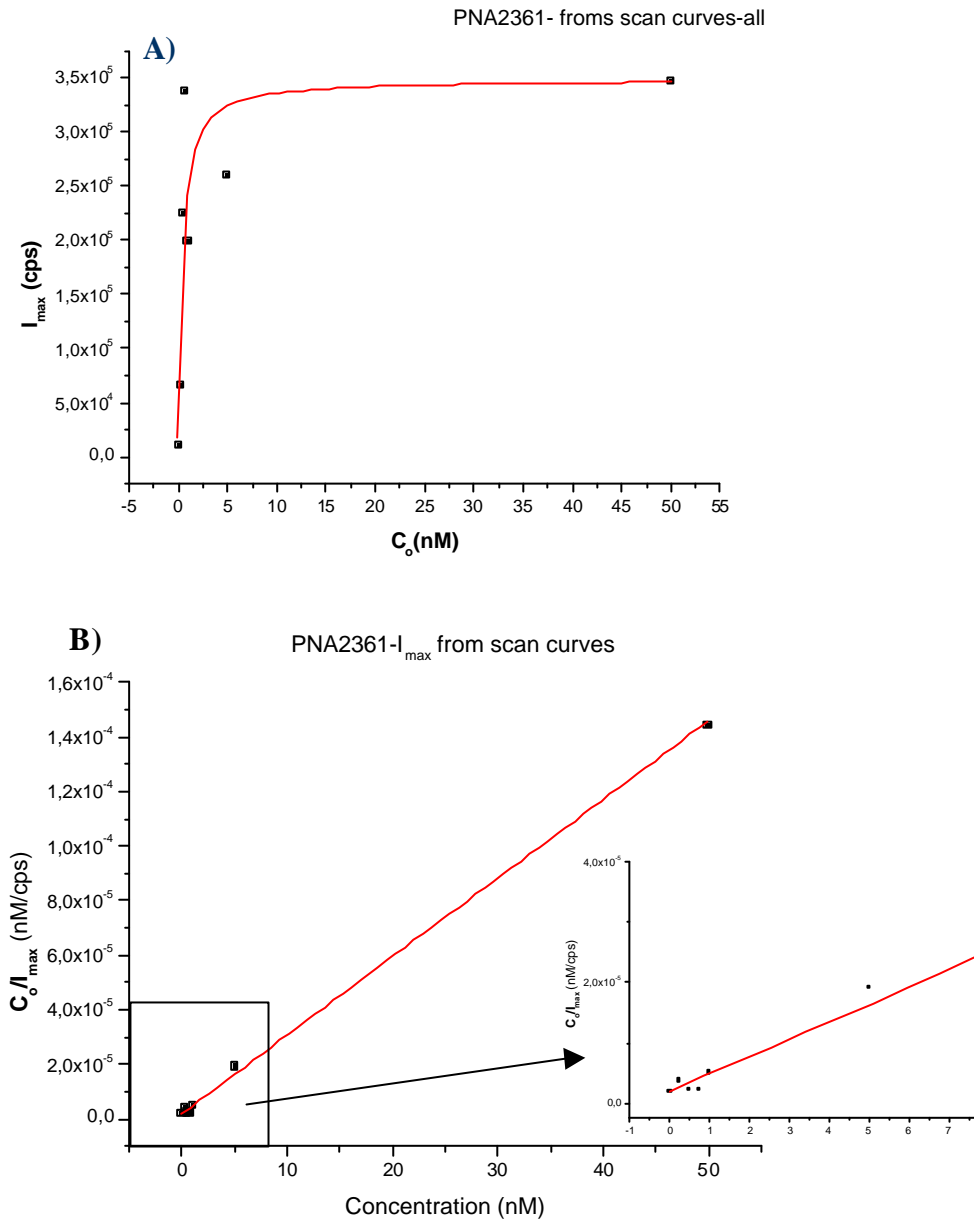


Figure 14: Langmuir isotherm (A) and linerized plot (B) of PNA2361 derived from angular scan with fluorescence

Fig.15 shows a similar analysis for an experiment carried out with PNA 2379 measurements.

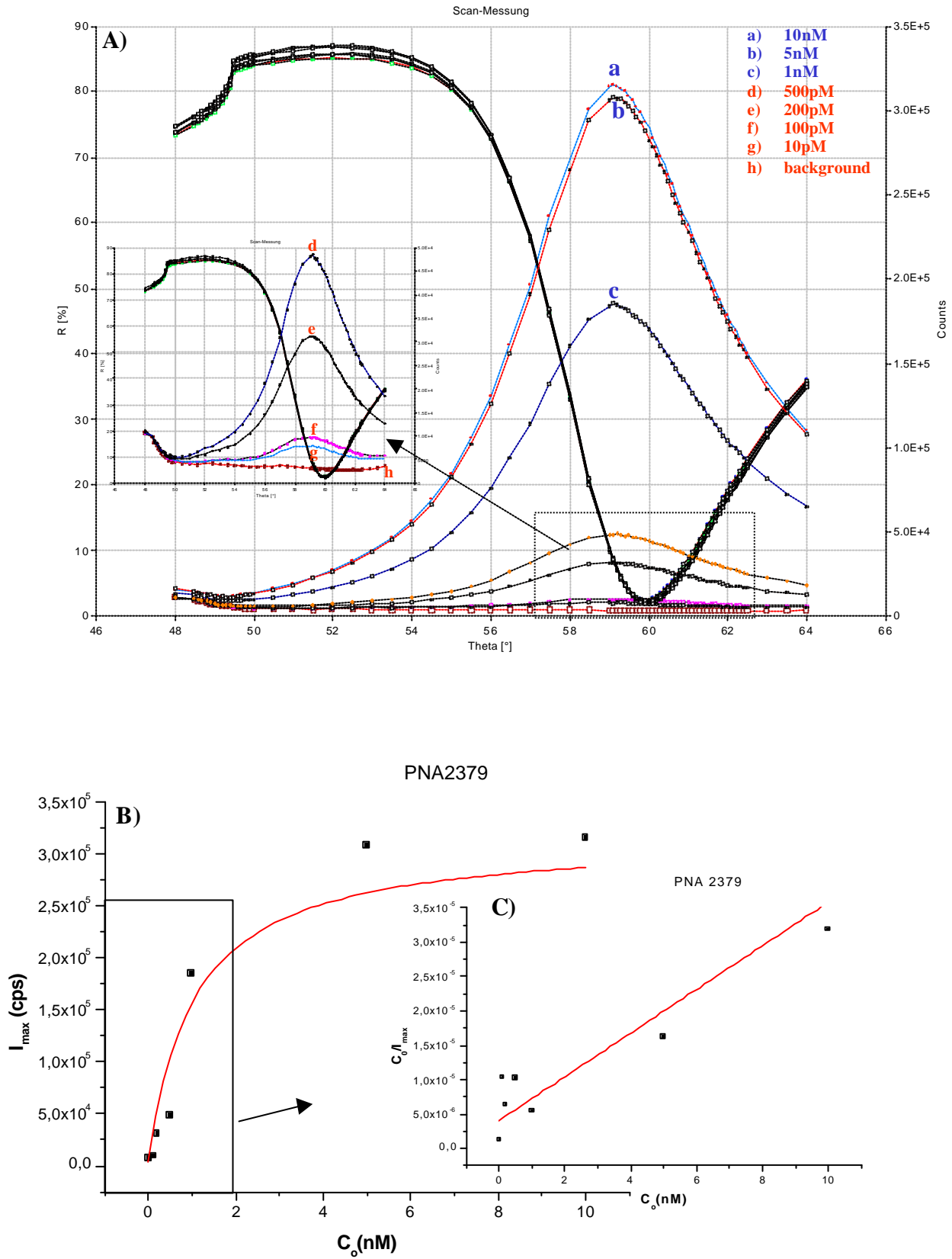
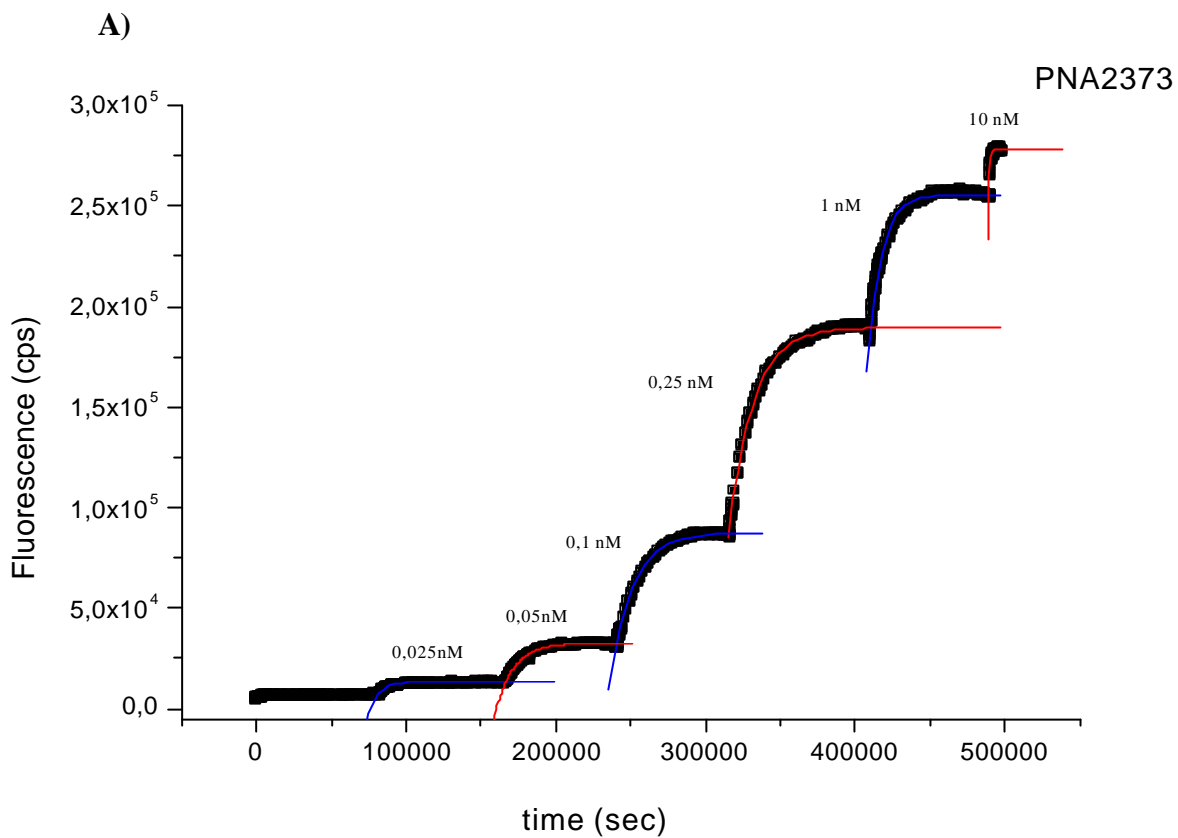


Figure 15: A) Angular Scan with the fluorescence after each concentration saturation in titration measurement B) Langmuir isotherm C) Linearized curve of PNA2379 derived from angular scan with fluorescence

The fitting in Fig.15 is not in good agreement with the data. If we look at the scan curve of the PNA2379, one can see that the increment in the I_{\max} values of 10, 100 and 200pM samples are just above the background level. Because of those low concentrations, the fitting shows some disagreement with the expected Langmuirian behavior.

Equivalent titration curves for PNA2373 and the derived isotherms are given in Fig.16A and B. Since the titration measurements are carried out using different concentrations of the target, each step refers to the association phase of a single kinetic measurement. Hence we can fit the association phase for each concentration and obtain concentration dependent k_{on} values. Since the disassociation is independent of the concentration (according to the Langmuir model), k_{off} values from a single kinetic measurement were used in the calculation of the affinity constant. Different to that approach, the k_{off} values for PNA2370 were obtained from Langmuir fitting for each rinsing step during the titration measurement. It can be seen from Fig.17 that the k_{off} values, indeed, do not change with concentration confirming the assumption made above based on the Langmuir model predictions.



B)

C_0 nM	k_{on} $M^{-1}sec^{-1}$	K_a a) M^{-1}
10	1.1×10^5	1.1×10^{10}
1	9.4×10^4	9.4×10^9
0.2	2.1×10^5	2.1×10^{10}
0.1	5.5×10^5	5.5×10^{10}
0.05	1.4×10^6	1.4×10^{11}
0.025	5.7×10^6	5.7×10^{11}

a) assuming a constant k_{off} -value, $k_{off} = 10^{-5} s^{-1}$

Figure 16: A) titration measurement of PNA2373 and B) Langmuir fitting results for association phase (k_{on}) of plot A.

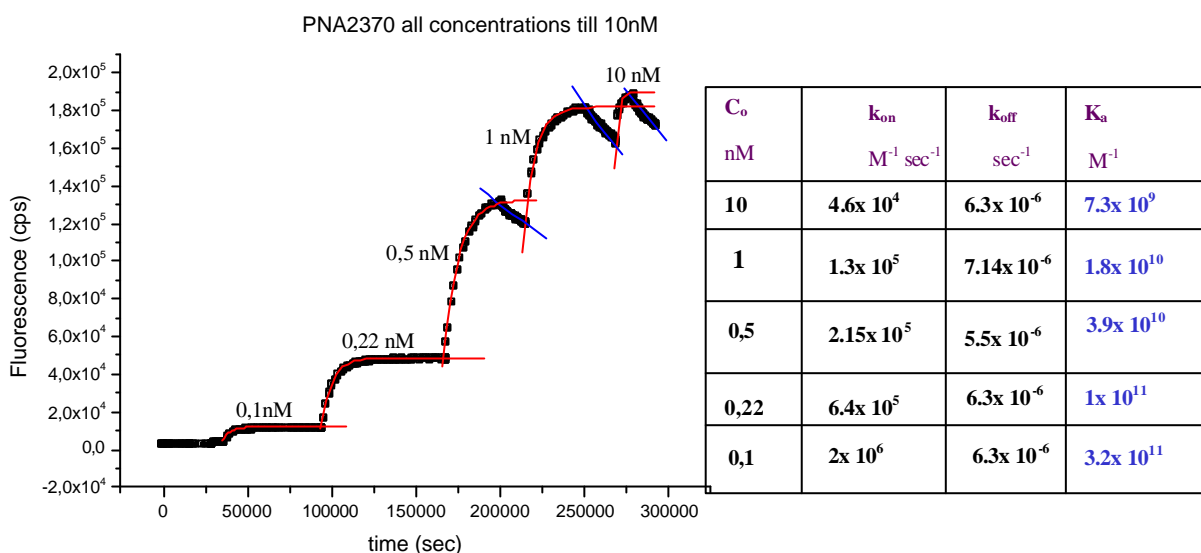


Figure 17 : Titration measurement of PNA2370 and summary of the k_{on} , k_{off} values from the fitting of plot A and calculated affinity constant from k_{on}/k_{off}

The results from both titration measurements, i.e., based on saturation levels (I_{sat}) and on the max. intensity from the scan measurements, are summarized in Table 3.

Table 3: Affinity constant and half saturation value obtained from titration measurement for all PNAs

PNA name	From saturation value (I_{sat})		From angular scan curves (I_{max})	
	K_a (M^{-1})	K_d (pM)	K_a (M^{-1})	K_d (pM)
2361	4×10^9	250	2.5×10^9	400
2364	1.1×10^{10}	92	1×10^9	1000
2367	1.3×10^{10}	76	2.5×10^{10}	40
2370	2.9×10^9	350	3×10^{10}	330
2373	5.6×10^9	180	5.9×10^9	170
2376	1.5×10^9	660	1.9×10^9	530
2379	1×10^9	1000	1×10^9	1000

The affinity constants obtained from the saturation values and the angular scans show slight differences most likely as result of bulk contribution. If we looked again back to the experimental procedure, the rinsing step starts right before the angular

scan is processed. After completing the scan measurement, the next higher concentration is injected and the same procedure is being repeated after reaching the next saturation level. Hence, if we plot the Langmuir isotherm curve taking into account the fluorescence intensity at the saturation levels, the signal might contain bulk contributions. However, this is only significant if we are in the high concentration regime. At the beginning of the titration, we are always far below the saturation level and we are dealing with the mass transfer dominant regime.

If we compare the K_a values obtained from the kinetic experiments with those from titration measurements (see Fig. 18), a fairly good agreement can be seen considering that the numbers are derived from a statistical analysis with error bars and evaluated with a theoretical model that certainly has some intrinsic limitations.

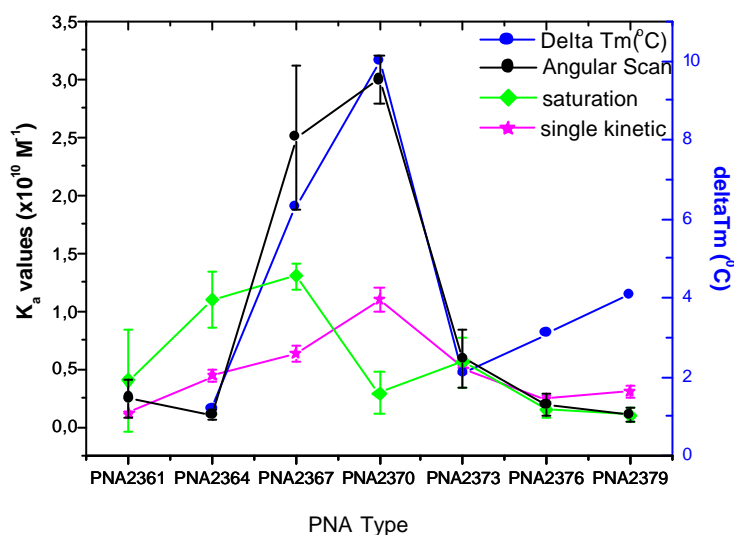


Figure 18: Comparison of K_a values obtained from single kinetic, saturation and angular scan measurements for the all PNAs

If all K_a values from single kinetic and titration measurements are compared, there is a slight increase in the all obtained K_a values as modification intended for. If we plot all the K_a values and increase in melting temperature for the different modified PNAs (Fig.18) we can see that all PNAs except PNA2376 and 2379 follow the same trend that ΔT_m shows. Especially the K_a values obtained from angular scan show a good agreement. The results obtained for PNA2376 and 2379 are not in a agreement with the increase in the T_m values. As we discussed for the single kinetic data, there might be again some fitting discrepancies that affected the results. But one should also

mentioned that the hybridization process is more complicated than described by the Langmuir model and there might be additional features happening during the hybridization that our technique is unable to detect.

Other possibility is that our probe matrix could be dense in terms of space per strand thus causing cross talk. Unfortunately, experiments with the diluted matrix haven't been performed. However, the diluted matrix affect has been studied by Dr. Yao in the group in her PhD thesis and reduced cross talk between the neighboring strands was observed.

Another fact related with the titration measurement is surface charges. After the first concentration, the surface become occupied by target DNAs which bring negative charges to the surface. If the next target concentration is injected, it has to overcome this Coulombic barrier in order to find the probe strand. This makes the binding process more complicated and might cause the disagreement with the Langmuir model.

4.1.6 Global Analysis:

The Global analysis method is based on applying a non-linear least square analysis and simultaneous fit to the association and disassociation phase data generated for a range of DNA concentrations injected into the sample cell. This method simply indicates that effects related to the probe surface, such as ionic strength or bulk contribution, does not complicate the observed responses. Each measurement is performed on a surface which is completely unoccupied by the target. However, the affect of the regeneration of the surface should not be ignored.

How to do “Global fitting”:

1. Kinetic experiments are performed for ~5 concentrations (>half saturation), giving 10 minutes for the association, and 10 minutes for the dissociation (Fig.19) at a fixed resonance angle for which the reflectivity is 30%;

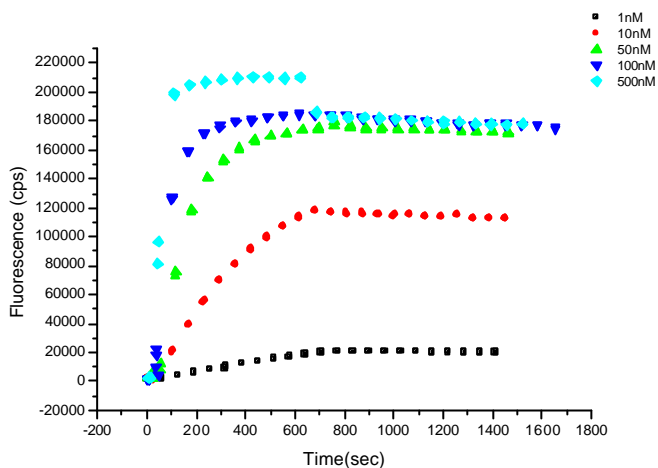
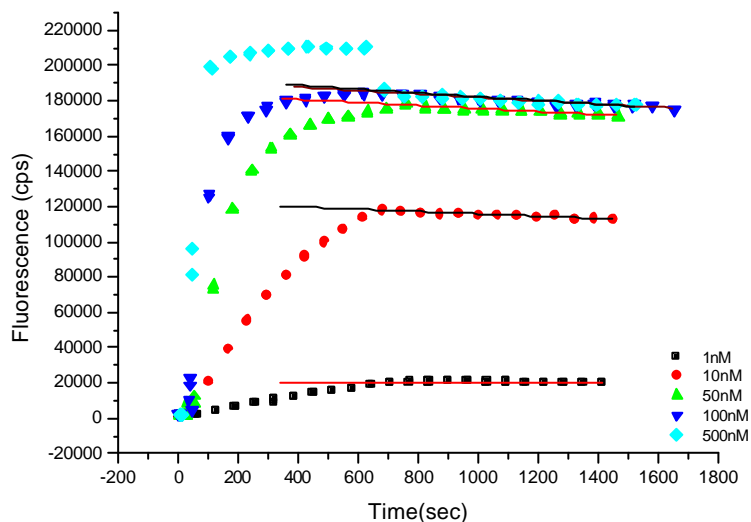


Figure 19: Single kinetic measurement for 5 different concentration

2. The dissociation phases is described by $I = I_0 \cdot \exp(-k_{\text{off}} \cdot t)$, which results in a k_{off} value for each concentration. Typically, these values are then averaged to yield a k_{off} value (Fig.20).



C_0 (nM)	k_{off} (s^{-1})
1	0.00007
10	0.00006
50	0.00005
100	0.00005
500	0.00006

$k_{\text{off average}} = 5.5 \times 10^{-5} \text{ s}^{-1}$

Figure 20. Langmuir fitting for dissociation phase of each concentration

3. The association phases is described by $I=I*(1-\exp(-k_a*t))$, resulting in a k_a value for each concentration (fig.21-A,B,C, and D)

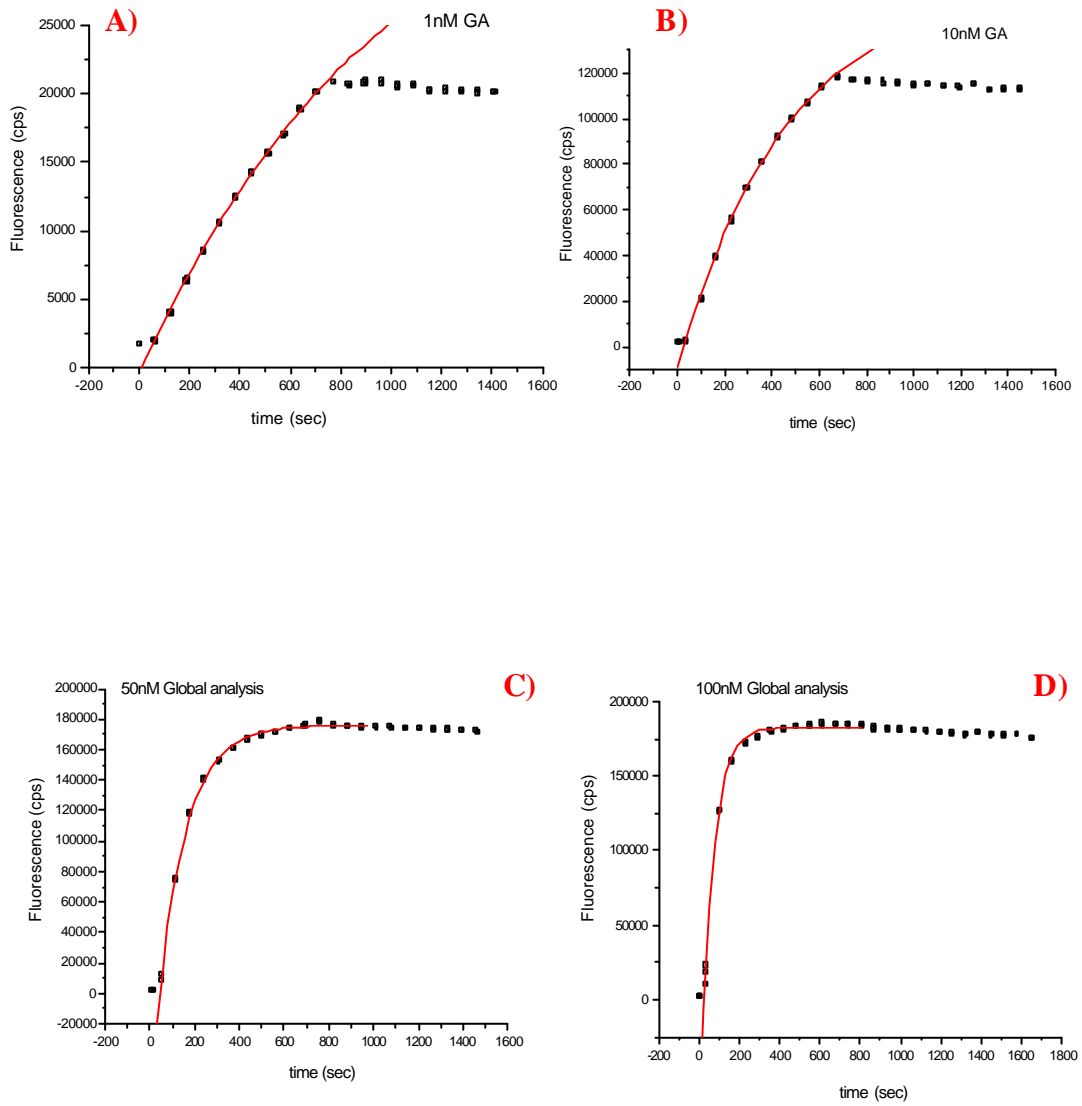


Figure 21: Langmuir fitting for the association phase of A) 1nM, B) 10nM, C) 50, and D) 100nM target concentration

4. The k_a values are plotted versus the concentration with a linear fit that gives slope k_{on} (since $k_a = k_{on} \cdot c_0 + k_{off}$) (Fig.22).

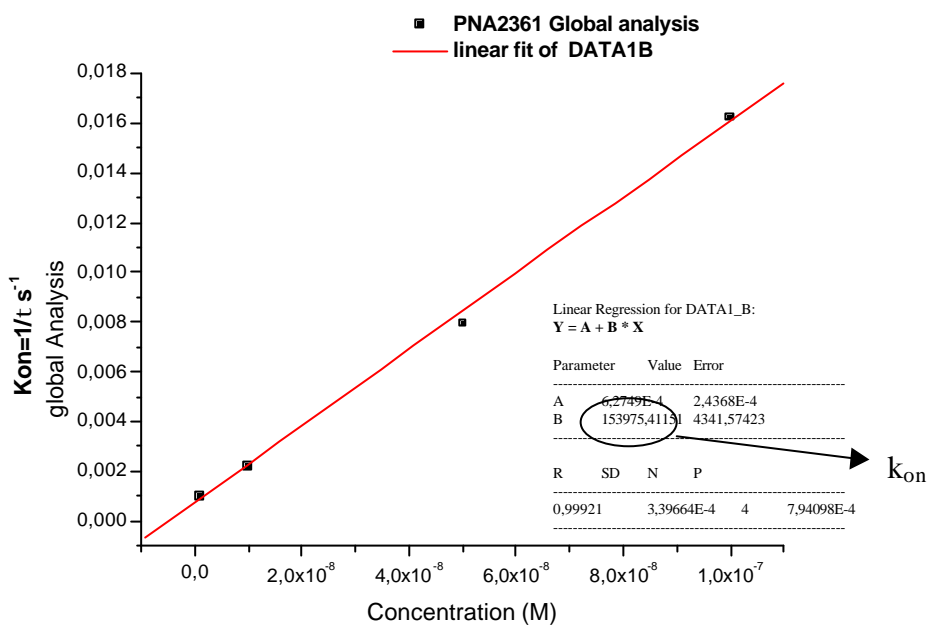


Figure 22. Linear fit of k_a vs. concentration plot

5. K_a and K_d are defined by dividing k_{on} and averaged k_{off} value

$$\left. \begin{array}{l} k_{on} = 1.6 \times 10^5 \text{ M}^{-1} \text{ s}^{-1} \\ k_{off \text{ average}} = 5.5 \times 10^{-5} \text{ s}^{-1} \end{array} \right\} K_a = 2.9 \times 10^9 \text{ M}^{-1} ; K_d = 3.6 \times 10^{-10} \text{ M}$$

The constants for all the PNAs above that were obtained from the Global Analysis measurement are summarized in Table 4;

Table 4: Summary of the values that were obtained from Global Analysis for each PNA

PNA name	k_{on} ($M^{-1}s^{-1}$)	$k_{off,average}$ (s^{-1})	K_a (M^{-1})	K_d (pM)
2361	1.6×10^5	5.5×10^{-5}	2.9×10^9	360
2364	4.5×10^4	2.6×10^{-5}	1.7×10^9	580
2367	7.7×10^4	4.5×10^{-5}	1.7×10^9	580
2370	5×10^4	3.4×10^{-5}	1.5×10^9	680
2373	4.5×10^4	2.8×10^{-5}	1.6×10^9	622
2376	2.4×10^4	6×10^{-5}	4×10^8	2500
2379	2.1×10^4	8×10^{-5}	2.6×10^8	3800

If we compare the association constant obtained from the single kinetic measurements with those from GA as plotted in Fig.23, a good correlation is being observed, with a exception of PNA2361. For this system, the association constant from the single measurement is almost an order of magnitude smaller than the one obtained from the global analysis. However, the affinity constants, from two measurements, are in the same order of magnitude.

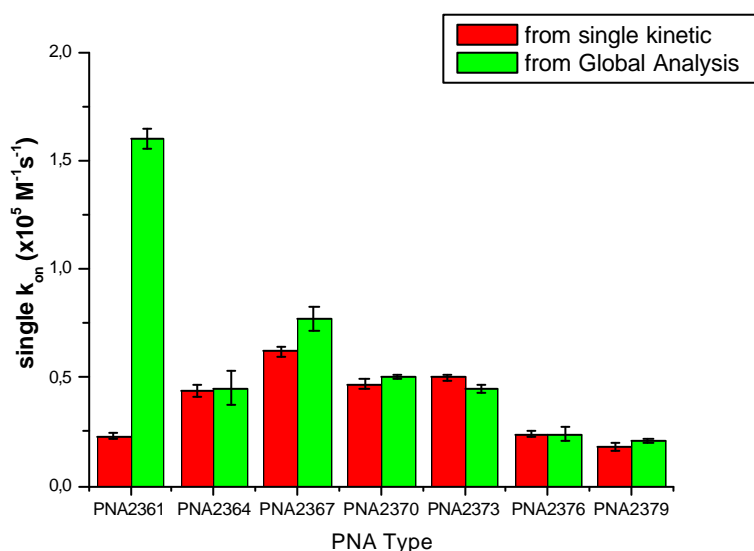


Figure 23: Comparison of association constant, k_{on} , obtained from Single Kinetic measurement and Global Analysis

We can do the same comparison for the affinity constants obtained from two measurements. As we have seen in Fig.23, the association constant differs in some cases, hence the K_a value will be effected. As can be seen in Fig.24 again, almost an order of magnitude difference is observed. It is also clear that there is no correlation between the affinity constants values which were obtained from single kinetic and global analysis measurement. But if we reconsider the k_{on} and k_{off} values for two measurements, one can see that the main difference comes from the dissociation rate constant values. Since a fully complementary target is used, hence rather stable duplexes are formed, 10min. rinsing phase is not sufficient to see significant dissociation that can be analysed quantitatively.

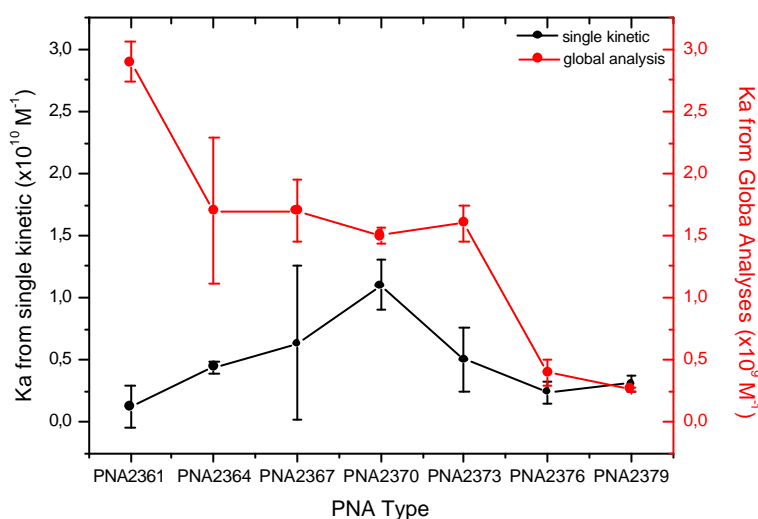


Figure 24: Comparison of the affinity constants, K_a , obtained from Single Kinetic measurement and from Global Analysis

If we plot the ΔT_m and the K_a values for each PNA, as is done in Fig.25, no correlation is observed.

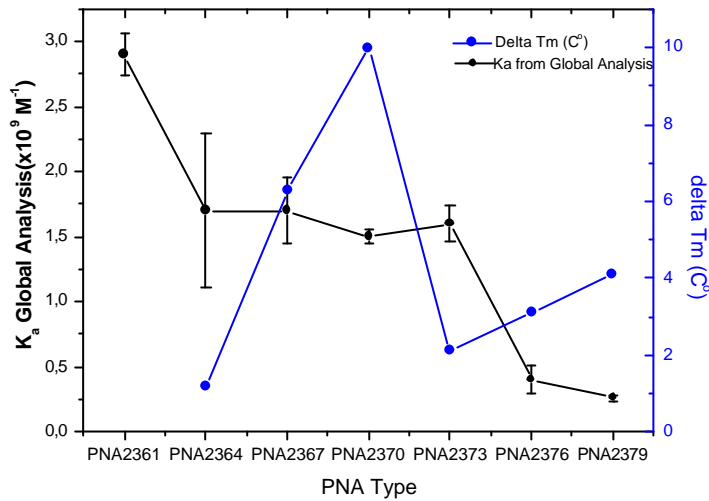


Figure 25: K_a from Global Analysis vs. ΔT_m

But if we have a close look to the overall picture in Fig.26 and plot all the K_a values that we obtained from the 4 different calculations and compare them to the difference in T_m , we can see that the increase in the change of K_a values only get closer to the change in T_m values when we use the angular scan values while the lowest K_a values were obtained with the global analysis method.

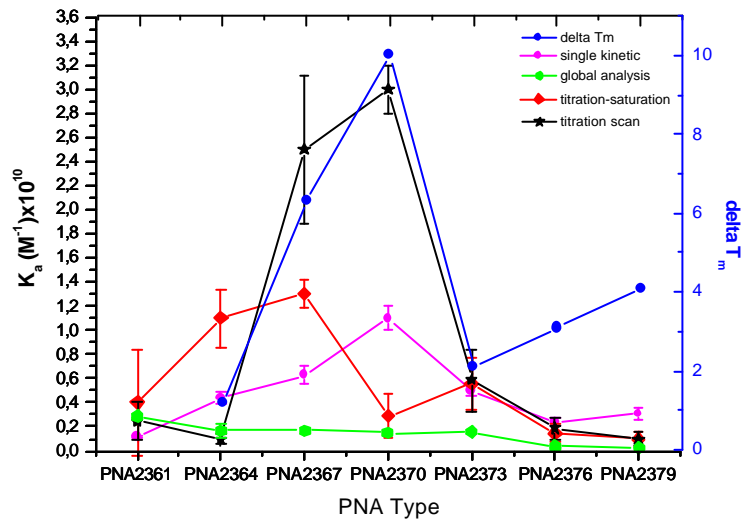


Figure 26: Plotting of K_a values obtained from Single kinetic, both Saturation and angular scan from titration measurements and Global Analysis measurement vs. ΔT_m

As a conclusion, we can say that the PNA-DNA binding process is more complicated than described by simple Langmuir model. Even though the bulk melting temperature of the PNAs shows a correlation upon modification, PNAs behaves differently when they are bound to the surface and the hybridization phenomenon does not follow the simple Langmuirian behavior most of the time.

Molecular dynamic simulations [Sotiva et al,2000] indicate that the highly flexible nature of the PNA backbone imposes energy penalties during the hybridization interaction. The flexible nature of the PNA backbone makes it difficult for the approaching DNA targets to relocate the recognition sites as compared to the DNA-DNA hybridization interaction, where the charged nature of the DNA makes the catcher probes stretched and thus, makes them easier accessible for the targets. Another possibility is that there might be structural changes that are occurring during the hybridization process. PNA is still a synthetic molecule that has a different structure compared to DNA. Orozco and co-workers [Orozco et al.1998] state in their studies that PNA molecules are not flexible enough that they can fit into any oligonucleotide counterpart, and its interaction with DNA requires some conformational changes. They have also shown that the internal energy of the PNA backbone results in the distortion of the DNA backbone during the hybridization process and they also emphasized that PNA demands a major change in the less flexible DNA backbone. Normally during the DNA-DNA hybridization, the basic structure of the individual DNA strands are altered via puckering of sugar units and backbone stretching beside the recognition sequence affinity [Zubay et al.1995]. Even though all those studies are performed in solution where the degrees of freedom are much higher than on our restricted surface, the natural tendency for changing conformation during the hybridization event might be more pronounced in our system resulting with a deviation from the Langmuir behavior. However that limitation could be avoided by using 3D dextran matrix in the future.

4.2 Surface Plasmon Fluorescence Microscopy (SPFM) studies of PNA-DNA interaction on microarrays

4.2.1 Aim

The aim of this study is to investigate PNA-DNA hybridization with the materials that have been discussed in chapter 4.1, using SPFM technique on an array platform. We obtain the affinity constants, and investigate the correlation of K_a values with the ones that were obtained from SPFS and T_m values. Since different PNAs have different binding affinities to the same target, that should result in a SPFM experiment in different intensity levels.

The materials are summarized in Table 1 below as a remainder. The red color letters represents the modifications that have been included in the backbone for reasons that have been discussed in the chapter mentioned above. The code names are given to the PNAs to simplify the names on the array according to the well numbers that they were spotted to.

Table 1: Structures of PNAs and their array codes in the experiment

Strands	Sequence	Array code
PNA 2361	5'-Biotin-(eg1) ₂ -AGA GTC AGC TT-Lys-NH ₂	(A3)
PNA 2364	5'-Biotin-(eg1) ₂ - DGA GTC AGC TT-Lys-NH ₂	(A4)
PNA 2367	5'-Biotin-(eg1) ₂ - DGD GTC AGC TT-Lys-NH ₂	(A5)
PNA 2370	5'-Biotin-(eg1) ₂ - DGD GTC DGC TT-Lys-NH ₂	(B5)
PNA 2373	5'-Biotin-(eg1) ₂ -AGA G(b1T)C AGC TT-Lys-NH ₂	(C5)
PNA 2376	5'-Biotin-(eg1) ₂ -AGA G(b1T)C AGC (b1T)T-Lys-NH ₂	(C3)
PNA 2379	5'-Biotin-(eg1) ₂ -AGAG(b1T)CAGC(b1T)(b1T)-Lys-NH ₂	(C4)
PNA 2523	5'-Biotin-(eg1) ₂ -AG D G(b1T)C DGC (b1T)T-Lys-NH ₂	(A2)
DNA2360 target	Cy5'-AAG CTG ACT CT-3	
Coupling Control (CC) Cy5-T15 TGT ACA TCA CAA CTA-Biotin		

First, the PNAs have been grouped in a 3x3 array. A non-specific Cy-5 labeled random sequence Coupling Control (CC) has been spotted on top of the array for focusing purposes of the CCD. That will allow us to focus the CCD camera optics without the need for any pre-hybridization with a highly concentrated target solution. All probes, in 1 μ M concentration, are spotted on a regular thiol mixture/streptavidin matrix with a pin-tool spotter.

The first array was spotted by using PNA 2367 (A5), 2370 (B5) and 2373(C5). As it can be seen from SPM image in Fig.1 which was captured in air. The spots are quite homogeneous and have almost all the same size of around 150-200 μ m in diameter.

In solution the array becomes invisible in SPM due to the low contrast. However, a scan measurement was always done with SPM performed to determine the resonance angle.

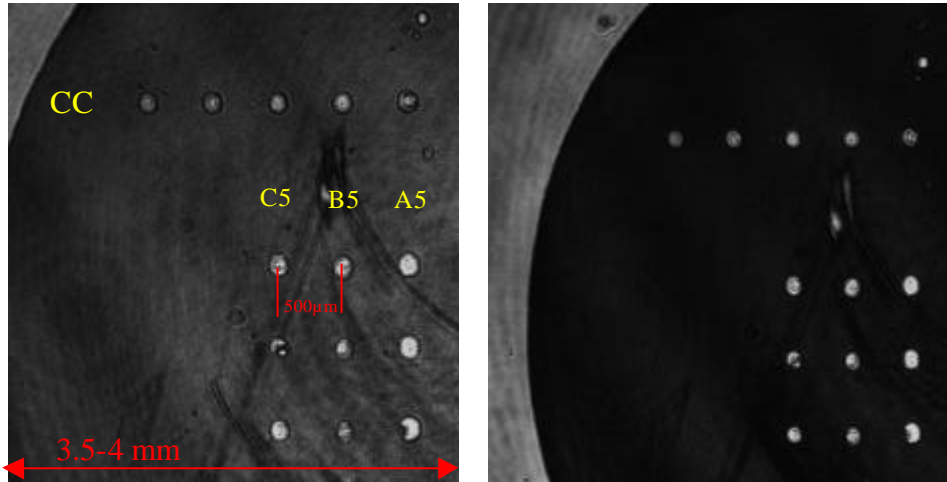


Figure 1: SPM image of Array 2A @ different resonance angle

Then the goniometer was tuned to θ_{res} and an interference filter was inserted in front of the CCD camera in order to capture for fluorescence image. First the background image with/without shutter open was captured as a reference that could be subtracted from the actual images. Fig.2-A shows the background image, which is captured with the laser blocked. The upper bright part of the image is back illumination of the CCD sensor. Then the shutter was opened, the laser illuminated to the sample and a background image was captured before any target injected. Fig.2-B below shows the fluorescence image without any target hybridized. Only fluorescence can be observed from the coupling control (CC) that was spotted for that purpose. The acquisition time for the images was 30sec.

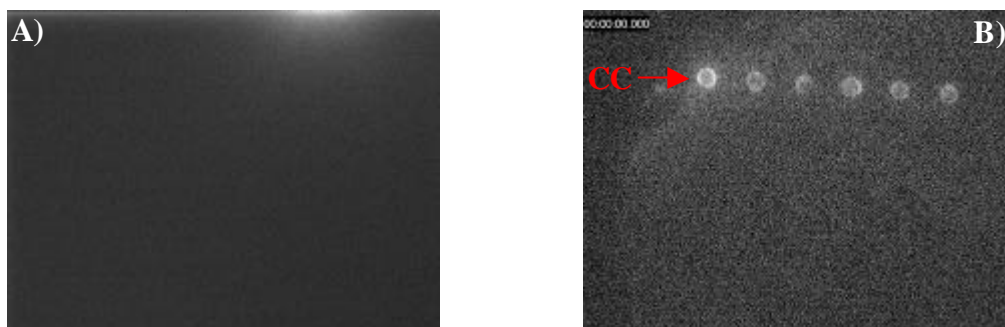


Figure 2: A) Background image

B) SPM image before any target injected

If the target is injected, it starts to “decorate” the array according to its affinity. However, since the K_a values of the 3 different PNAs spotted in the 3 rows are not very different as we found by SPFS studies, the image also will not show of a much difference in terms of intensity as it can be seen in the images in Fig.3 below.

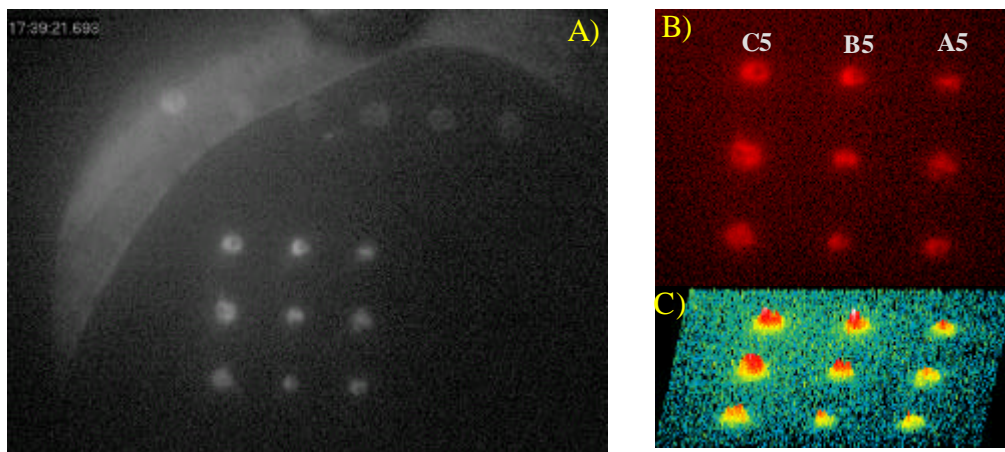


Figure 3: SPM image of the array after hybridizing with 50nM target(A), false color representation(B) and intensity profile(C) of the same image.

If we take a line scan in order to quantify the intensity on the array as shown in Fig.4, we can see a small difference in the grey levels. On the other hand, if we take the region measurements (averaged values) as defined by the spot area in Fig.5, the intensity values shows the difference more clearly in numbers.

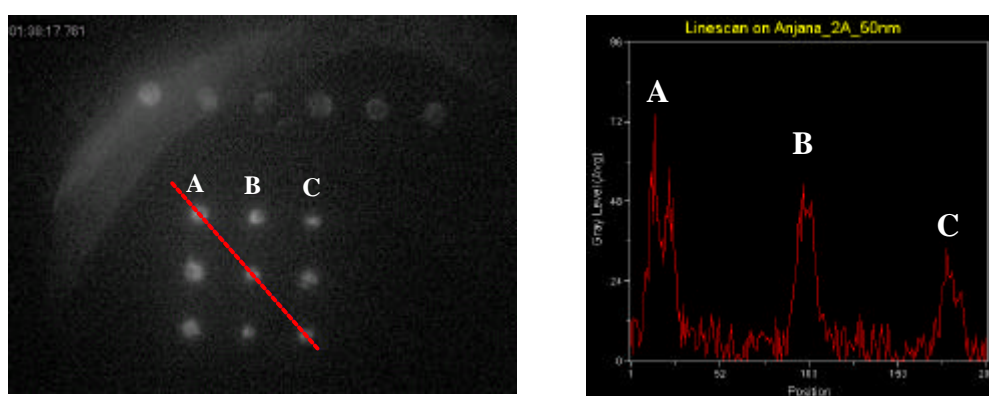
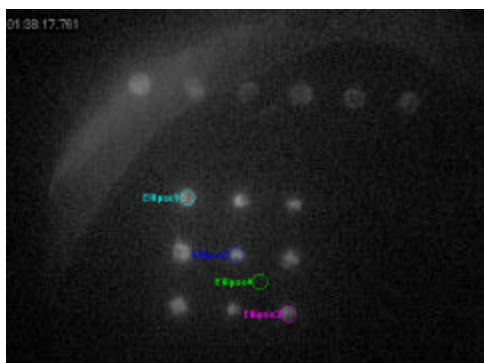


Figure 4: Line scan on A) C5, B) B5 and C) A5 row.



Region	Area(pixel)	Integrated Intensity (grayscale level)
Ellipse1-A	401	15665
Ellipse2-B	401	10581
Ellipse3-C	401	6283
Ellipse4-background	401	1619

Figure 5: Region measurement of the spots on array after rinsing

If we do the same measurements to array 3A whose SPM image is shown in Fig.6 below, we can also hardly see a difference between three modified PNAs in the line scan after hybridization with 50nM target (Fig.7). It definitely gives difference when two columns are compared with C4 column.

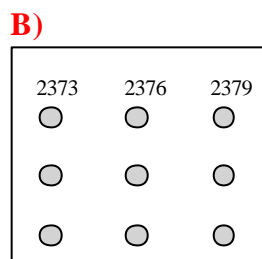
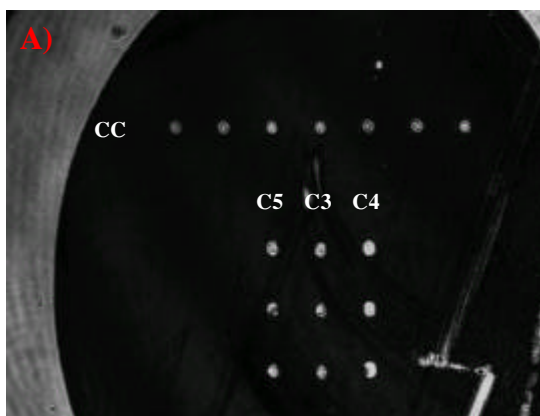
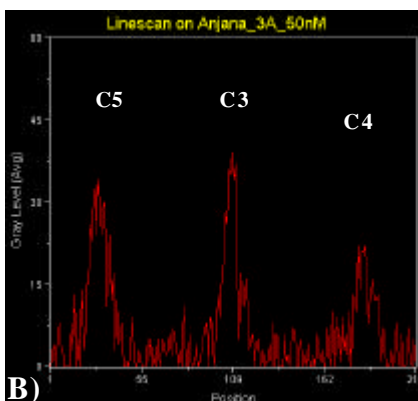
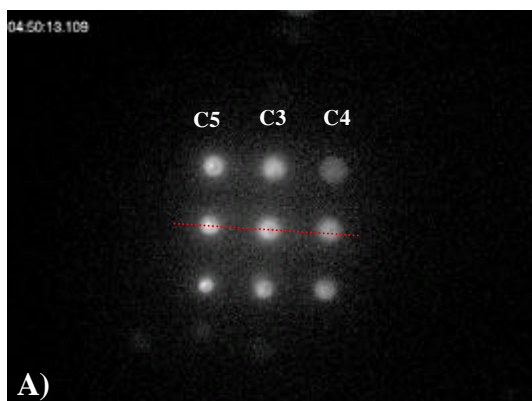
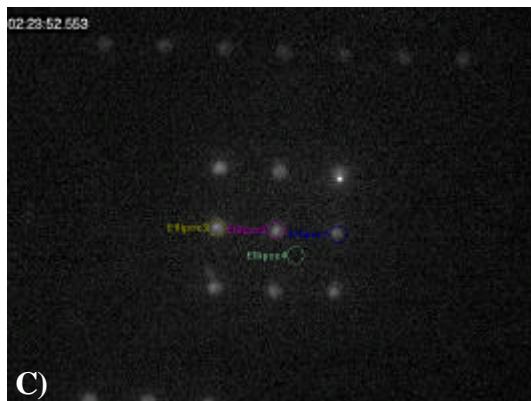


Figure 6: A) SPM image of array, A) in air and B) cartoon drawing of the array





Elapsed Time	Region Label	Area (pixel)	Integrated Intensity (grayscale level)
2:23:52,6	Ellipse1-C4	424	4143
2:23:52,6	Ellipse2-C3	424	6140
2:23:52,6	Ellipse3-C5	424	7368
2:23:52,6	Ellipse4-background	424	1361

Figure 7: A) Line scan image and B) lines scan plot of array after hybridized with 50nM target and rinsed with buffer C) image and region measurement values after overnight rinsing

The images could also be captured during the hybridization process in order to observe the kinetic behavior of the binding. The integrated intensity values for each PNA which was measured from a time lapse image series during the hybridization and dehybridization processes is shown in Fig.8 and zoomed in version in Fig.9. If we fit the data with a Langmuir model, we can obtain the affinity constants for each PNA.

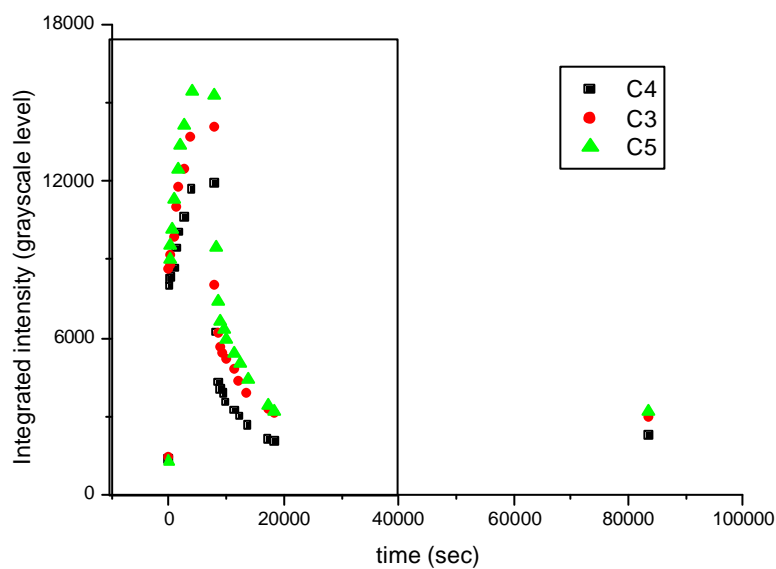


Figure 8: Integrated intensity vs. time plotted for each PNA

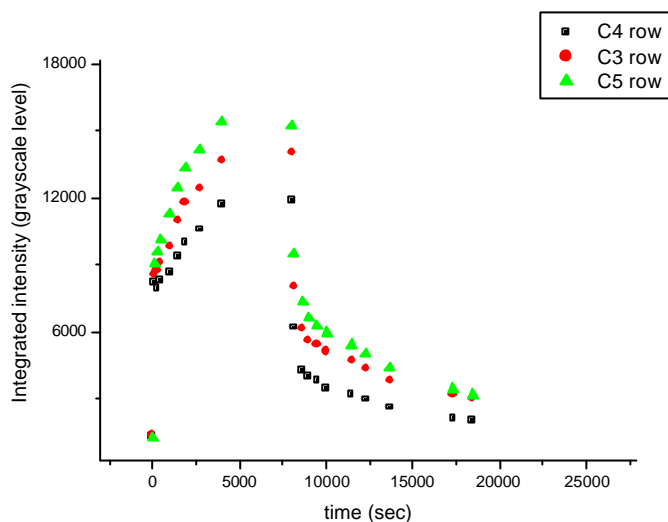


Figure 9: Zoomed-in plot of Fig.8, Integrated intensity vs. time plotted for three different PNAs.

For example if we fit the curve for C3 which refers to PNA2376 (Fig.10), the values that was found from SPFM data differs at least by one order of magnitude compared to results obtained from SPFS. The main difference comes from the dissociation phase. The image that was captured right after rinsing shows a big drop in fluorescence value. There might be two reasons: first, the probe density is not as high as in regular surface matrix that the fluorescence intensity in the association phase is mainly contributed from the unbounded chromophore in the solution. Thus, it is rinsed away after buffer circulation resulting the fluorescence drop. Second reason might be surface roughness. The surface due to spotting is more rough than the regular matrix. Thus, scattered light from the surface contributes to the monitored fluorescence intensity during association phase and it disappears upon rinsing resulting a drop in fluorescence. Thus, the overall fluorescence decrease is more pronounced in the kinetic curve from microscopy.

That could have been overcome by using higher probe concentration in order to get a denser probe layer. However the probes were received from collaborates and having concentrated solution was not possible option during the studies.

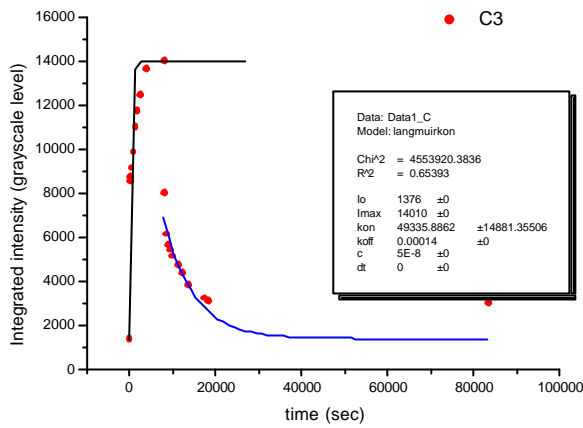


Figure 10: Langmuir fit for C3 column, PNA2376.

Table 2: k_{on} , k_{off} , K_a and K_d results from SPFM and SPFS by Langmuir fitting for PNA2376

PNA2376	$k_{on}(M^{-1}s^{-1})$	$k_{off}(sec^{-1})$	$K_a (M^{-1})$	$K_d (M)$
from SPFM	5×10^4	1.4×10^{-4}	3.5×10^8	2.9×10^{-9}
from SPFS	2.4×10^4	1×10^{-5}	2.4×10^9	4.1×10^{-10}

Another array was prepared with the PNAs 2523, 2361 and 2364. The SPM image in air is shown in Fig.11.

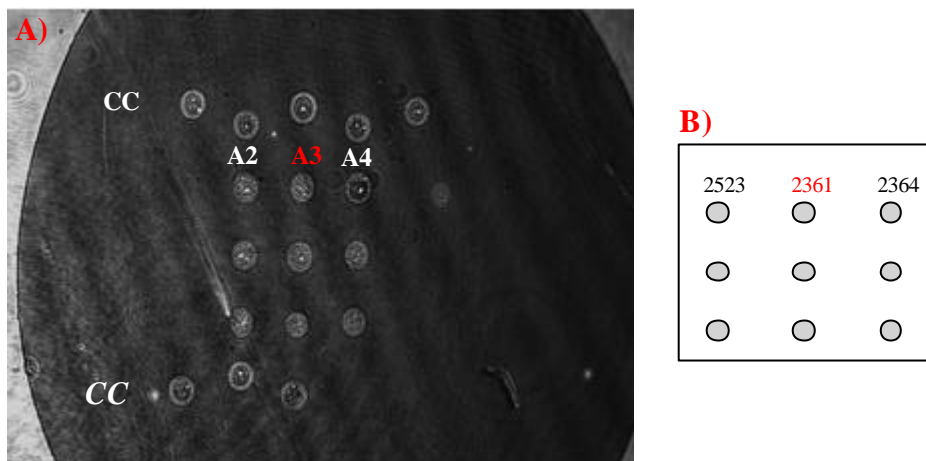


Figure 11: SPM image of array 1A, A) in air and B) cartoon drawing of the array

After injecting a $1\mu M$ target solution the fluorescence image was captured (Fig.12-A). Since we know from SPFS studies that the surface reaches saturation in a short time for such high concentrations, the array rinsed after approximately 2 hrs of

hybridisation. As we can see from Fig.12-C the disassociation process was completed after overnight rinsing and the intensity levels in the line scan decreased (Fig.12-D). The intensity values are also shown in Table3.

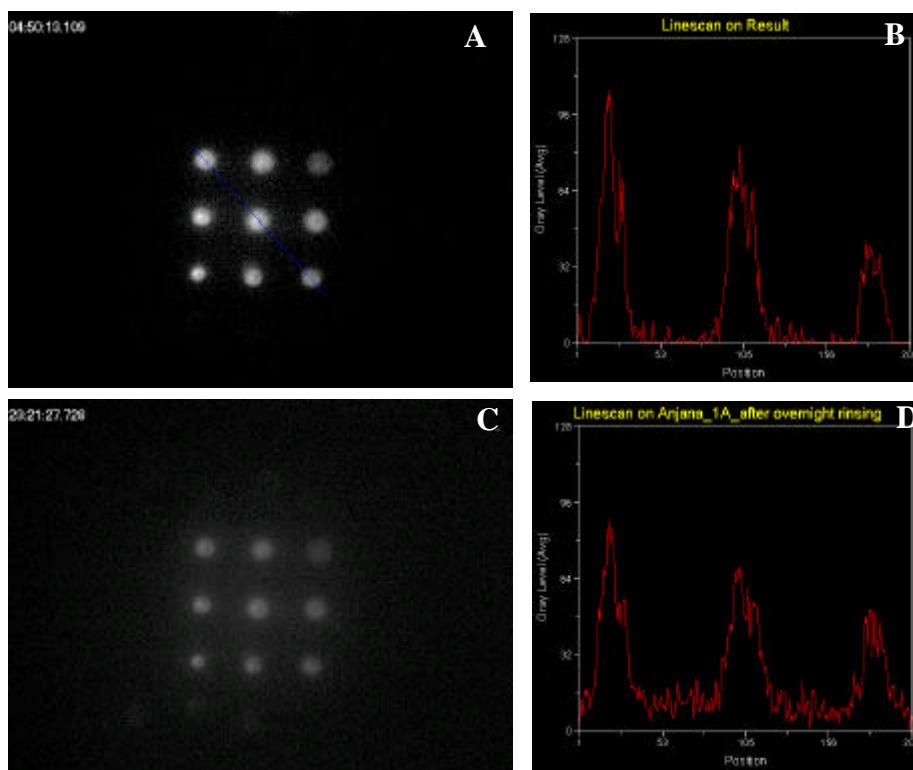


Figure 12: SPFM image of array 1 A) after appr.2 hrs rinsing and B) its line scan, C) after overnight rinsing and D) its linescan

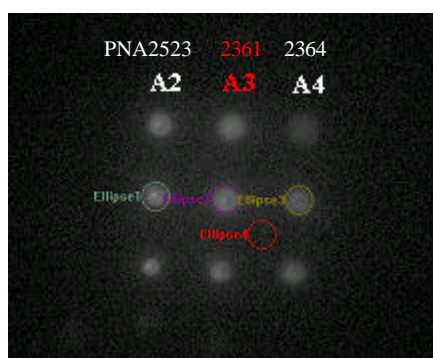


Table 3: Intensity values of selected region in Fig.13

Image Plane	Region Label	Area (pixel)	Integrated Intensity(gray scale level)
rinsed	Ellipse1-A2	791	38175
Rinsed overnight	Ellipse1-A2	791	33420
rinsed	Ellipse2-A3	791	41966
Rinsed overnight	Ellipse2-A3	791	38434
rinsed	Ellipse3-A4	791	26117
Rinsed overnight	Ellipse3-A4	791	25852
	background	791	3557

Figure 13: The averaged region measurements of the spots in each row and values summarized in the table.

As mentioned before, the surface could be regenerated many times and reused. Using the SPFM image, the regeneration process can be observed by eye as it is shown in Fig.14.

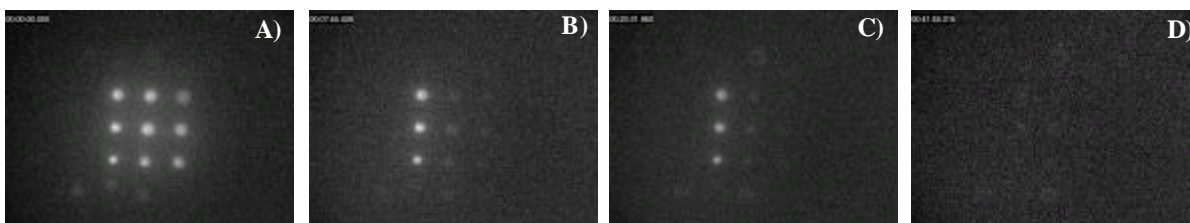


Figure 14: Regeneration of array A)before rinsing, B) 7min after C)23min and D) after 40min. rinsing with $\text{NaOH}_{(aq)}$ and later with buffer

In Fig.15, a 50pM target solution was injected, and after overnight hybridization, the fluorescence image was captured. The intensity levels is the highest in the PNA2523 case followed by PNA2364. This result is expected based on the ΔT_m values. On the other hand, Fig.13 and table 3 show the highest affinity for PNA2361 which is not expected.

In the microscopy, at least we should monitor the half “decorated” probe fluorescence intensity. 50pM target solution (fig.15) was the lowest concentration that could have been observed in a clear array appearance. If we look at the K_a value of the PNAs that were obtained from 4 different measurements in Chp.4.1, the closest K_d value to the 50pM appear from the ones that were obtained by using the saturation values from titration measurement, which are in the range of 90-250pM.

Region name	Elapsed Time (sec)	Area (pixels)	Integrated Intensity (grayscale level)
1-A4	22537	358	5474
2-A3	22537	358	5592
3-A2	22537	358	6274
Background		358	1620



Figure 15: region measurements and SPFM image of the array1A after hybridization with 50pM target.

As mentioned earlier, the main advantage of the microarrays is that more than one probe can be put on the same chip and measured simultaneously. In the following experiment, all the PNAs in Table1 were printed on the same chip surface by using a pin-tool spotter with a 500 μm pitch length.

Fig.16-A shows the SPM image of the array at the resonance angle and Fig.16-B displays the SPFM image of the array before hybridization. The coupling control was used again for focusing.

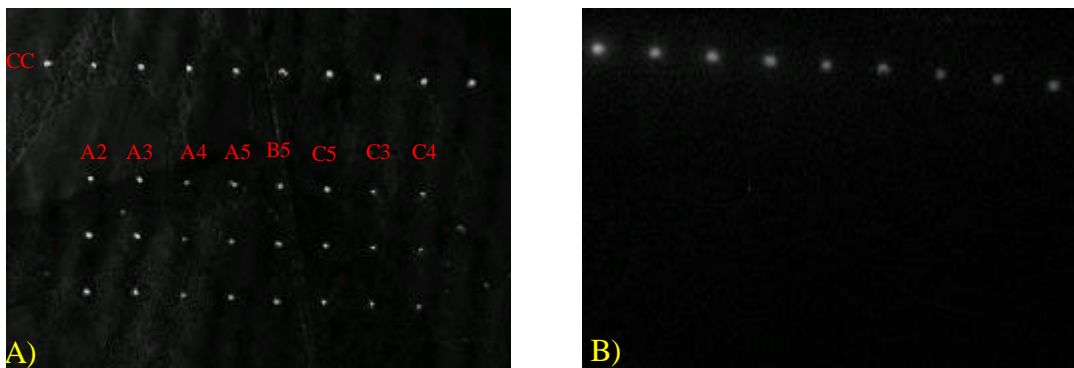


Figure 16: A) SPM image B) SPFM image of the array before hybridization

Fig.17-A shows the SPFM image and Fig.18 the kinetic graph of the array after hybridization with a 50nM target solution. After rinsing with PB buffer, a line scan was evaluated for each column in order to quantify the hybridization as shown in Fig.17-B.

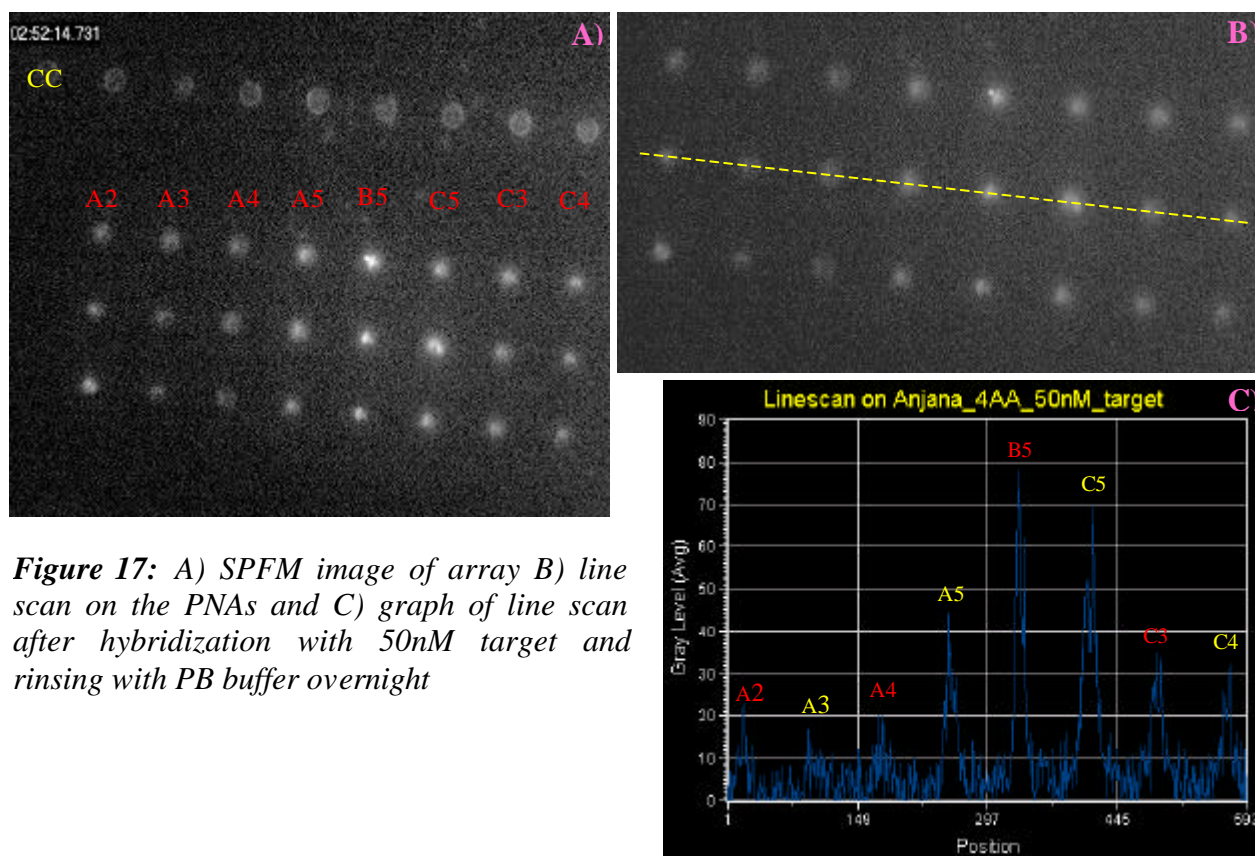


Figure 17: A) SPFM image of array B) line scan on the PNAs and C) graph of line scan after hybridization with 50nM target and rinsing with PB buffer overnight

As it can be seen from Fig.17-C, the intensity levels for the different PNAs are not the same. If we follow the line scan level in terms of gray value after overnight rinsing, the intensity levels have order as following; B5>C5>A5>C3>C4>A2>A4>A3 which refers to PNA2370>2373>2367>2376>2379>2523>2364>**2361**.

As we have also seen from the SPFS result, there is no clear differentiation in the affinities of the PNAs. However all have higher fluorescence intensity than unmodified PNA (2361).

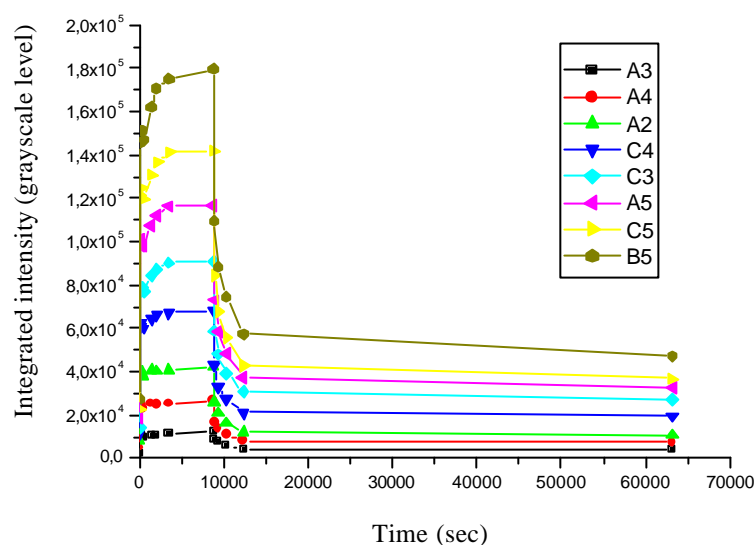


Figure 18: Graph of integrated intensity vs. time for all PNAs (Including PNA2523)

Reproducibly, we observed a big drop on fluorescence value upon rinsing in the kinetic measurement as mentioned before. Thus, the K_a value obtained from Langmuir fitting will not be as accurate as we obtained from SPFS measurement. If we obtain the K_a values for each PNA, we can see that SPFM results confirm the results that we got at the end of SPFS measurements which was indicating that there is no systematic difference in the affinity constants has been observed and the values that were obtained from two methods at the end varies in the range of an order of magnitude. Additionally, it can be also seen in Fig.19 that the K_a obtained from SPFM results does not follow the increase in ΔT_m . While PNA2370 is supposed to show the highest K_a value, it shows the lowest value obtained from SPFM results.

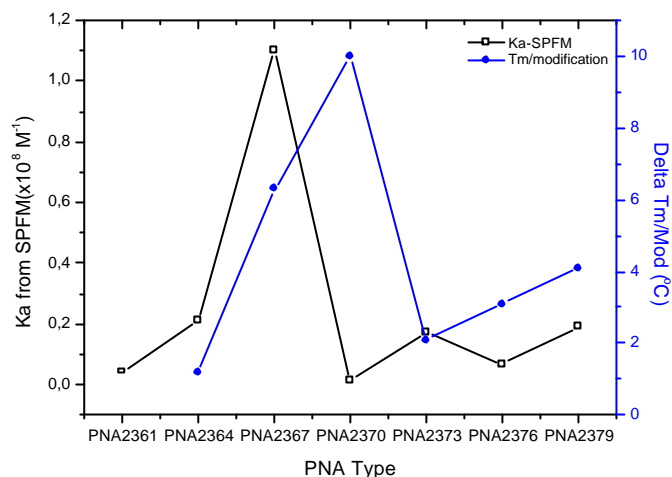


Figure 19: Plot of K_a values obtained from single kinetic measurement with SPFM technique vs. ΔT_m values each PNA (PNA2523 excluded).

And another fact in terms of the sensitivity rises from the results. As it was mentioned before, the min. concentration that could have been observed in SPFM for this study was 50pm while that value was a couple of pM in SFPS measurements. That clearly shows that the SPFS technique is more sensitive than SPFM.

As it was performed in SPFS measurement, the affinity constant was also obtained from titration measurement. The titration experiment was performed with the concentrations starting from 200pM up to 100nM. As we see in Fig.20, the surface started to be “decorated” with an increasing concentrations. After each concentration, the saturated fluorescence value was obtained and plotted against concentration (Fig.21-A). The Langmuir isotherm was also linearized (Fig.21-B). Thus, the affinity constants for each PNA was obtained as it was also performed in the same way in SPFS data.

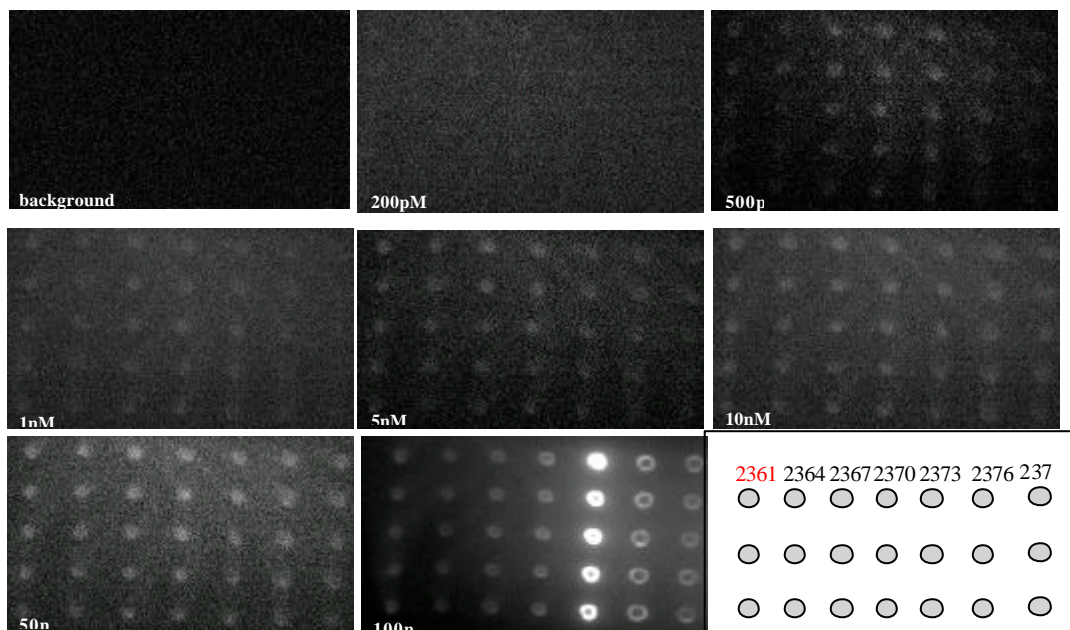
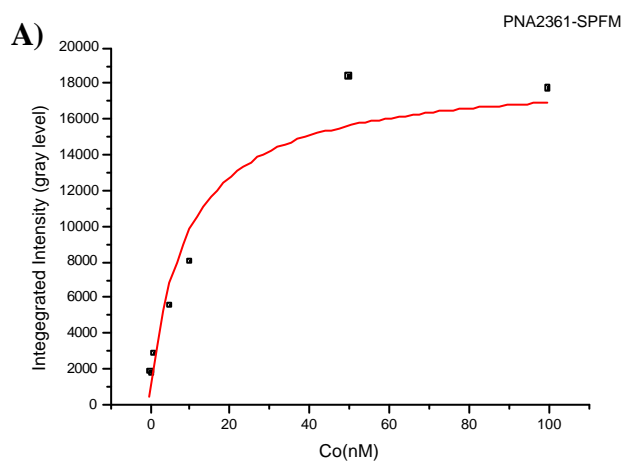


Figure 20: SPFM images of the titration starting from 200pM to 100nM SPFM.



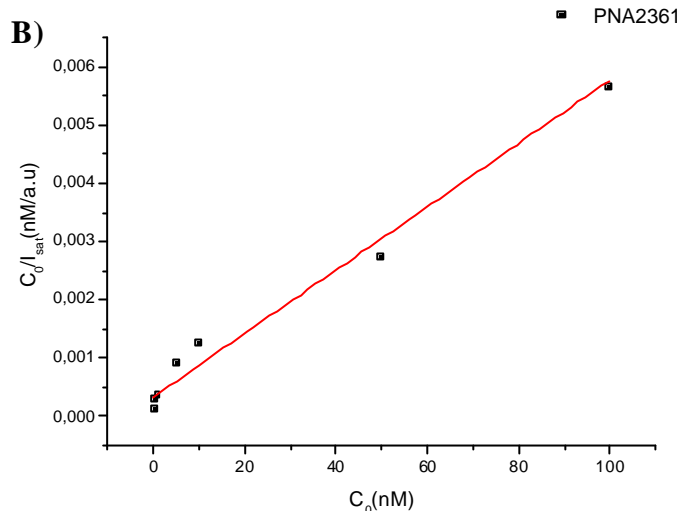


Figure 21: A) Langmuir Isotherm and B) linearized Langmuir isotherm of PNA2361 from titration measurement with SPFM

Table 4 summarizes all K_a values obtained from SPFM titration measurements and lists the K_a values obtained from single kinetic and titration measurement. In Fig.22 these values are plotted for the different PNAs. Fig.23 compares the values with ΔT_m values. Both cases do not show any correlation. Additionally, the K_a values from titration measurement are higher than the respective values of single kinetics but still smaller than that of SPFS experiments (Fig.24). However we should mention that even though the affinity constants do not follow the trend in ΔT_m increase cases, the K_a values in most cases are higher than the value of unmodified PNA.

Table 4: Affinity constant and half saturation value obtained from single kinetic and titration measurement by SPFM for all PNAs

PNA name	<u>From single kinetic</u>		<u>From saturation value (Isat)</u>	
	K_a (M^{-1})	K_d (M)	K_a (M^{-1})	K_d (M)
2361	4.3×10^6	2.3×10^{-7}	1.1×10^8	9.1×10^{-9}
2364	2.1×10^7	4.8×10^{-8}	1.1×10^8	9.1×10^{-9}
2367	1.1×10^8	9.1×10^{-9}	6.1×10^7	1.6×10^{-8}
2370	1.3×10^6	7.7×10^{-7}	3.6×10^7	9.1×10^{-9}
2373	1.7×10^7	5.9×10^{-8}	4.5×10^7	2.2×10^{-8}
2376	6.9×10^6	1.5×10^{-7}	6.6×10^7	1.5×10^{-8}
2379	1.9×10^7	5.3×10^{-8}	3.5×10^7	2.9×10^{-8}

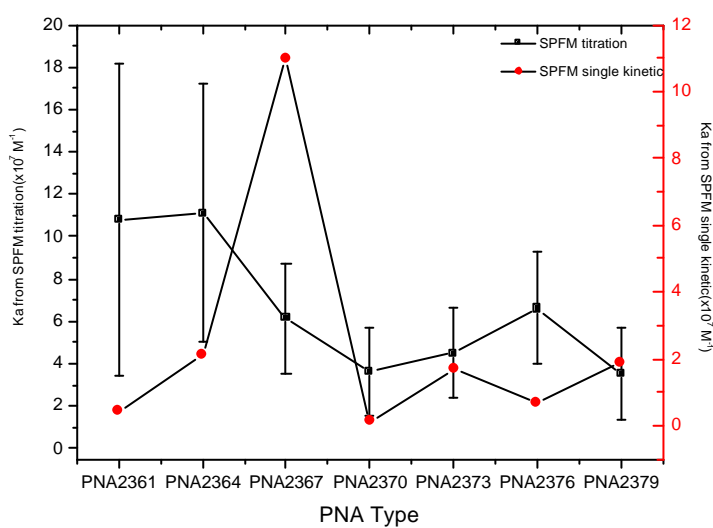


Figure 22: K_a values obtained from titration measurement and single kinetic measurements with SPFM for each PNA.

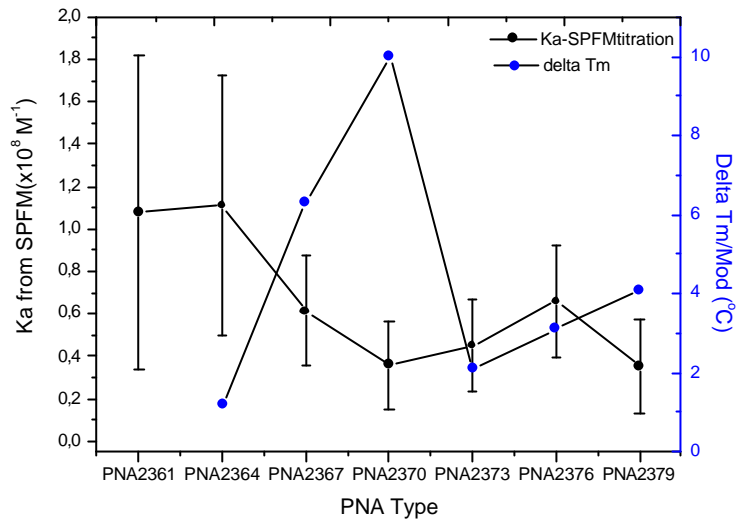


Figure 23: *Ka* values obtained from titration measurement with SPFM technique vs. *DTm* values for each PNA.

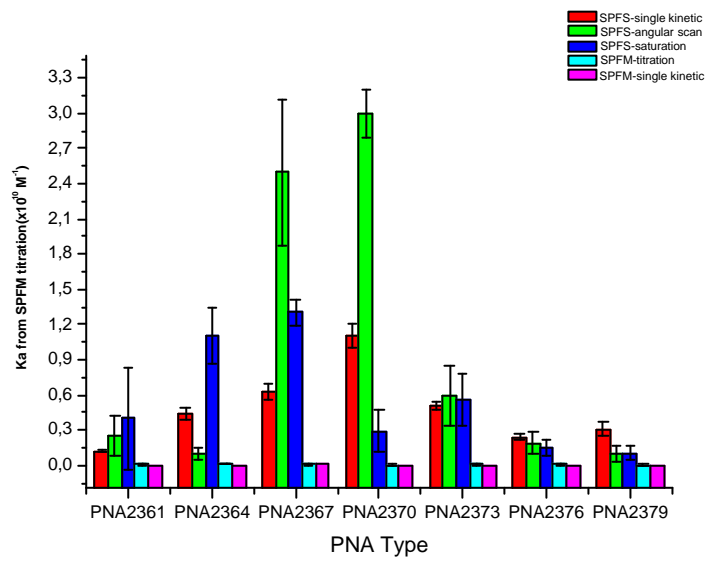


Figure 24: Comparison of the *Ka* values obtained from SPFM and SPFS techniques for each PNA.

4.3 Conclusions

The hybridization process of different PNAs with different affinities to the same target were investigated using SPFS and SPFM techniques on a planar surface and on an array platform respectively. The affinity constants of each PNA were obtained by fitting the single kinetic measurements, titration measurements (both for SPFM and SPFS) and by global analysis (for SPFS) datasets according to the Langmuir model. From each measurement, K_a was obtained. The values obtained from different approaches were compared in-between and to values of the melting temperature difference upon modification. No clear correlation between the K_a values was found. The K_a values from SPFM experiments show approximately an order of magnitude difference when compared with those obtained from SPFS. Even when using the same technique, either SPFS or SPFM, different affinity constants for the same PNA were found from different analysis approaches. The k_{off} rates of PNA 2376 is 1.4×10^{-4} for SPFM and 1×10^{-5} for SPFS measurements (table 2). We believe that faster k_{off} rate is an artifact due to the relatively long integration time needed for image recording (ca. 30 sec.). This case has been also observed in the previous studies of Lieberman et al (2003). The limited stability of the Cy5 fluorescence dye results in a substantial loss of the fluorescence due to photobleaching of the chromophores. For the k_{on} process this is less pronounced because the target molecules are continuously exchanged from solution. There is also no correlation between ΔT_m and the K_a values. The SPFM technique is limited by sensitivity of the CCD and also facing with fluorescence lost due to long exposure times during the image capture. As a fact of the detection limit for SPFS is about a few pM while we are not able to detect those concentration values with SPFM. Hence, the values that we obtained from SPFS measurements are more reliable compared to those from SPFM. However, SPFM is more suitable when a quick yes/no answer or a relative comparison is needed.

As it has been observed very often during the measurements that, when the target was injected for as a first time after the probe immobilization, there was always some problem monitoring the hybridization. However, when same measurement was repeated after 1st regeneration, the fluorescence signal was able to be monitored smoothly. This might indicate that the probes on the surface might rearranges itself in time.

There were also no correlation observed between with ΔT_m values and the affinity constants. ΔT_m values were measured by collaborators and they represent the stability increase of the duplex PNA-DNA in solution. Since our technique is a surface sensitive technique, the conformational change upon surface-immobilization might effect the kinetic behavior of the PNAs resulting in the deviation in K_a values.

Additionally, as it was also mentioned earlier that the sharp decrease in the fluorescence intensity upon rinsing as result of either low probe density or surface roughness effects the dissociation curve. Thus, it gets very difficult to obtain a meaningful K_a value out of a single kinetic measurement by SPFM.

5. Genetically Modified Organism (GMO) detection in food chain by means of DNA-DNA and PNA-DNA Hybridization by Surface Plasmon Fluorescence Spectroscopy (SPFM)

5.1 DNA-DNA Hybridization on a Biotin / Streptavidin Matrix

5.1.1 Aim

The presence of ingredients derived from GMOs in food production, in the market is subject to number of European Regulations that stipulate which product consisting of or containing GMO-derived ingredients should be labeled. In recent incidence, according to reports [E.Kok et al,2002] where unapproved GMO varieties entered to EU market played driving force role to develop more powerful tool for GMO detection and identification in the food chain in order to maintain this labeling requirements.

Our studies are very relevant since our approach can offer a sensitive method for real-time analysis both a labelled and a non-labelled platform on an array bases. The EU project (*DNA-Track, OLK1-2000-01658*) has the aim to detect GMO contents in the food chain based on the DNA and PNA array technology. The collaborators are listed in Appendix A. The limit for labelling which is 1% GMO content was the ultimate aim of GMO detection in the food chain project and

This part of the study involves GMO detection based on a regular streptavidin matrix as described in section. 3.2.1 and 3.2.2 by using a DNA probe and a DNA target with 1 or 2 mismatches on the backbone.

The oligonucleotides that have been used as model system for spotting are shown in Table 1. The biotinylated probes were obtained from MWG, Germany. The total lengths of the probes are 30 bases with a 15mer T spacer and a specific 15mer recognition sequence. The mismatches (MM) are placed in the middle of the recognition sequence on the G base. For detection of GMOs, 2 kinds of amplicons were prepared by polymerase chain reaction (PCR) method from natural soybean (SL) and from genetically modified round-up ready soybean (RR) for detection of GMO.

Table 1: DNA probes and targets sequences

P1 probe 30	5'-Biotin -T15 TGT AC <u>G</u> TCA CAA CTA -3'
P2 probe 30	5'-Biotin -T15 TGT ACA TCA CAA CTA -3'
P3 probe 30	5'-Biotin -T15 TGT AC <u>G</u> <u>TGA</u> CAA CTA -3'
T1 target 15	5'- Cy5 -TAG TTG TGA <u>CGT</u> ACA -3'
T2 target 15	5'- Cy5 -TAG TTG TGA TGT ACA -3'
T3 target 15	5'- Cy5 -TAG TTG <u>TCA</u> <u>CGT</u> ACA -3'
Mu196bp	CGGCGGTACACTACCTATAGACGTCTTAAGCGGGAACCCCGGGTCGGCCGGTTAC TTGGTGGCTCCCCTGGCTCCCGGACATGTAGTGTGATTGAAGATGCACGGACCTA GGCGCACCCTGGCTCTAGAGGGCCCTAGGTTCCCGCTTAAGGTCGTGTGACCGCC GGCAATGATCACCTAGGCTCGAGCCATG
RR 125bp	CATTTTCATTTGGAGAGGACACGCTGACAAAGCTGACTCTAGCAGATCTTTCAAAGAATGGC ACAAAATTAACAACATGGCACAAAGGGATACAAACCCTTAATCCC AATTCCAATTTCCATA AAACCCCA

A 3x3 array has been prepared by using an ink-jet spotter under the same conditions as described before. After giving enough time for the probes to react with the surface, the sample was placed into sample holder and the SPM image was captured in air.

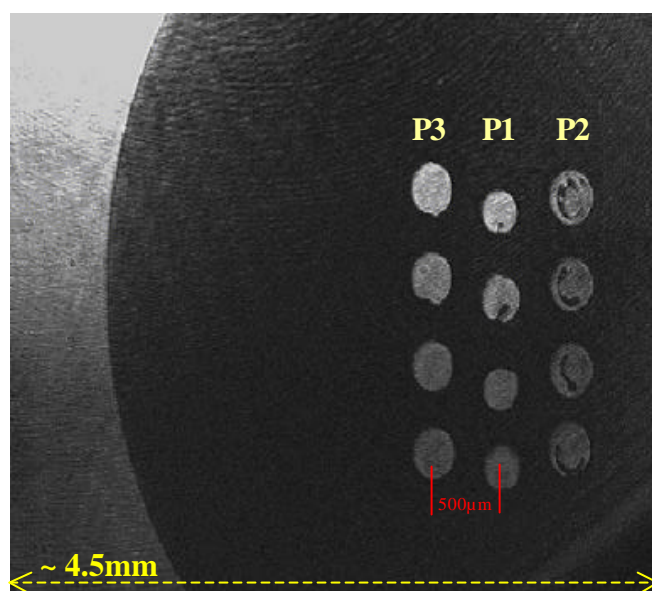
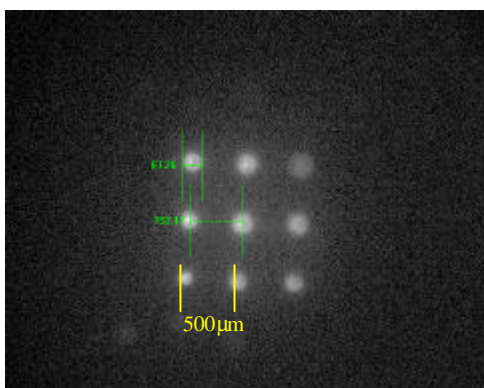


Figure 1: SPM image of DNA P1, P2,P3 probes in air- (no target injected)

The spot size was analyzed using software option “calipers”. Since we know the pitch length of the spot from the spotting parameters, we can calibrate the distance between two spots and calculate the spot.



$$\text{Spot size} = (61.26/152.1) \times 500 \mu\text{m} \cong 200 \mu\text{m}$$

Figure 2: Calibrated spot size in the based of pitch length

After pulse rinsing with PBS, a SPR scan was performed in order to define the resonance angle precisely. As a practical trial, the resonance angle (θ_{res}) could be also seen when the goniometer is moving in between the angles 45-65° in solution. After tuning the goniometer to the θ_{res} , firstly, 1µM Cy5 labeled T2 target solution which is fully complementary to P2, MM1 to P1 and MM2 to P3 probes was injected to the flow cell and the hybridization reaction has been observed by capturing SPFM images over time. After approx. 1hr. hybridization time, the sample was rinsed with PBS solution. (Fig.3)

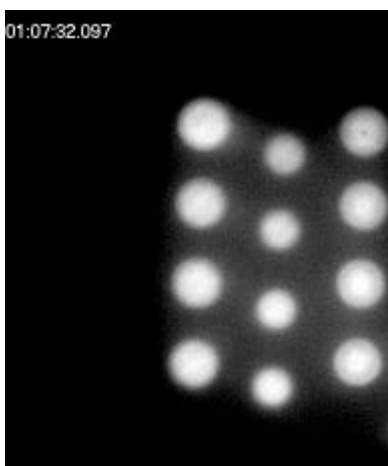


Figure 3: SPFM image of the array after hybridization.

Upon rinsing the dissociation process is triggered and resulted with different intensity levels in MMs as seen in Fig.4. The quantification of the array has been obtained by line scans of the different probe columns. (Fig.5,6,7)

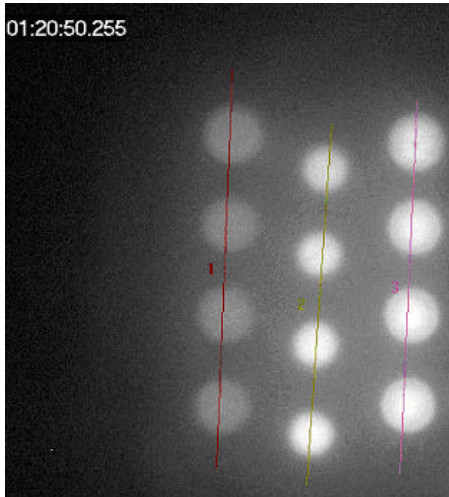


Figure 4: SPFM picture of the array hybridized with $1\mu\text{M}$ T2 target and 13min. after rinsing with PBS.

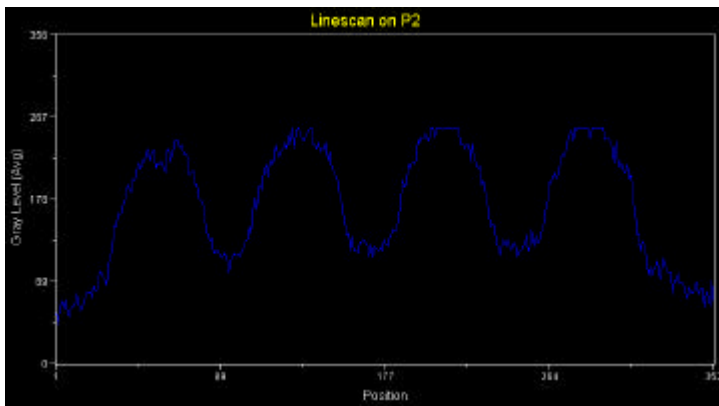


Figure 5: Line scan of P2 row, which is MM0 for T2 target

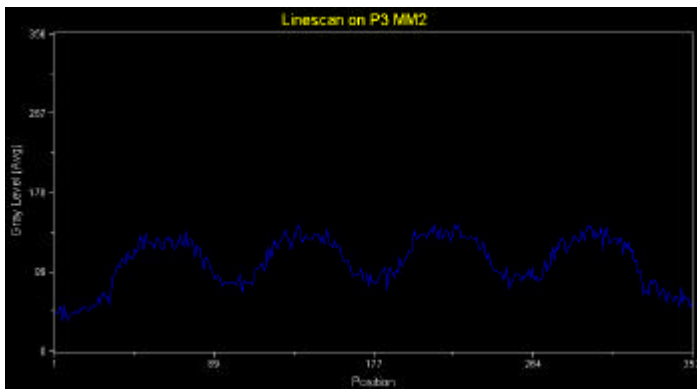


Figure 6: Line scan of P1 row, which is MM1 for T2 target

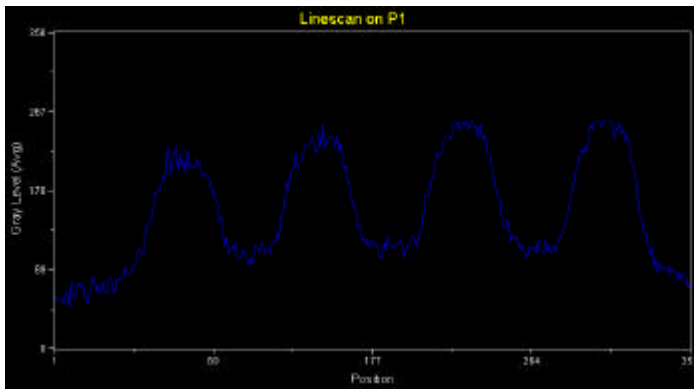
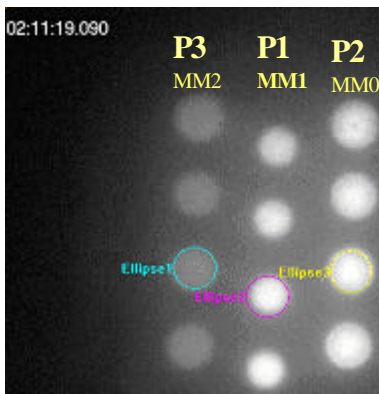


Figure 7: Line scan of P1 row, which is MM1 for T2 target



Region Label	Area (pixels)	Integrated Intensity (grayscale level)
Ellipse1	1530	145434
Ellipse2	1530	301512
Ellipse3	1530	342994

Figure 8: Integrated intensity measurement for selected region for P1, P2 and P3

From Fig.8, we can see that the MM0 spot has the highest intensity. The MM1 intensity is almost double of the MM2 intensity. After prolonged rinsing, the unstable target will be washed away. More specifically, higher disassociation will occur first in the MM2 column, then in the MM1 column.

As it was motioned before, the regeneration process can be observed visually in SPFM as an example is shown in Fig.9. If the surface is regenerated with 10mM NaOH, one can see that the fluorescence is washed from the surface. It is also necessary to wash away the any trace of NaOH solution. Hence, rinsing with buffer long time with an open loop is highly advised.

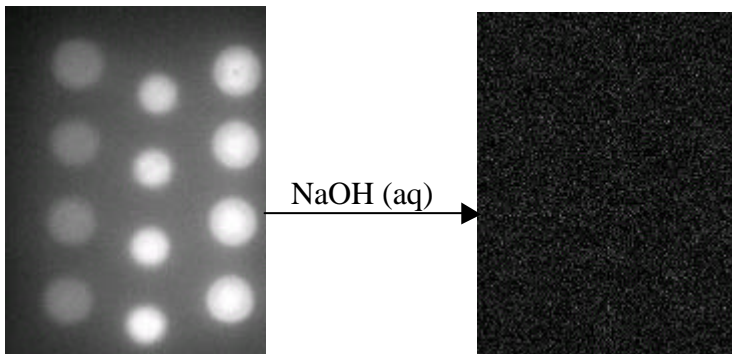


Figure 9: Regeneration of a P1,P2,P3 array after hybridization with a T2 target.

After regeneration of the surface, $1\mu\text{M}$ of T3 target solution was injected to the flow cell. As can be seen in Fig.10, since target T3 is fully complementary to the probe P3, the highest signal appears in the P3 row. MM1 case is P1 probe and MM2 is P2 probe as it could be also distinguished from the line scans (figs.11,12 and 13)

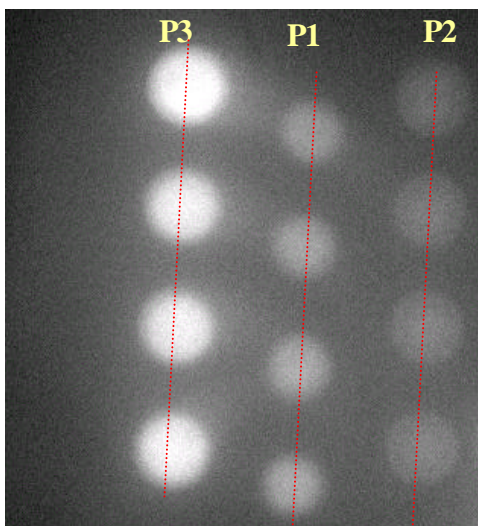


Figure 10: SPM picture of the array after hybridized with $1\mu\text{M}$ T3

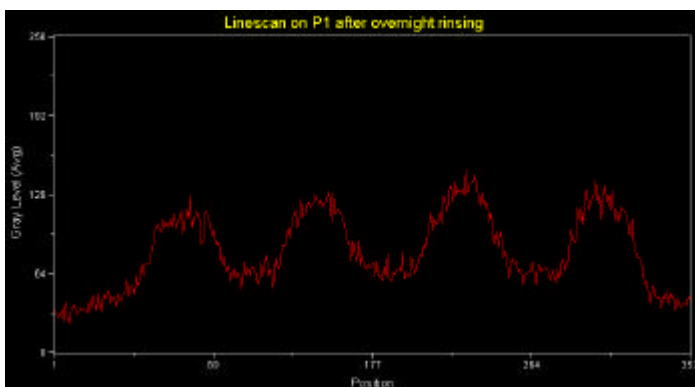


Figure 11: Line scan of P1 row, which is MM2 for T3 target

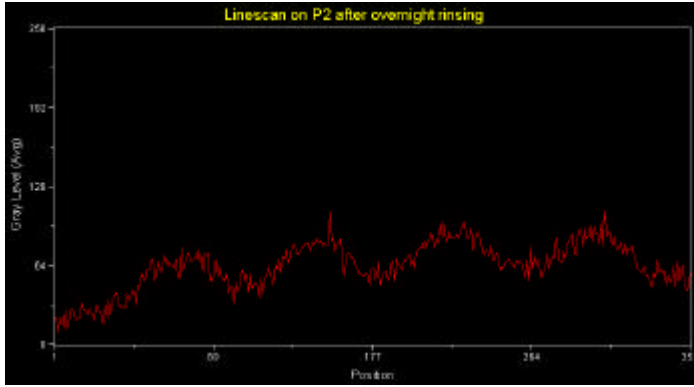


Figure 12: Line scan of P2 row, which is MM1 for T3 target

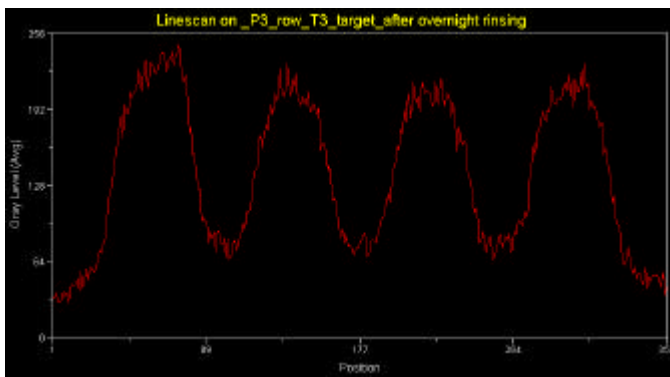


Figure 13: Line scan of P3 row, which is MM0 for T3 target

If we again regenerate the surface and inject the T1 target, a difference between MM1 and MM2 only can be observed (Fig.14a) after longer rinsing. As it can be seen from figures 14b,14c and 14d below, when we started to rinse first the intensity levels looks like quite similar, also the intensity values from table 2 are close to each other. But then we rinsed one more hour, the target in unstable mismatch cases gets ribbed off from surface and after overnight rinsing the MM2 case almost disappears and MM1 is also almost invisible. We could see the integrated intensity values for the images a,b,c and d for the P1,P2 and P3 rows in the Table2. It should be mentioned that the intensity values are the average value of the 4 spots in the each columns even though it was just showed one region in the Fig.15.

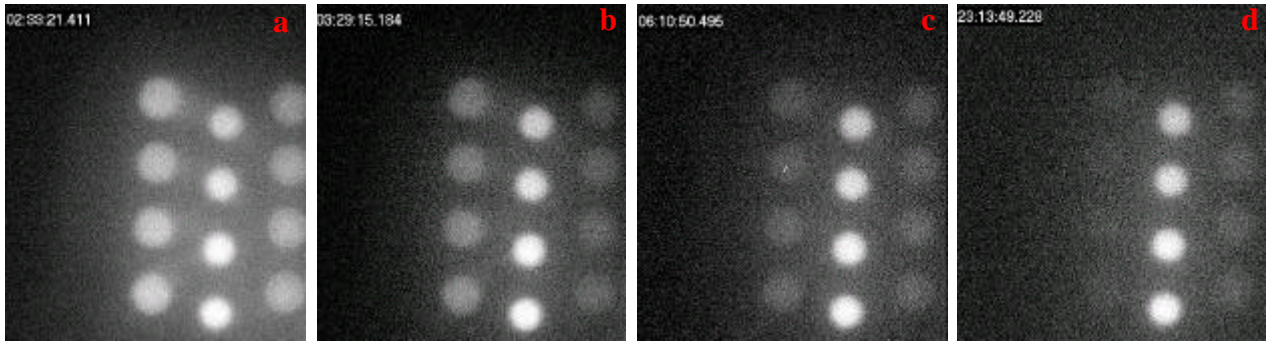


Figure 14: series of images captured during rinsing after hybridisation with T1 target

Table2: Region measurement of each PNAs

Image Plane	Region Label	Area (pixels)	Average Integrated Intensity (Grey level)
a	Ellipse1-P3	1293	61242
b	Ellipse1	1293	27611
c	Ellipse1	1293	15065
d	Ellipse1	1293	11135
a	Ellipse2-P1	1293	76029
c	Ellipse2	1293	54532
c	Ellipse2	1293	48301
d	Ellipse2	1293	41755
a	Ellipse3-P2	1293	52498
b	Ellipse3	1293	18134
c	Ellipse3	1293	15299
d	Ellipse3	1293	13438
	Ellipse4-background	1293	4453

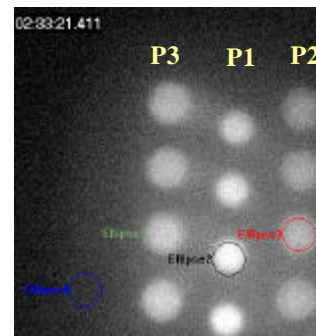


Figure 15: Average integrated intensity values of each PNA probe

The association and disassociation process using a lower target concentration can be observed in the fig.16 below. There is a significant bulk drop when rinsing starts, as seen in the precious chapter. Thus, the Langmuir fitting wasn't performed since a meaningful K_a value cannot be obtain from the curves in Fig.16.

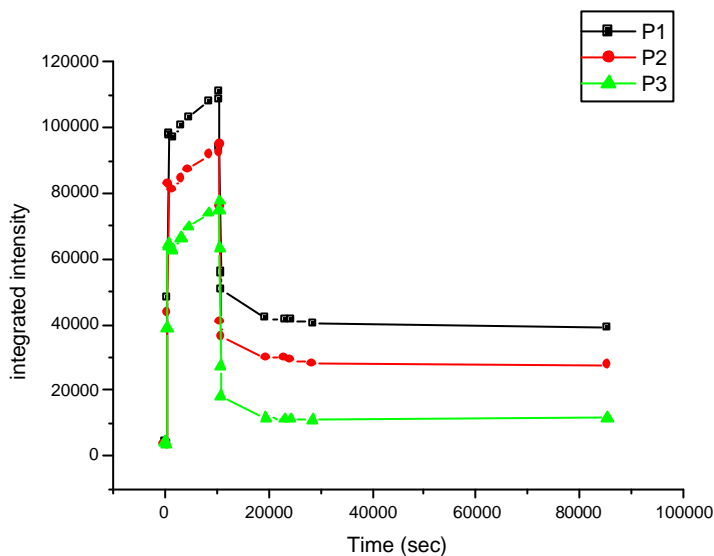


Figure 16: Langmuir isotherm of P1(MM0),P2(MM1) and P3(MM2) probes after hybridisation with 100nM T1 target.

The homogeneity of the spots is also important for the quantification purposes. We do statistics about spot-to-spot variation; we can see from the Table 3 that the spots are quite homogenous although this is not always the usual case. The spot size strongly dependent on the humidity during the spotting and probe concentration but most of the probes are commercially supplied or received from the collaborators, it's difficult to get samples in very high concentrations as it was also mentioned earlier.

Table 3: Spot-to-spot variation

Spot Label	Average Intensity	Intensity Standard Dev	Intensity Signal/Noise	Integrated Intensity
	119,016	53,4606	2,22623	293731
	122,252	42,834	2,85409	241326
	126,925	49,1318	2,58335	276315
	125,303	51,7738	2,42019	268649

Beside the differentiation of the MMs, another aim of the project was to investigate, if GMO can be detected on an array base using SPFM. In the following chapter this detection will be also performed by using PNA .

The PCR Mü196 target, which has the recognition sequence for a P2 probe, was used as a model target. It also shows MM1 and MM2 affinity to P1 and P3 probes respectively. 100nM Mü196 was used after a melt & quenching cycle. This cycle opens the double-strand at high temperature. The separated strands are then quenched at 0°C and directly injected into the flow cell. The different affinities (MM0, MM1, MM2) can be clearly detected from Fig.17. The right column corresponds to P2, the middle P1 and the left to P3.

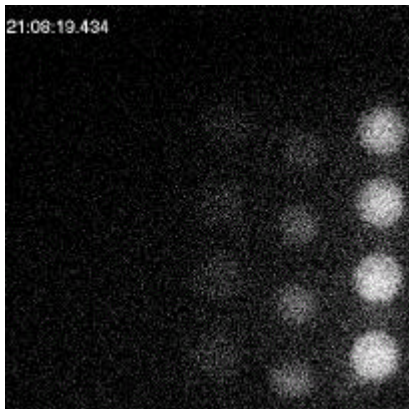


Figure 17: Hybridization with 100nM PCR target Mü196

We now move from model systems to actual DNAs corresponding to GMO relevant system.

The following DNA probes were designed according to the GMO sequences. The array (Fig. 18) of the DNA probes listed in Table 2 was prepared and used for the GMO detection.

Table 4: DNA probes and target sequences

DNA name	Sequence
RR15merMM0 (Mismatch 0)	5'-TTT TTT TTT TTT TTT TGC TAG AGT CAG CTT-3'
RR15merMM1 (Mismatch 1)	5'-TTT TTT TTT TTT TTT TGC TAG AGC CAG CTT-3'
SL15merMM0 (Mismatch 0)	5'-TTT TTT TTT TTT TTT GAT CAA GTC GTC GCT-3'
SL15merMM1 (Mismatch 1)	5'-TTT TTT TTT TTT TTT GAT CAA GTT GTC GCT-3'
Target DNA15mer MM1	Cy5- AAG CTG GCTCTAGCA -3'
GMO RR125	CATTTCAATTTGGAGAGGACACGCTGACAAGCTGACTCTAGCAGATCTTTCAAGAATGGC ACAAATTAACAACATGGCACAAGGGATACAAACCCTTAATCCCAATTCCAATTTCCATA AACCCCA

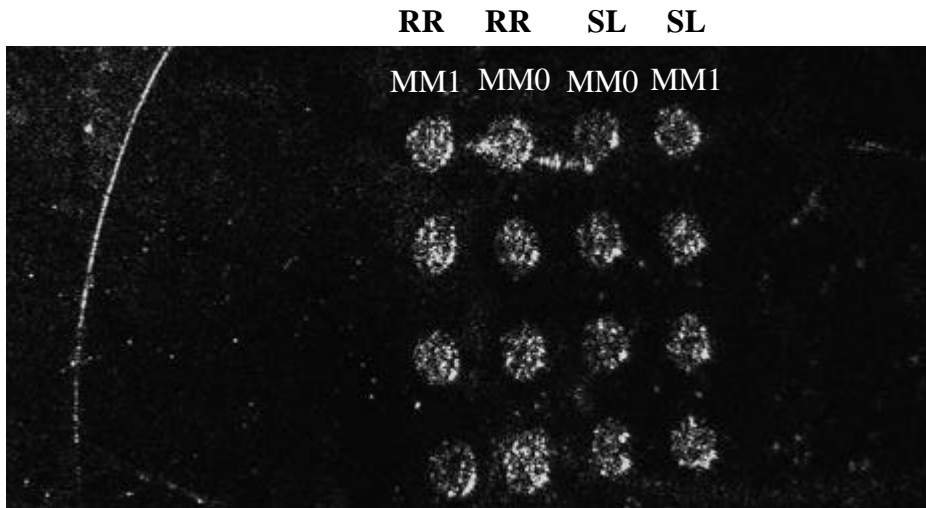


*Figure 18: SPM image of 4*4 DNA array*

The SPM image was captured in air as seen in Fig.18. After rinsing the array with PB buffer, 50nM of Cy5 labelled RR125 PCR target in 450mM NaCl PB buffer was injected into the flow cell after a melting&quenching process. As seen in figure 19, the RR125 GMO target has been specifically bound to the corresponding RR targets following the predicted mismatch behaviours. There is no hybridisation detectable for the SL probes.

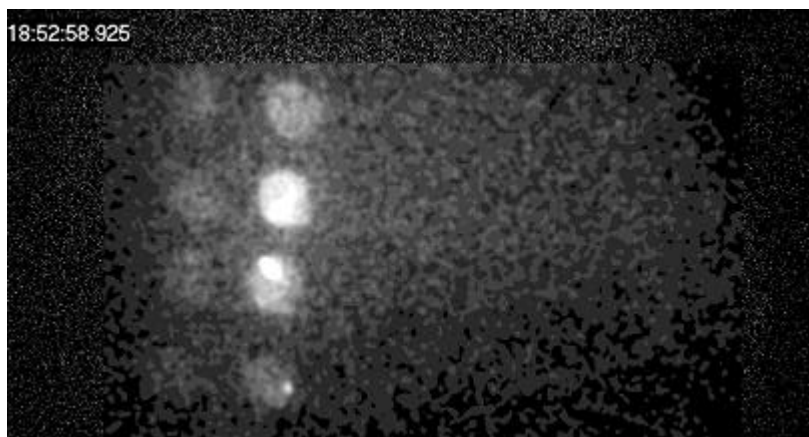


Figure 19: SPFM image of array after hybridisation with RR125 GMO target

5.2 PNA-DNA Hybridization on a SH-Streptavidin Matrix

5.2.1 Aim

As mentioned in the section 5.1, the aim of the study is to detect the GMO content in the food chain by using PNA probes.

Model experiments have been performed to optimise the experimental conditions. First measurements were carried out on SH-Streptavidin matrix to observe the effect of eliminating the thiolation step during the sample preparation.

5.2.2 Materials

The biotinlated probe PNAs were synthesized by the Parma Group (App.A) according to the sequence of the targets with 11, 13, 15mer bases. The oligonucleotides, which were complementary, i.e., fully matched or with a single mismatch had 11, 13 or 15 bases and PCR targets with a Cy5 chromophore, used for the hybridization kinetics. For detection of genetically modified organism(GMO), 5 different amplicons were prepared by polymerase chain reaction (PCR) from natural soybean (SL) or from genetically modified round-up ready soybean (RR). All sequences are shown in Table 1 and 2.

Table 1: Sequences of probe PNAs

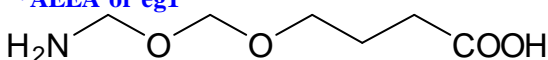
PNAs for Round-up Ready		PNAs for Soy Lectin	
Name	Sequences	Name	Sequences
RR 11mer	BIOT-(AEEA) ₂ - AGAGTCAGCTNH ₂	SL 15mer	BIOT-(AEEA) ₂ -GATCAAGTCGTCGCTNH ₂
RR 13mer	BIOT-(AEEA) ₂ - CTAGAGTCAGCT-NH ₂		
RR 15mer	BIOT-(AEEA) ₂ -TGCTAGAGTCAGCT-NH ₂		
*AEEA or eg1		PNA for Mu	
		Name	Sequences
		P2	BIOT-(EG1) ₉ - TGTACATCACA ACTA-NH ₂

Table 2: Sequences of target DNAs

	Name	Sequences
Oligo-nucleotides	11mer(MM0)	Cy5-5'- AAGCTGACTCT -3'
	11mer(MM1)	Cy5-5'- AAGCTGGCTCT -3'
	13mer(MM0)	Cy5-5'- AAGCTGACTCTAG -3'
	13mer(MM1)	Cy5-5'- AAGCTGGCTCTAG -3'
	15mer(MM0)	Cy5-5'- AAGCTGACTCTAGCA -3'
	15mer(MM1)	Cy5-5'- AAGCTGGCTCTAGCA -3'
PCR	RR 125bp	CATTTTCATTTGGAGAGGACACGCTGACA AAGCTGACTCTAGC AGATCTTTCAAGAATGGC ACAAATTAACAACATGGCACAAGGGATACAAACCCTTAATCCCAATTCCAATTTCCATA AACCCCA
	RR 169bp	ATCCCACTATCCTTCGCAAGACCCTTCCTCTATATAAGGAAGTTCATTTTCATTTGGAGA GGACACGCTGACA AAGCTGACTCTAGC AGATCTTTCAAGAATGGCACAACATTAACAACAT GGCTCAAGGGATACAAACCCTTAATCCCAATTCCAATTTCCATAAACCCCA
	SL 157bp	CCGATGTGTGGATTTGGTGGATCCCAAGAGTTCGGAAAGTGTCAAAC TCAACAGCGAC GACTTGATC ACCAGACTCGTTTTTCGTTGAAAAGACCAAGATAACCTGCATGTGTTTTGTG GCTTAGTGTCAATTGGTGCAGAAAGAAGGCAAGCCCAT
	Mu159bp	CGGCGGTACACTACCTATAGACGTCTTAAGCGGGAATGGTGCGCCTAGGTCCGTGCAT CTTCA ACATGCAGTGTGAT CCGGGAGCCAGGGAGCTCACAAGTATTCCCGCTTAAGG TCGTGTGACCGCCGCAATGATCACCTAGGCTCGAGCCATG
	Mu196bp	CGGCGGTACACTACCTATAGACGTCTTAAGCGGGAACCCCGGGTTCGGCCGGTTA CTTGGTGGCTCCCCGGCTCCCGG ACATGTAGTGTGAT TGAAGATGCACGGACC TAGGGCACCACCTGGCTCTAGAGGGCCCTAGGTTCCCGCTTAAGGTTCGTGTGACC GCCGCAATGATCACCTAGGCTCGAGCCATG

All probes have the same 11mer sequence in their backbone, the 13mer has additionally 2 and the 15 mer has 4 extra bases in their structure.

The array has been printed on a gold slide, which was incubated in SH-terminated Streptavidin overnight. Using SH-Streptavidin can help to reduce the step size of the probe preparation process. The printing conditions were the same as described in the array preparation session in the experimental chapter.

The schematic representation of the array and the fluorescence image are shown in Fig.1-B and Fig 1-A respectively. The fluorescence image shows the background image where no fluorescence target injected. If the target was being started to flow through the sample, it started to bind to the probe on the surface and “decorated” the surface in time.

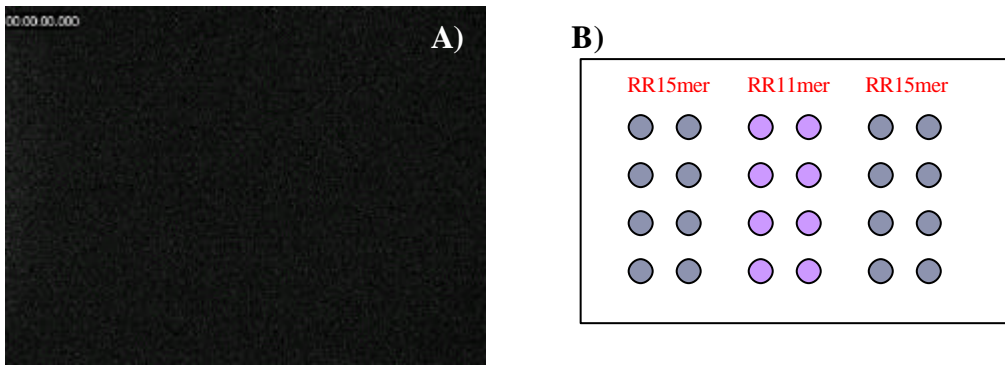


Figure 1: A) SPFM image of the sample before injecting the fluorescence labeled target and B) cartoon representation of the array.

The fluorescence appeared in the areas where the hybridization occurred as seen in Fig.2B. Since the 15mers have also the complementary 11mer bases, the 11mer target also hybridizes with the 15mer PNA probes. The intensity profile of the array is shown Fig.2A and C.

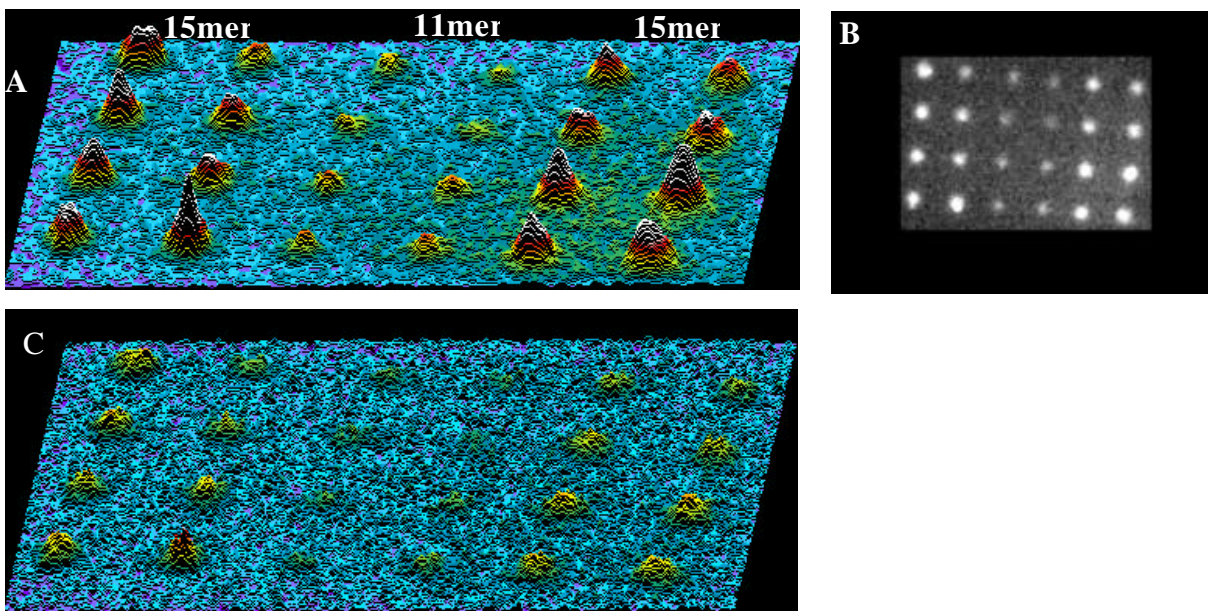


Figure 2: Array of 11 and 15mer PNA after hybridization with 100nM 11merMMO target; first and the last two columns are PNA15mer and two columns are in the middle are 11mer PNA. Image(A) is intensity profile and (B) is the SPFM image after hybridization and C) after overnight rinsing.

The intensity level of each probe was analysed by line scans (fig3-A) after rinsing with phosphate buffer.

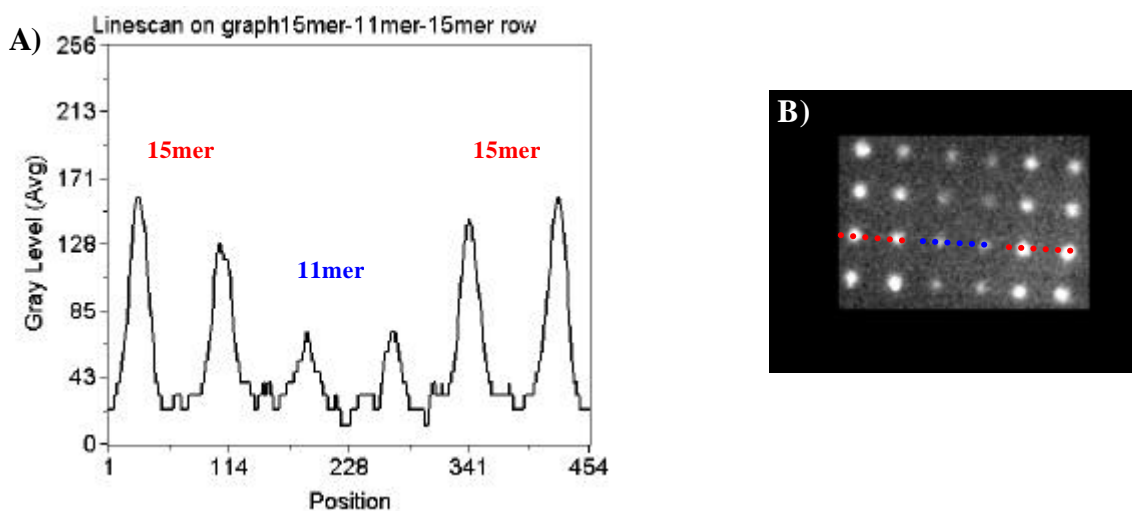


Figure 3: Line scan graph (A) and image (B) on the row of 15mer-11mer-15mer PNA probes after hybridization with 100nM 11mer DNA target.

As it can be seen from the intensity profiles, the intensity level changes after rinsing. This is due to the dehybridization process, k_{off} as a result of rinsing. The interesting part is, that even though the target was fully complementary to the both 11 and 15mer PNA probes, the intensity level in the 15mer row is higher than that of 11mer. That might be the result of having 4 additional bases in 15mer probe's backbone. Since this addition results in a 1.5nm longer (out of total 10-15 nm) chain length, the distance between chromophore and Au layer is increased, resulting in less quenching effect. As it can be seen from the line scans made on 11mer and 15mer probes after hybridization with 100nM of 11mer DNA target, the gray level intensity is almost 2.5x higher in the case of 15mer PNA than that of 11mer.

The intensity of the fluorescence depends on the affinity of the probe to the target. As it can be seen in intensity profiles of the MMO and MM1 cases in Fig.3A and Fig.4C, the fluorescence intensity is higher when the target is fully complementary to the probe. Almost no hybridization can be detected for MM1.

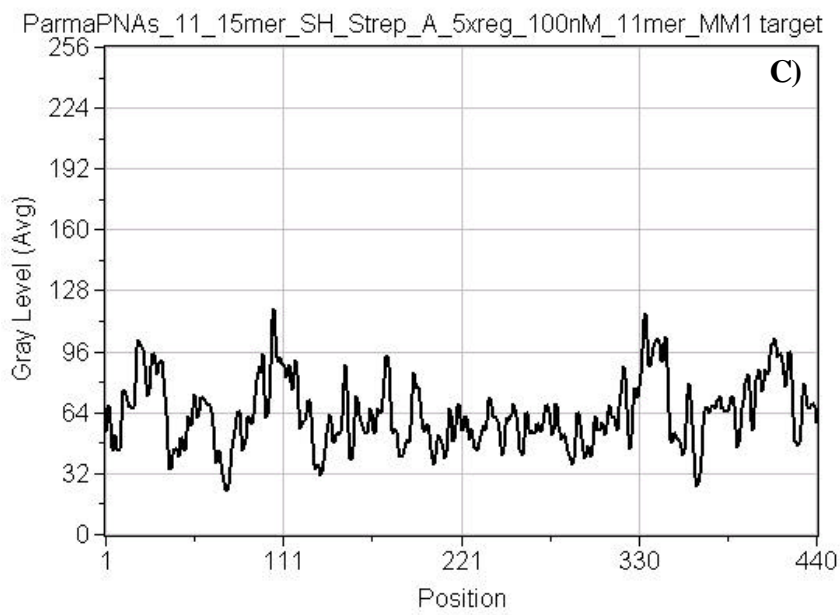
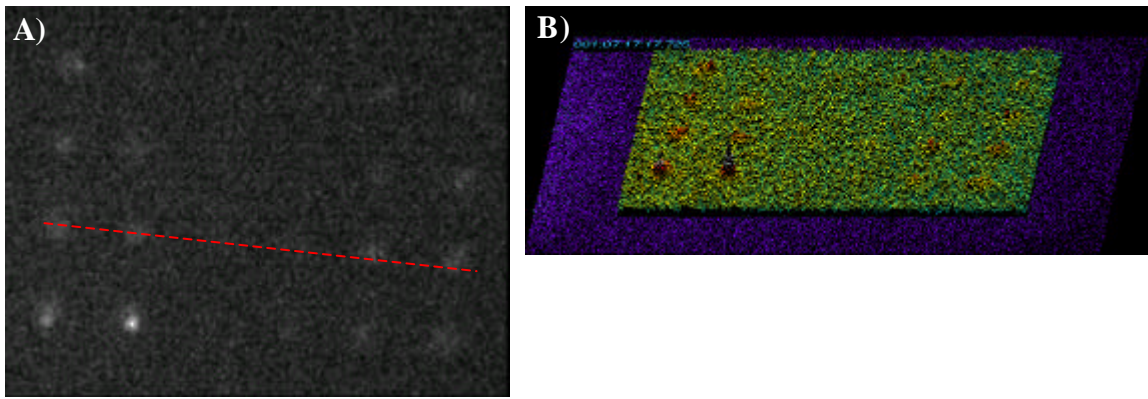


Figure 4: A) The SPFM image and B) intensity profile and C) Line Scan of array after injecting 100nM of 11mer MM1 target onto 5xregenerated surface

Once again the surface could be regenerated by pulse rinsing with NaOH as it can be seen in the image below.

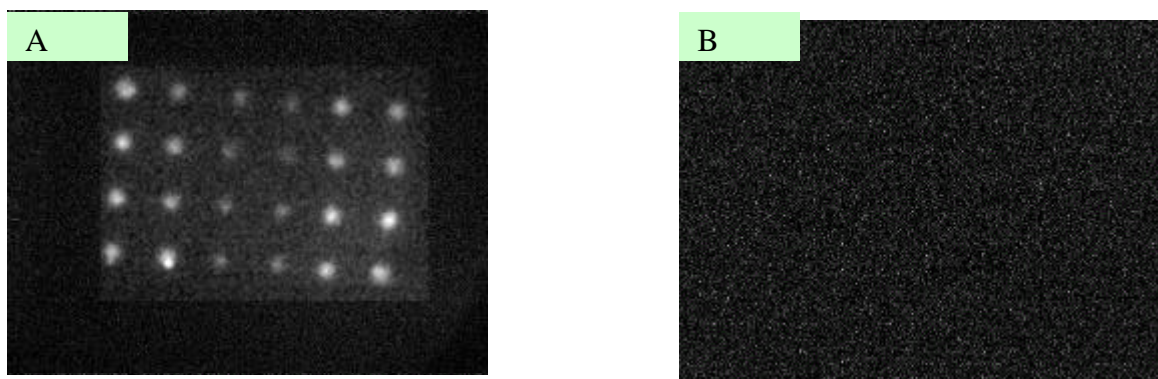


Figure 5: SPFM image of array A) before B) after regeneration

Two different SPFS measurements were performed in order to investigate the importance of the SAM step for the fluorescence measurement in further experiments design. For that purpose a RR11mer PNA probe and a RR15mer MM0 DNA target were used. Both measurements were performed in 10mM phosphate buffer under the same experimental conditions. The first measurement in Fig.6-A shows the measurement with SH-Streptavidin and Fig.6-B with SAM/Streptavidin matrix by using 100nM and 50nM target respectively. When we compare the two measurements, we can easily see that the fluorescence signal differs in the SH-streptavidin case in the rinsing step. Since the rinsing step is independent from the target concentration, the only reason for this result might be quenching of the fluorescence. Once the target solution is replaced with the pure buffer and the dissociation of the targets from their probes leads to a decrease of the measured fluorescence as a function of time by coupling their energy back to the metal layer. Even though a MM0 target was used in both cases, the fluorescence intensity in the SAM matrix case decreases slowly while the SH-Streptavidin case shows a sharper decay. This effect cannot be observed in the association phase because relatively high target concentration were used, there are always an exchange between bleached chromophores and fresh ones from solution.

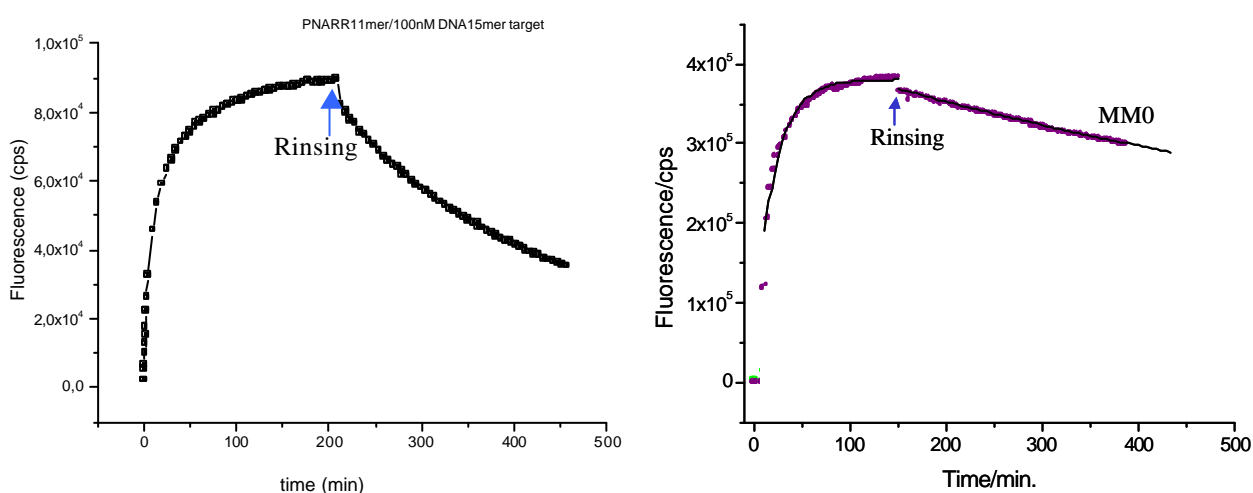


Figure 6: SPFS measurement of DNA RR15mer target hybridisation with PNA11mer probe immobilized onto A) SH-Streptavidin, B) biotinylated thiol/OH-thiol mixture/streptavidin matrixes

5.3 CCD Saturation Test:

To have a reliable measurement, it is important to check the performance of the camera in time. For that purposes, a serial of experiment was performed. The intensity read out of the CCD was recorded for different laser intensities. As it can be seen in Fig.1, the laser intensity was tuned from 200% to 75 % and an image was captured for each intensity level during 25sec. capturing time.

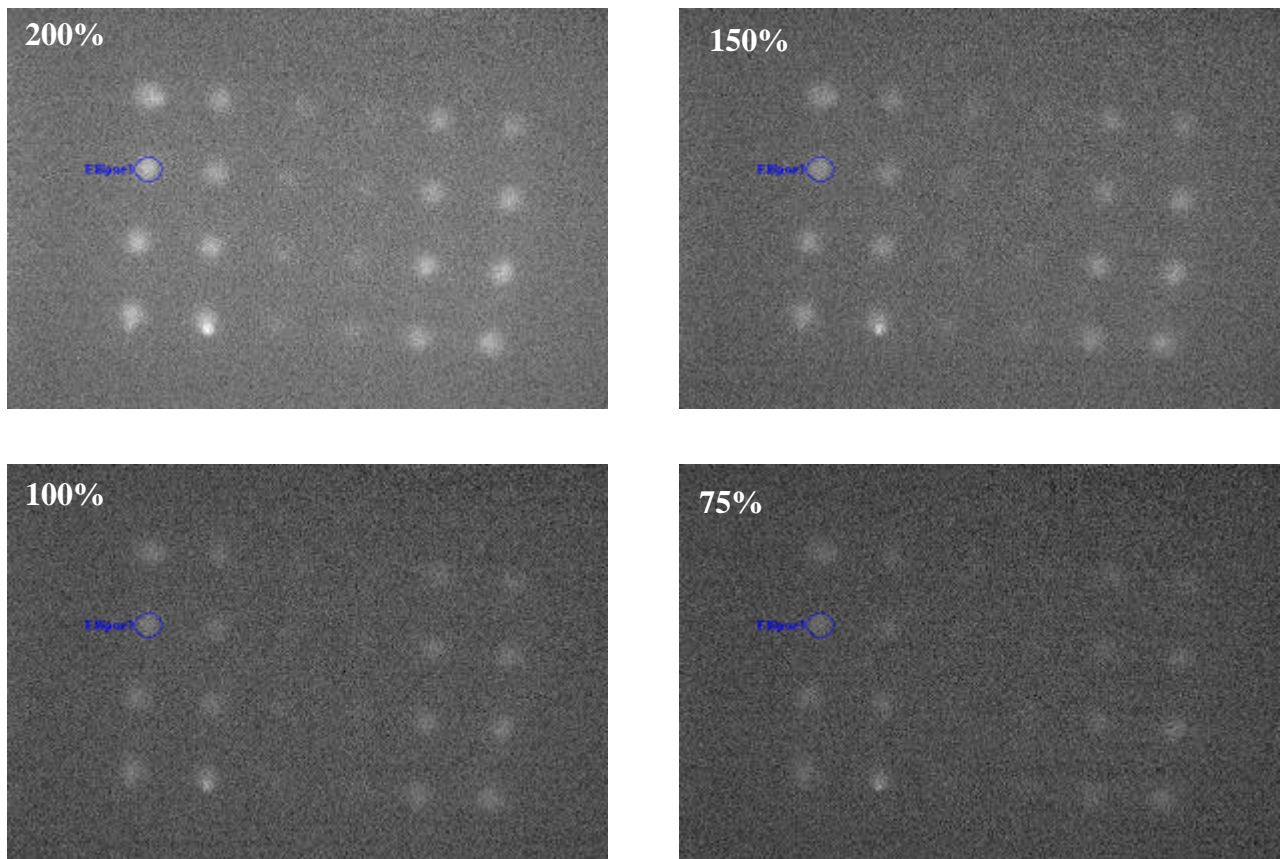


Figure 1: Laser intensity (200%, 150%, 100% and 75%) vs. Integrated intensity read-out.

Fig.2 shows a linear relation between the integrated intensities and the laser intensity. This indicates that the CCD is not in a saturation point and the read-out is reliable.

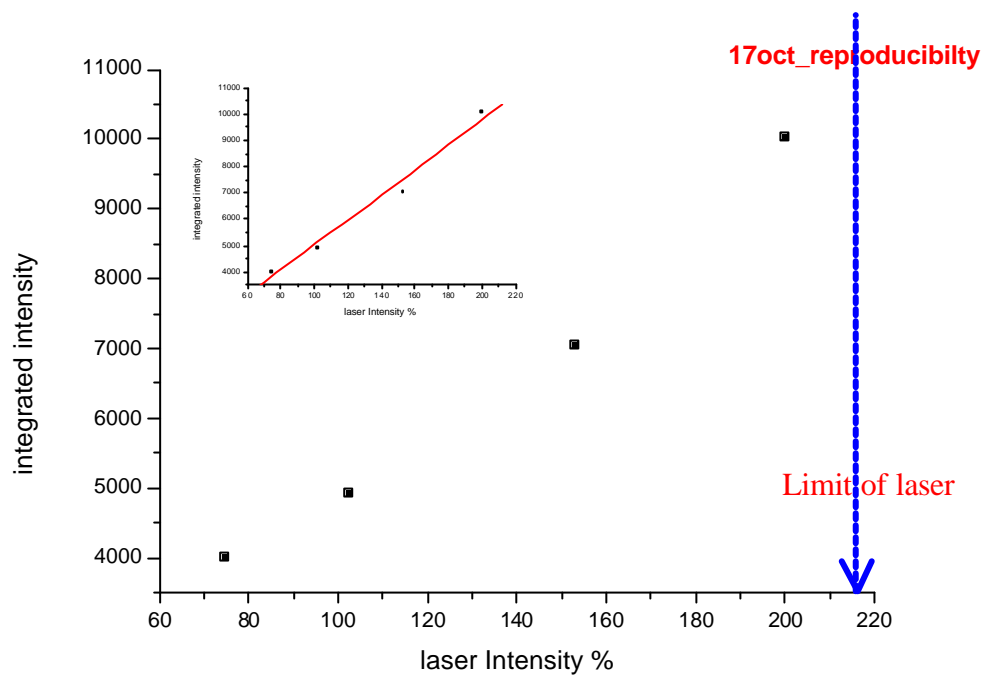


Figure 2: Integrated intensity vs. laser intensity

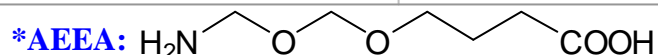
5.4 PNA-DNA Hybridization on a Biotin thiol / Streptavidin Matrix

5.4.1 Array A:

The following experiments were done as a model system for the combination of mismatches and specific binding on a same chip. For that purposes, 11 and 15mer PNA probes, that have mentioned in section 4.3.1 and the probes PNA P1, P2 and P3 (section 4.3.2), that have mismatches in their sequences to the same target have been used.

Table 1: PNA probes and the complementary targets

PNA for Roundup Ready (RR probes)	11mer: <i>Biotin</i> -AEEA-AEEA- AGAGTCAGCTT -NH ₂ 13mer: <i>Biotin</i> -AEEA-AEEA- CT AGAGTCAGCTT -NH ₂ 15mer: <i>Biotin</i> -AEEA-AEEA- TG CT AGAGTCAGCTT -NH ₂
DNAs (target)	11mer: Cy5-5'- AAGCTGACTCT -3' 13mer: Cy5-5'- AAGCTGACTCTAG -3' 15mer: Cy5-5'- AAGCTGACTCTAGCA -3'
<u>PNA</u>	P1 probe 30 5'- <i>Biotin</i> -T15 TGT AC G TCA CAA CTA -3' P2 probe 30 5'- <i>Biotin</i> -T15 TGT ACA TCA CAA CTA -3' P3 probe 30 5'- <i>Biotin</i> -T15 TGT AC G TGA CAA CTA -3'
<u>DNA targets</u>	T1 target 15 5'- Cy5 -TAG TTG TGA CGT ACA -3' T2 target 15 5'- Cy5 -TAG TTG TGA TGT ACA -3' T3 target 15 5'- Cy5 -TAG TTG TCA CGT ACA -3'



The spotting was done by using an ink-jet spotter thiol/biotin-streptavidin substrate. The humidity of the printing chamber was kept at 70% during the spotting process. After allowing the probe to react with the streptavidin coated surface for about 2 hrs, the sample was placed into a sample holder. Fig.1 shows the SPM image of the array in air.

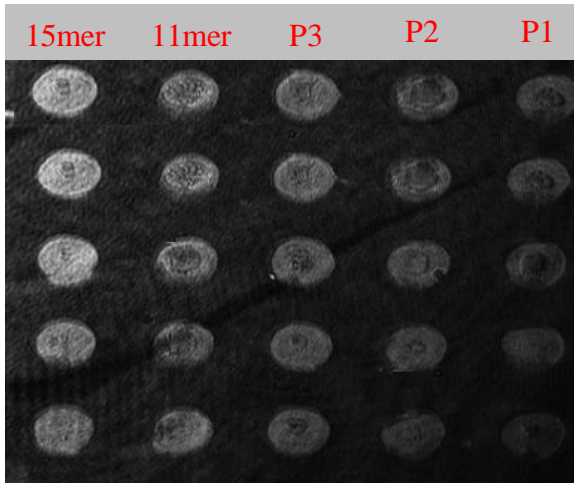


Figure 1: SPM image of Array A in air

SPFM images have been captured before (Fig.12A) and after (Fig.2B) injection of the fluorescence target. After a 500nM 11mer target solution was injected PNA-DNA hybridization was observed as a function of time and quantified with line scans (cf. Fig.3). Since the 15mer PNA probe has the same 11mer sequence in its structure, it has been observed that the 15mer probe has also bound to the 11mer target. As it can be seen in Fig.2, there is no non-specific binding to the P1, P2 and P3 probes.

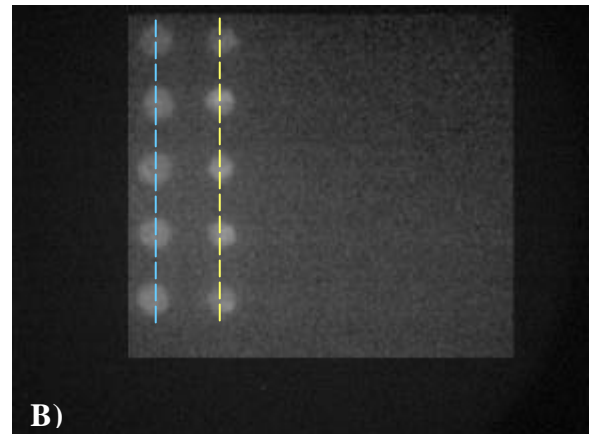
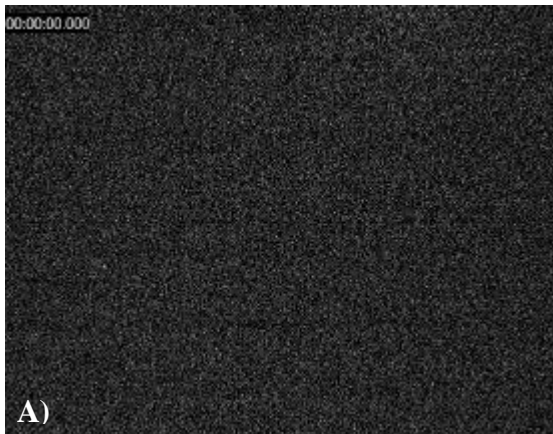


Figure 2: SPFM image of array A) before, B) after 15 min. hybridisation with 11mer 500nM target $t_{acq} = 25\text{sec}$.

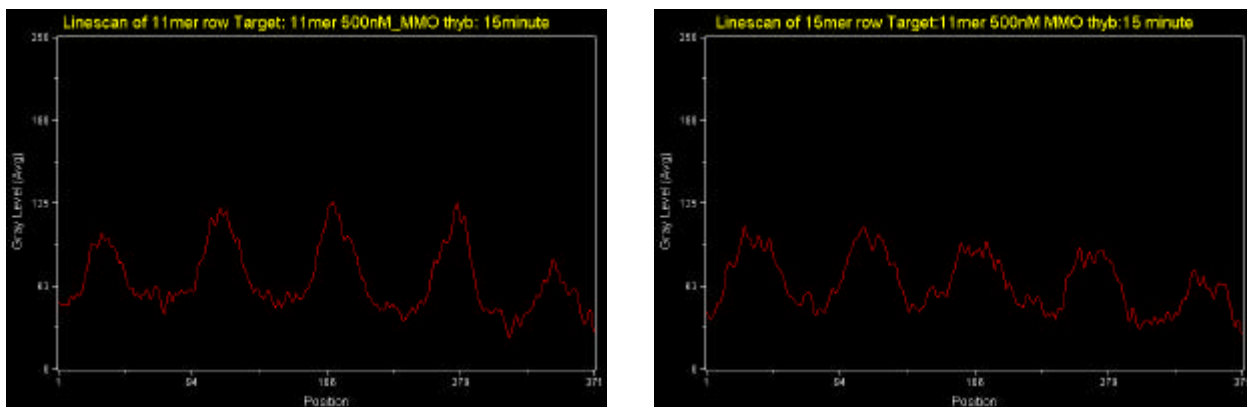


Figure 3: A) Line scan on 11mer column

B) Line scan on 15mer column

As it can be seen from Fig.3, the intensity level in the 11mer row is higher than that of 15mer which was the opposite in SH-Streptavidin matrix system in the previous chap. This clearly shows the importance of the SAM layer. Hence puts the chromophore molecule more further from metal surface and avoids the distance depending quenching.

The array surface was regenerated by using 10mM NaOH solution and rinsed with PBS buffer (cf. Figure 4).

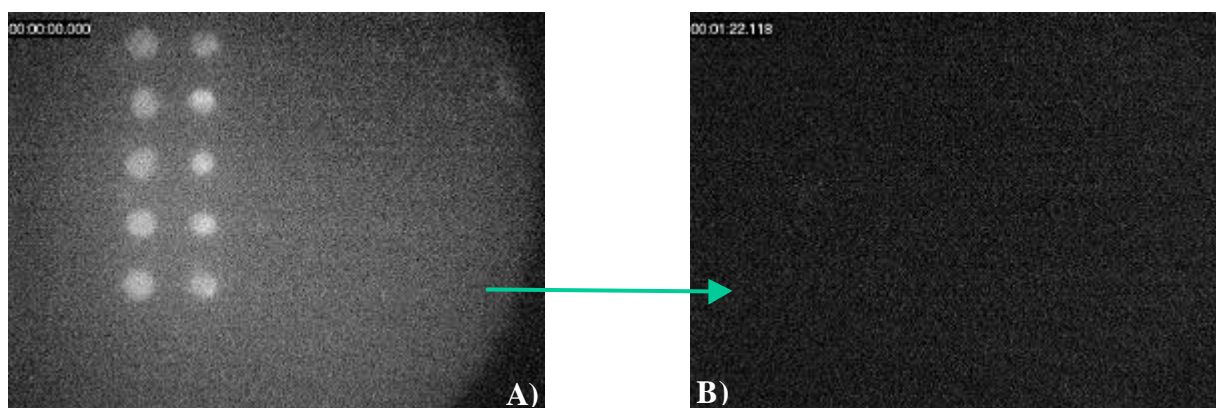


Figure 4: SPFM image of the array before A) and B) after regeneration

After the regeneration and a rinsing step, a 500nM T3 target solution which is MM0 to P3, MM1 to P1 and MM2 to P2 probes was injected into the flow cell and images were captured after 2hr. hybridisation (cf. Figure 5). After rinsing line scans were taken from each probe columns (Fig. 6-A, B and C).

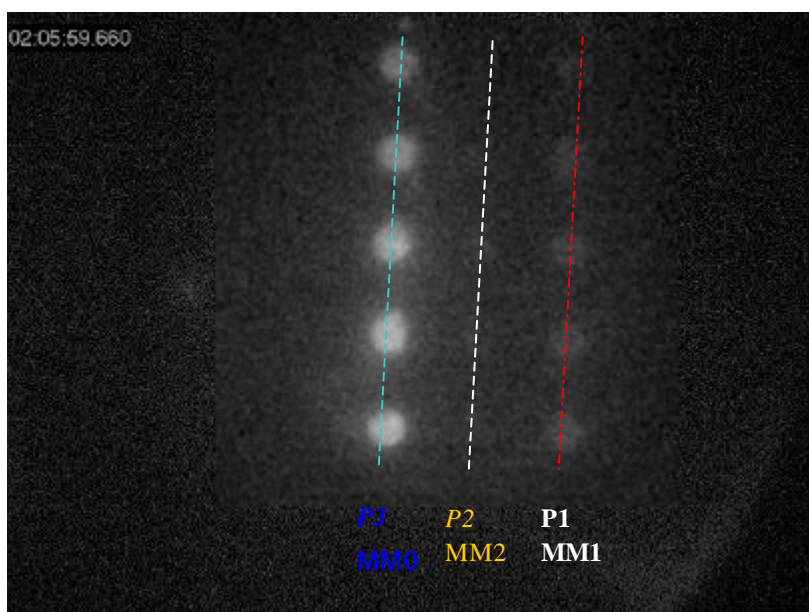


Figure 5: SPFM image of array after hybridisation with 500nM DNA T3 target

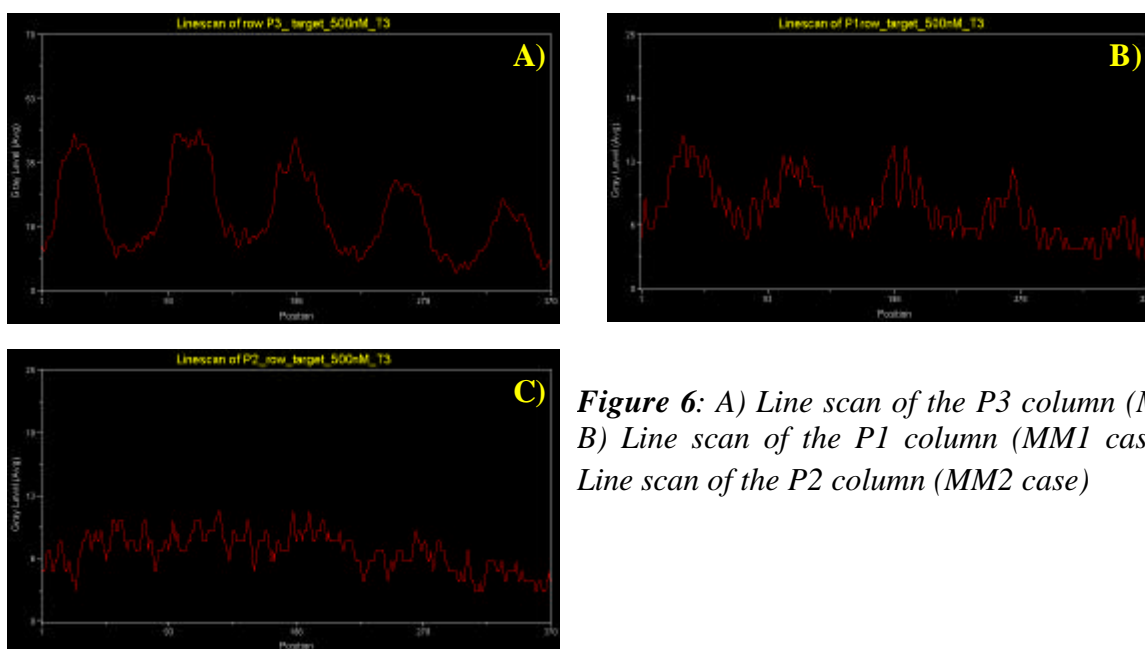


Figure 6: A) Line scan of the P3 column (MM0 case) B) Line scan of the P1 column (MM1 case) and C) Line scan of the P2 column (MM2 case)

Since the target has different affinities to the probes, the intensity levels of the MM0, MM1 and MM2 situations are different as seen also from Fig.7- A, B and C. The intensity level of MM2 case is almost in the background level.

After the 3rd regeneration of the surface, 50nM RR125 target solution was injected to the same chip after a melt&quenching process (for single strand fabrication). As seen in Fig.7, the target again specifically binds to the 11 and 15mer PNA probes. Here 15mer probe shows higher intensity than 11mer with PCR target because the PCR target has all the 15mer complementary bases that 15mer probe has.

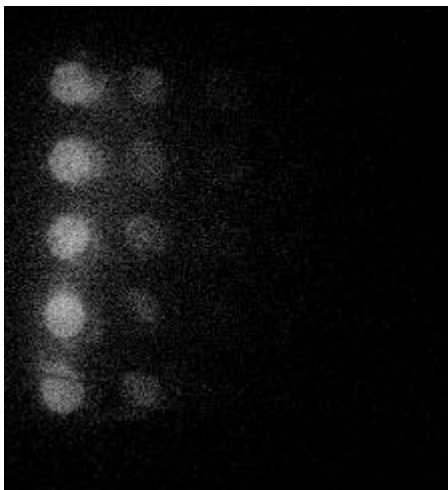


Figure 7: SPFM image of array after hybridization with 50nM GMO RR125 target.

After the 50nM RR125 target hybridization, these time a target solution with $C_0=1.6\text{nM}$, which corresponds to the K_d -value, has been tried after regeneration of the same surface for the 4th time. SPFM images have been captured (cf. Fig. 8) and line scans were applied (cf. Fig. 9).

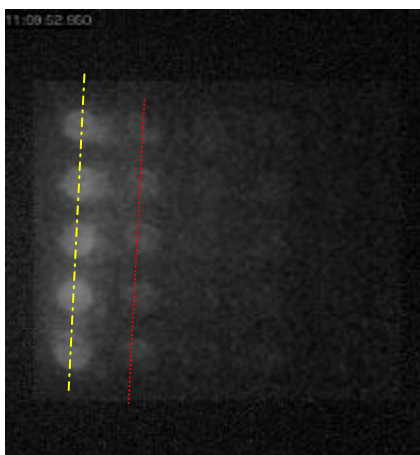


Figure 8: SPFM image of the array after hybridization with GMO RR125 target at $C_0=1.6\text{uM}$

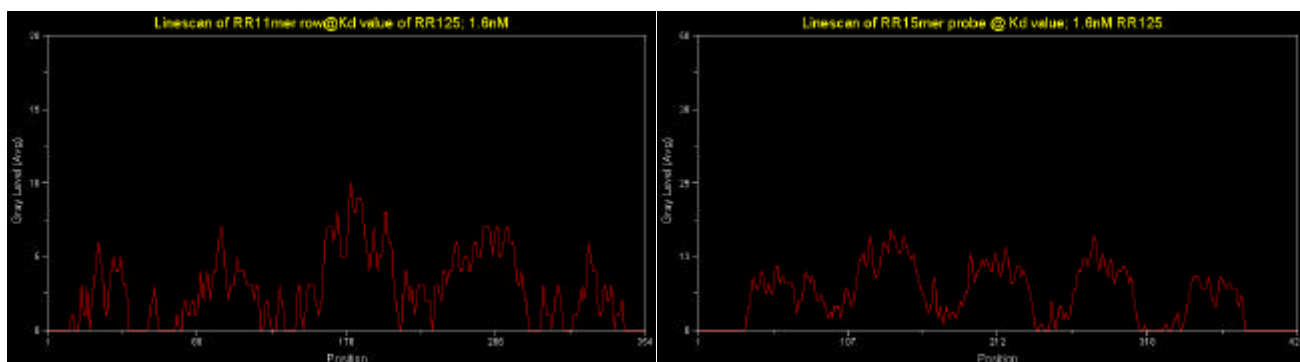


Figure 9: A) Line scan on 15mer Column

B) Line scan on 11mer column

After the 5th regeneration, the PCR target (Mü196) that has a complementary sequence to the P probes was injected to the system and as seen in Figure 10, it can still bind specifically to the P probes with different intensity corresponding to the different mismatch situations.

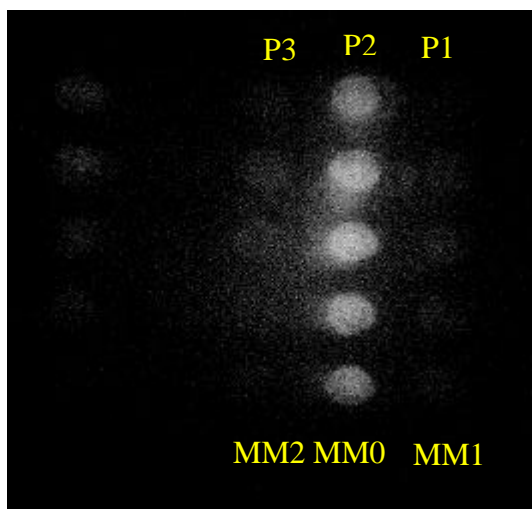


Figure 10: SPFM image of the array after hybridization with 50nM Mü 196 Target

After that all GMO detection, the surfaces has been regenerated several times. In the following experiment, the surface has been regenerated 8 times and, 50nM 11mer MM0 target has been injected to check the surface stability. The hybridization reaction takes place and after 8th regeneration, reproducible results can be obtained. In fact, Fig.11 and 12 correspond to a similar experiment as Fig.3 and shows similar result.

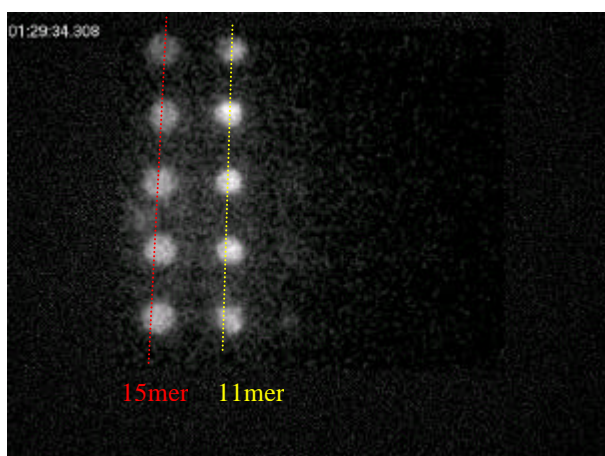


Figure 11: SPFM image of the array after hybridization with 50nM 11mer target

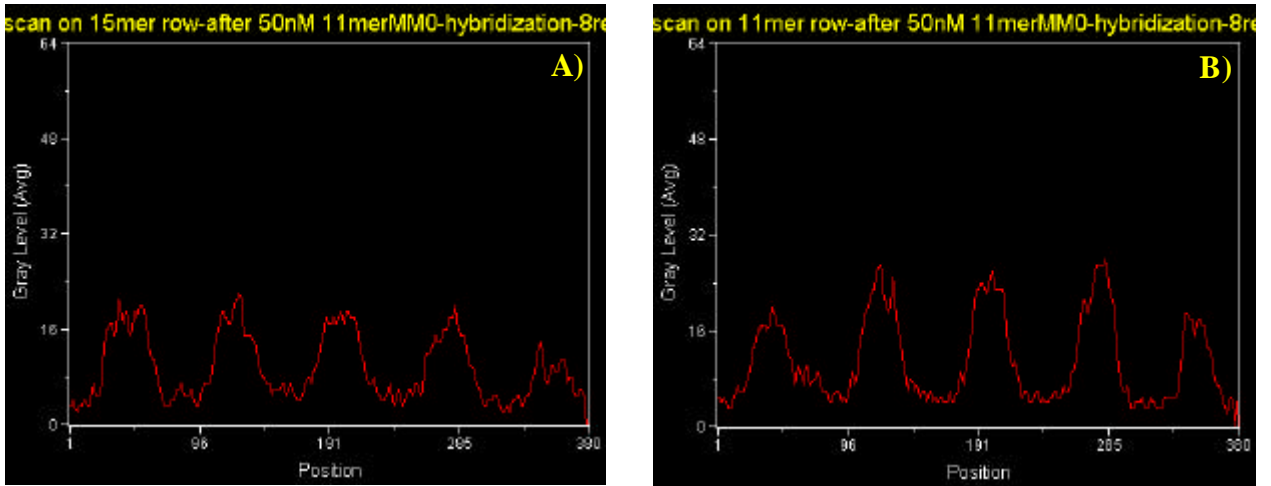


Figure 12: Line Scans after hybridization with 50nM 11mer MM0 target on A) 15mer row B) 11mer row.

5.4.2 Array B:

All Parma PNAs have been spotted using a Pin-tool spotter under the same conditions and having the same surface chemistry that has been described in the Array A. This array represents the final goal of the project, which is determination of GMO ingredient (RR target) from natural component (SL targets) in the food. The SPM image of the array is shown in Fig.1.

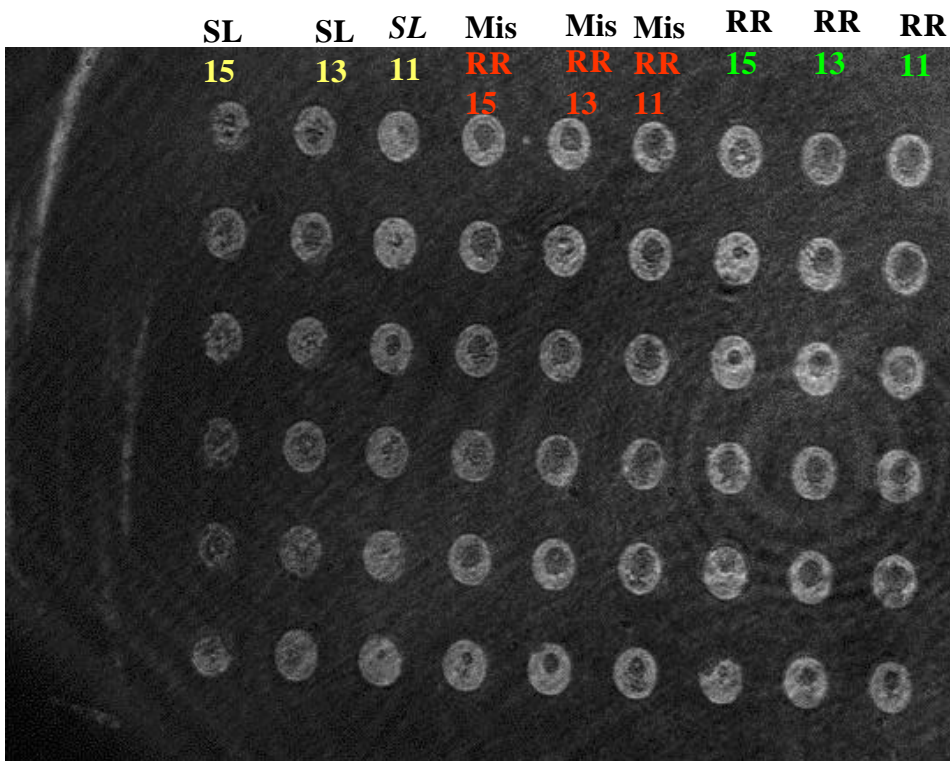


Figure 1: SPM image of Array B in air (All Parma PNAs at 1nM probe concentration)

In the Fig.2, the hybridization reaction with 500nM of a RR11mer target can be observed. As seen before, while the target hybridized with MM0 probes, the MM1 probes was stayed almost in the background level. However, another case that observed in the Fig.2 is that, SL probes have unspecific binding to RR11mer target. That means that the probe design needs to be improved for the future experiments by the Parma collaborator where the probes were received.

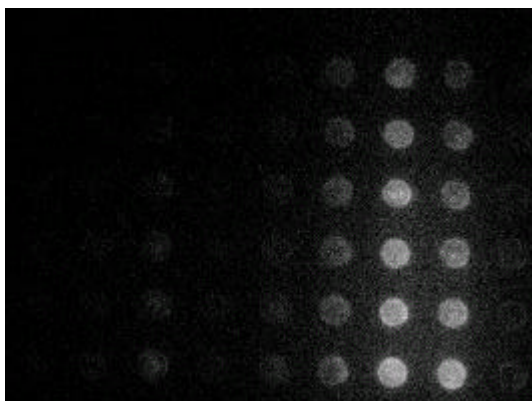


Figure 2: SPFM image of the array after injection of 500nM 11mer target

After regeneration of the surface and rinsing with the buffer afterwards, RR125 PCR target having 1% detection limit concentration was injected after melt & quench cycle and the hybridization reaction was observed by capturing SPFM images (Fig.3).

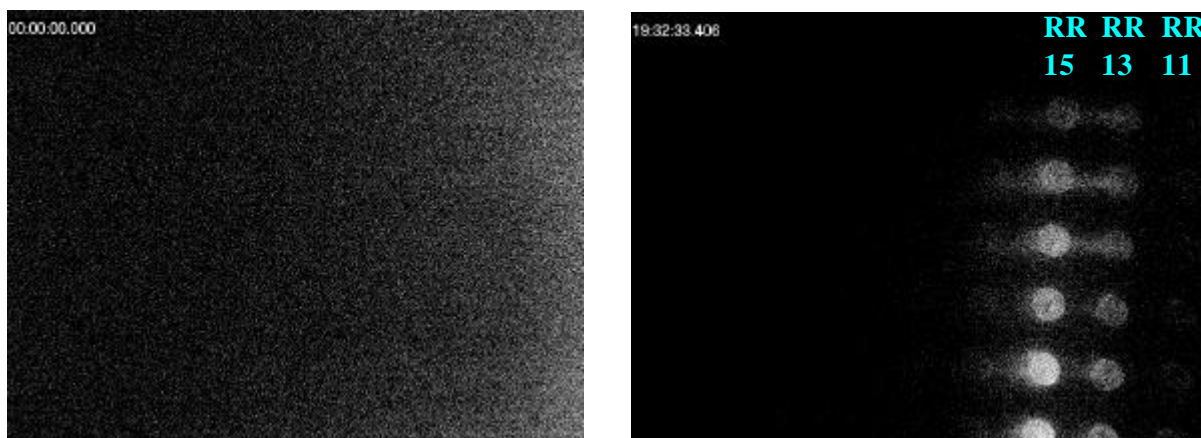


Figure 3: SPFM image of the array before A) and after B) hybridization with 1% RR125 GMO target solution

As can be seen, pure 1% GMO (which refers to the 1% detection limit concentration by dilution) can be detected. A critical test, however, is the detection

out of a cocktail solution. For that purpose, a solution containing 1% of labeled RR125 PCR amplicons in 99% unlabelled 75mer PCR "impurities" was injected and the hybridization was observed. After rinsing, SPFM images have been captured (Figure 4) and the intensities were quantified with line scans on probes and the background (Figure 5- A, B and C, respectively)

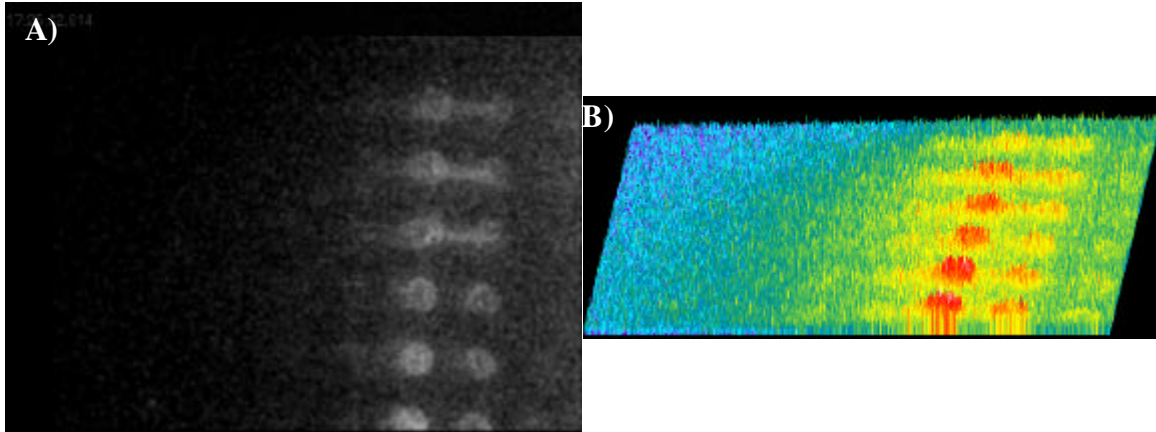


Figure 4: A) SPFM image of the array after hybridization with a PCR mixture 1%RR125 + 99% impurity and B) its intensity profile

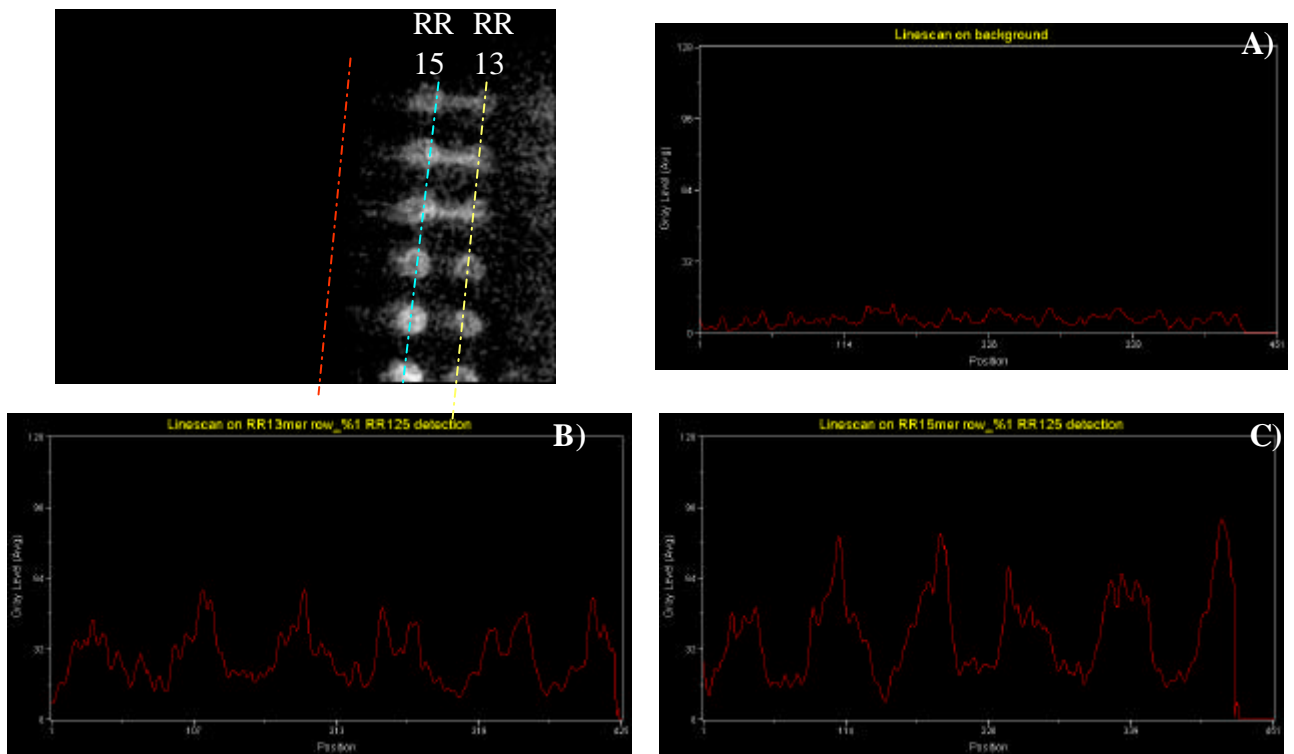


Figure 5: Line scan on A) background, B) on RR13mer and C) on RR 15mer

As it can be seen from the SPFM images and the line scans, 1% GMO from the cocktail solution was detected significantly out of natural components.

5.5 Conclusions

In this chapter, we describe how Surface Plasmon Fluorescence Microscopy (SPFM) can be used to determine the GMO content in food samples. For that purpose, DNA and PNA microarrays have been prepared on biotinylated thiol-OH thiol mixture/Streptavidin and SH-streptavidin matrices using Ink-Jet and Pin-Tool spotters. Arrays with mismatch carrying (MM) oligonucleotide probes of different lengths have been prepared. DNA and PCR target were injected into the system and hybridisation has been observed by capturing images by a cooled CCD camera during the hybridisation process.

SPFS experiments were performed in order to define the best surface chemistry for further experiments. It was observed that the fluorescence intensity decreases artificially in SH-Streptavidin matrices where SAM is not used for building the catcher probe layer. Here, the chromophores get quenched due to reduced distance to the metal surface. Therefore, it was decided to prepare the arrays onto biotinylated thiol/OH-thiol mixture/Streptavidin matrix.

Before performing the GMO detection on a single array where all natural (SL) and genetically modified probes (RR) are involved, some model experiments were performed. Arrays from DNA and PNA probes carrying MM sequences and different strand length on the same chip were prepared. As a summary of the measurements mentioned above in section 5.4, we saw that we can differentiate the target easily if it carries single or two mismatches from its fully complementary strand even though they are on the same array with the other probes which are specifically designed for GMO detection. However due to some intrinsic limitation of the SPFM technique, it is hard to make a comparison between the DNA and PNA probes for the GMO detection.

Finally, all the probes designed for GMO detection (RR probes) and extracted from natural food component (SL probes) were immobilized on one chip. 1% GMO in the mixture, which is the amount for labelling requirement in EU, was able to detect

specifically from the natural food component (SL) by using SPFM technique on an array platform.

Using SPFM, we could easily detect 1% GMO out of a mixture. This value corresponds to the amount, which requires labelling according to the EU laws. Therefore we could show that the SPFM technique, presented in this work, is well suitable for the detection of genetically modified genes in food chain. However, for future SPFM experiments, it is important to consider the probe design.

List of Figures

Chpt1-2

- Figure 1:** Schematic representation of the double helix (left) showing the minor and the major groove, a DNA single-strand illustrating the way the sugar units are linked via the H-bonding between specific Watson-Crick base pairs (right) and phosphodiester bridges (middle).....8
- Figure 2:** The structure of PNA and hybridization scheme with DNA strand.....10
- Figure3:** Target strand amplification by PCR
(<http://allserv.rug.ac.be/~avierstr/pdf/PCR.pdf>)..... 14
- Figure 4:** Ink-jet spotter.....19
- Figure 5:** a) Pin Tool spotter and b)Tip position from surface).....20
- Figure 6:** a) Solid pin, b) Split pin (www.pointech.com).....20
- Figure 7:** Effect of spotting solution on spot quality, right image is without spotting solution and the left one is with spotting solution (www.telechem.com).....21
- Figure 8:** Jablonski energy level diagram.....22
- Figure 9:** Schematic description of Langmuir adsorption. As it can be seen from the graph, the surface coverage is dependent on adsorption and desorption rate constants, k_{on} and k_{off} respectively.....26
- Figure 10:** The basic configuration for evanescent optics.....29
- Figure 11:** Schematic representation of reflected and transmitted P-polarized light at the interface between two optically different media30
- Figure 12:** Dispersion relation for A) free photons in a dielectric, B) free photons propagating in a coupling prism, SP1) surface plasmons at a metal/dielectric interface and SP2) surface plasmons after adsorption of an additional dielectric layer [Liebermann, 1999]. 33
- Figure 13 a)** Reflection geometry for photons with a momentum k_{ph} at a metal/dielectric interface. The angle of incidence \mathbf{q} determines the absolute value of the momentum in z-direction, $k_{ph, z}$, that is relevant for surface plasmon excitation. b) Kretschmann configuration for momentum matching..... 34
- Figure 14:** As it was described in the text above, resonant coupling is observed as a very pronounced drop in angular scan of the reflected light intensity at \mathbf{q}_R . \mathbf{q}_c is the critical angle for Total Internal Reflection (TIR).....35

Figure 15: a) Scan curves of Biotin-Streptavidin binding onto biotinylated/OH-terminated thiol modified Au surface. The resonance angle shift is around 0.5 degree since streptavidin is a big bulk molecule which has molecular weight around 60K. b) kinetic curve of streptavidin binding onto same surface. The binding was observed at fixed resonance angle by following the reflective index change in time.36

Figure 16: Schematic drawing of a fluorophore positioned close to a metal/dielectric interface. Different fluorescence decay channels take place at different fluorophore/metal separation distances.....38

Figure 17: Schematic representation of SPM & SPFM set-up (from Rothenhäusler et al., 488, 1988, Nature).....40

Figure 18: Schematic representation of SPM and SPFM techniques with a 3D spatial filter configuration.....41

Chpt.3

Figure 1: Schematic sketch of a surface plasmon spectrometer (SPR) set-up including various extensions. The whole set-up including the motors of the goniometer is remote controlled by a personal computer using the software WASPLAS.....45

Figure 2: Actual picture of the SPR set-up with different modifications: A) CCD Camera, B) 3D beam expander.....46

Figure 3: experimental set-up of SPM (taken from dissertation of Thomas Neumann).....47

Figure 4: Chemical structure of a) 1-mercapto-undecanole and b) 11-mercapto-(8-biotinamido-4, 7, dioxaoctyl)-undecanoylamide, (c) Schematic of the self-assembly process. The anchor group, in this case S-H, has a strong chemical affinity to the gold surface. A covalent Au-S-bond is spontaneously formed by the mere exposure of the thiol solution to the gold surface. In the course of the reaction, all available binding sites on the gold surface are occupied by thiol molecules. The alkyl-chains adopt a parallel orientation with a uniform tilt angle of 30° relative to the surface normal. Such a highly ordered surface architecture meets perfectly the steric requirements for streptavidin binding (right cartoon).....49

Figure 5: Schematic representation of a mixed monolayer of biotin- and EG (spacer)-thiol (with a molar ratio of 1:9 in the preparation solution) covered with streptavidin, probe and target.....50

Figure 6: Molecular structure of a single streptavidin tetramer. Four biotin molecules (chemical structure on the right side) are depicted using a ball and stick model.....51

Figure 7: SPR detection of streptavidin binding. a) resonance angle shift after binding and b) kinetic observation of binding reaction in time.....52

Figure 8: Construction of the measurement chamber (left) and top view of the flow cell including a schematic of the circulation loop (right).....53

Figure 9: Angular Scan measurement after probe immobilization.....55

Figure 10: A typical SPR scan curve with the fluorescence (SPFS).....56

Figure 11: Single kinetic measurement with fluorescence. 1) Injection of target solution; 2) hybridisation, association phase; 3) saturation of fluorescence signal; 4) start of rinsing; 5) disassociation phase with continued rinsing.....57

Figure 12: Chemical structure of Cy5 chromophore, which has its maximum absorbance at $\lambda=649\text{nm}$ and emission at $\lambda=670\text{nm}$58

Figure 13: a) A typical titration experiment with a concentration range from pM to nM and b) obtaining the binding constant from Langmuir Isotherm fitting.....60

Figure 14: Monitoring of the fluorescence vs. time during the regeneration process with 10mM NaOH.....61

Chpt4

Figure 1: Decay channels for fluorescence emitted near a metallic surface A) non-radiative energy transfer, B) coupling of irradiated fluorescence light to SP modes, C) free emission of fluorescence.....65

Figure 2: Structural formula of 2,6-diaminopurine represented as “D” ($\text{C}_{11}\text{H}_{14}\text{N}_8\text{O}_2$).66

Figure 3: A) Mimic of the neutral thymine nucleobase, 7-chloro-1,8-naphthyridine-2(1H)-one; The Watson-Crick base pair interaction B) between natural Adenine-Thymine, C) Adenine-Modified Thymine bases67

Figure 4: Unspecific binding measurement between Lysine and dye.....69

Figure 5: Single kinetic measurement of PNA2361 with 100nM target concentration in 10 mM70

Figure 6: A) Single kinetic measurement of PNA2364 and B) its Langmuir fit with the flow rate 2.5ml/min. C) same kinetic measurement with a faster flow rate, 3.6ml/min and using 10nM target concentration and zoomed-in plot of association (small graph).....71

Figure 7: A) Single kinetic measurement of PNA2367 after twice regeneration of the surface and B) Langmuir fitting of kinetic curve.....72

Figure 8: A) Single kinetic measurement of PNA2370 and B) MM1 case with 100nM target.....73

Figure 9: Single kinetic measurement of PNA2370 with 500pM target concentration in PBS	74
Figure 10: Single kinetic measurement of A) PNA2376 and B)PNA2379 with 100nM target	74
Figure 11: Plot of K_a from single kinetic measurement vs. DT_m	76
Figure 12: Titration curve of PNA2361 A) MMO titration experiment B) conventional representation and C) linearized isotherm plots relating target concentrations with respective saturation intensity and b) and c) focused plots of B) and C) respectively.....	78-79
Figure 13: Angular scan with fluorescence after saturation of each target concentration in the titration measurement	79
Figure 14: Langmuir isotherm (A) and linerized plot (B) of PNA2361 derived from angular scan with fluorescence.....	80
Figure 15: A) Angular Scan with the fluorescence after each concentration saturation in titration measurement B) Langmuir isotherm C) Linearized curve of PNA2379 derived from angular scan with fluorescence.....	81
Figure 16: A) titration measurement of PNA2373 and B) Lanmuir fitting for association phase (k_{on}) of plot A.....	83
Figure 17 : Titration measurement of PNA2370 and summary of the k_{on} , k_{off} values from the fitting of plot A and calculated affinity constant from k_{on}/k_{off}	84
Figure 18: Comparison of K_a values obtained from single kinetic, saturation and angular scan measurements for the all PNAs.....	85
Figure 19: Single kinetic measurement with 5 different concentration.....	87
Figure 20. Langmuir fitting for dissociation phase of each concentration	87
Figure 21. Langmuir fitting for the association phase of A)1nM, B)10nM, C)50, and D)100nM target concentration.....	88
Figure 22. Linear fit of k_a vs. concentration plot.....	89
Figure 23: Comparison of association constant, k_{on} , obtained from Single Kinetic measurement and Global Analysis.....	90
Figure 24: Comparison of the affinity constants, K_a , obtained from Single Kinetic measurement and from Global Analysis.....	91
Figure 25: K_a from Global Analysis vs. DT_m	92

Figure 26: Plotting of K_a values obtained from Single kinetic, both Saturation and angular scan from titration measurements and Global Analysis measurement vs. DT_m 92

Chp4.2

Figure 1: SPM image of Array 2A. CC refers coupling control @ different resonance angle.....96

Figure 2: A) Background image, B) SPFM image before any target injected..... 96

Figure 3: SPFM image of the array after hybridizing with 50nM target(A), false color representation(B) and intensity profile(C) of the same image.....97

Figure 4: Line scan on A) C5, B) B5 and C) A5 row.....97

Figure 5: Region measurement of the spots on array after rinsing.....98

Figure 6: A) SPM image of array, A) in air and B) cartoon drawing of the array98

Figure 7: A) Line scan image and B) lines scan plot of array after hybridized with 50nM target and rinsed with buffer C) image and region measurement values after overnight rinsing.....98-99

Figure 8: Integrated intensity vs. time plotted for each PNA.....99

Figure 9: Zoomed-in plot of Fig.8, Integrated intensity vs. time plotted for each PNA.....100

Figure 10: Langmuir Fit for C3 column.....101

Figure 11: SPM image of array 1A, A) against air and B) cartoon drawing of the array.....101

Figure 12: SPFM image of array 1 A) after appr.2 hrs rinsing and B) its line scan, C) after overnight rinsing and D) its linescan.....102

Figure 13: The averaged region measurements of the spots in each row and values summarized in the table.....102

Figure 14: Regeneration of array A)before rinsing, B) 7min after C)23min and D) after 40min. rinsing with $\text{NaOH}_{(aq)}$ and later with buffer.....103

Figure 15: region measurements and SPFM image of the array1A after hybridization with 50pM target.....103

Figure 16: A) SPM image B) SPFM image of the array before hybridization.....104

Figure 17: A) SPFM image of array B) line scan on the PNAs and C) graph of line scan after hybridization with 50nM target and rinsing with PB buffer overnight....104

Figure 18: Graph of integrated intensity vs. time for all PNAs (Including PNA2523)105

Figure 19: Plot of K_a values obtained from single kinetic measurement with SPFM technique vs. DT_m values each PNA (PNA2523 excluded).....106

Figure 20: Cartoon representation of the array and SPFM images of the titration starting from 200pM to 100nM SPFM.....107

Figure 21: A) Langmuir Isotherm and B) linearized Langmuir isotherm of PNA2361 from titration measurement with SPFM.....107-108

Figure 22: K_a values obtained from titration measurement and single kinetic measurements with SPFM for each PNA.....109

Figure 23: K_a values obtained from titration measurement with SPFM technique vs. DT_m values for each PNA.....110

Figure 24: Comparison of the K_a values obtained from SPFM and SPFS techniques for each PNA.110

Chp5

Figure 1: SPM image of DNA P1, P2,P3 probes in air- (no target injected).....114

Figure 2: Calibrated spot size in the based of pitch length115

Figure 3: SPFM image of the array after hybridization, just started to rinse.....115

Figure 4: SPFM picture of the array hybridized with 1 μ M T2 target and 13min. after rinsing with PBS.....116

Figure 5: Line scan of P2 row, which is MM0 for T2 target.....116

Figure 6: Line scan of P1 row, which is MM1 for T2 target.....116

Figure 7: Line scan of P1 row, which is MM1 for T2 target.....117

Figure 8: Integrated intensity measurement for selected region for P1, P2 and P3.117

Figure 9: Regeneration of P1,P2,P3 array after hybridization with T2 target.....118

Figure 10: SPFM picture of the array after hybridized with 1 μ M T3.....118

Figure 11: Line scan of P1 row, which is MM2 for T3 target.....118

Figure 12: Line scan of P2 row, which is MM1 for T3 target.....119

Figure 13: Line scan of P3 row, which is MM0 for T3 target.....119

Figure 14: series of images captured during rinsing after hybridisation with T3 target.....120

Figure 15: Avarage integrated intensity values of each PNA probe.....120

Figure 16: Langmuir isotherm of P1(MM0),P2(MM1) and P3(MM2) probes after hybridisation with 100nM T1 target.....121

Figure 17: Hybridization with 100nM PCR target Mü196122

Figure 18: SPM image of 4*4 DNA array124

Figure 19: SPFM image of array after hybridisation with RR125 GMO target..... 124

Chpt5.2

Figure 1: A) SPFM image of the sample before injecting fluorescence labeled target and B) carton representation of the array.....127

Figure 2: Array of 11 and 15mer PNA after hybridization with 100nM 11merMM0 target; first and the last two columns are PNA15mer and two columns in the middle are 11mer PNA. Image(A) is intensity profile and (B) is the SPFM image after hybridization and C) after overnight rinsing.....127

Figure 3: Line scan graph (A) and image (B) on the row of 15mer-11mer-15mer PNA probes after hybridization with 100nM 11mer DNA target.....128

Figure 4: A) The SPFM image and B) intensity profile and C) Line Scan of array after injecting 100nM of 11mer MM1 target onto 5xregenerated surface.....129

Figure 5: SPFM image of array A) before B) after regeneration129

Figure 6: SPFS measurement of DNA RR15mer target hybridisation with PNA11mer probe immobilized onto A) SH-Streptavidin, B)biotinylated thiol/OH-thiol mixture/streptavidin matrixes.....130

Chpt5.3

Figure 1: Laser intensity (200%, 150%, 100% and 75%) vs. Integrated intensity read-out.....131

Figure 2: Integrated intensity vs. laser intensity.....132

Chpt5.4.1

Figure 1: SPM image of Array A in air.....134

Figure 2: SPFM image of array A) before, B) after 15 min. hybridisation with 11mer 500nM target tacq= 25sec.....134

Figure 3: A) Line scan on 11mer column ,B) Line scan on 15 mer column.....135

Figure 4: SPFM image of the array before A) and B) after regeneration135

Figure 5: SPFM image of array after hybridisation with 500nM DNA T3 target....136

Figure 6: A) Line scan of the P3 column (MM0 case) B) Line scan of the P1 column and (MM1 case) C) Line scan of the P2 column (MM2 case)136

Figure 7: SPFM image of array after hybridization with 50nM GMO RR125 target.....137

Figure 8: SPFM image of the array after hybridization with GMO RR125 target at $C_o=1.6\mu M$137

Figure 9: A) Line scan on 15mer Column ,B) Line scan on 11mer column..... 137

Figure 10: SPFM image of the array after hybridization with 50nM Mü 196 Target.....1389

Figure 11: SPFM image of the array after hybridization with 50nM 11merTarget..... 138

Figure 12: Line Scans after hybridization with 50nM 11mer MM0 target on A) 15mer row B) 11mer row.....139

Chpt5.4.2

Figure 1: SPM image of Array B against air (All Parma PNAs @ 1mM probe concentration).....139

Figure 2: SPFM image of the array after injection of 500nM 11mer target.....140

Figure 3: SPFM image of the array before A) and after B) hybridization with 1% RR125 GMO target solution.....140

Figure 4: A) SPFM image of the array after hybridization with a PCR mixture 1%RR125 + 99% impurity and B) its intensity profile.....141

Figure 5: Line scan on A) background, B) on RR13mer and C) on RR 15mer ..,141

List of Tables

Table 1: PNAs that were obtained from the Copenhagen group and the targets which were commercially supplied from MWG, Germany.....68

Table2: Kinetic constants of the PNAs with 100nM Target concentration in PB buffer that was obtained after Langmuir fitting,.....75

Table 3: Affinity constant and half saturation value obtained from titration measurement for all PNAs84

Table 4: Summary of the values that were obtained from Global Analysis for each PNA..... 90

Chpt4.2

Table 1: Structures of PNAs and their array codes in the experiment.....95

Table 2: k_{on} , k_{off} , K_a and K_d results from SPFM and SPFS by Langmuir fitting.....101

Table 3: Intensity values of selected region in Fig.13.....102

Table 4: Affinity constant and half saturation value obtained from single kinetic and titration measurement by SPFM for all PNAs.....109

Chpt 5

Table 1: DNA probes and targets sequences.....114

Table2: Region measurement of each PNAs.....120

Table 3: Spot-to-spot variation.....121

Table 4: DNA probes and target sequences123

Chpt.5.2

Table 1: Sequences of probe PNAs..... 125

Table 2: Sequences of target DNAs..... 126

Chpt5.4

Table 1: PNA probes and the complementary targets.....133

